INFORMATION TO USERS

This manuscript has been reproduced from the microfilm master. UMI films the text directly from the original or copy submitted. Thus, some thesis and dissertation copies are in typewriter face, while others may be from any type of computer printer.

The quality of this reproduction is dependent upon the quality of the copy submitted. Broken or indistinct print, colored or poor quality illustrations and photographs, print bleedthrough, substandard margins, and improper alignment can adversely affect reproduction.

In the unlikely event that the author did not send UMI a complete manuscript and there are missing pages, these will be noted. Also, if unauthorized copyright material had to be removed, a note will indicate the deletion.

Oversize materials (e.g., maps, drawings, charts) are reproduced by sectioning the original, beginning at the upper left-hand corner and continuing from left to right in equal sections with small overlaps. Each original is also photographed in one exposure and is included in reduced form at the back of the book.

Photographs included in the original manuscript have been reproduced xerographically in this copy. Higher quality 6" x 9" black and white photographic prints are available for any photographs or illustrations appearing in this copy for an additional charge. Contact UMI directly to order.

UMI®

Bell & Howell Information and Learning
300 North Zeeb Road, Ann Arbor, MI 48106-1346 USA
800-521-0600

Development of a New Water–Water Interaction Potential and Application to Molecular Processes in Ice

Enrique R. Batista

A dissertation submitted in partial fulfillment
of the requirements for the degree of

Doctor of Philosophy

University of Washington

1999

Program Authorized to Offer Degree: Department of Physics

In presenting this dissertation in partial fulfillment of the requirements for the Doctorial degree at the University of Washington, I agree that the Library shall make its copies freely available for inspection. I further agree that extensive copying of this thesis is allowable only for scholary purposes, consistant with "fair use" as prescribed in the U.S. Copyright Law. Requests for copying or reproduction of this dissertation may be referred to University Microfilms, 1490 Eisenhower Place, P.O. Box 975, Ann Arbor, MI 48106, or to the author.

Signature Enrique Soltero

Date 21 April, 1999

University of Washington

Graduate School

This is to certify that I have examined this copy of a doctoral dissertation by

Enrique R. Batista

and have found that it is complete and satisfactory in all respects,
and that any and all revisions required by the final
examining committee have been made.

Chair of Supervisory Committee:

Hannes Jónsson

Reading Committee:

Samuel Fain

Samuel Fain

Marshall Baker

Marshall Baker

Date: 21 April, 1999

University of Washington

Abstract

Development of a New Water–Water Interaction Potential and Application to Molecular Processes in Ice

by Enrique R. Batista

Chair of Supervisory Committee

Hannes Jónsson
Dep. of Chemistry

A new potential energy function modeling the interaction among water molecules is presented. The dominant attractive interaction among the molecules, the electrostatic interaction, is represented with a multipolar expansion around the center of mass. The dipoles and quadrupoles are polarizable while the octopoles and hexadecapoles are fixed. The parameters in the multipole expansion are taken from experimental measurements on isolated water molecules or *ab initio* calculations. The molecules are treated as rigid objects. In addition to the electrostatics, the potential energy function includes dispersion energy and repulsive interaction at short range. The repulsive interaction includes many-body effects through density dependent parameters.

To test the multipolar representation of the electric field, a comparison was made with *ab initio* calculations of the field near water clusters (Moller-Plesset MP2 calculations) and in the interior of an ice crystal (gradient corrected Density Functional Theory calculations). Very good agreement was found even for distances that are significantly shorter than typical intermolecular distances.

Free parameters in the repulsive energy term were fitted to reproduce *ab initio* calculations of the energy of the water dimer as a function of distance, and the energy of ice I_h as a function of lattice constant.

This new water potential energy function is, therefore, transferable to different types of environments. We have interpolated the potential energy surface from the gas phase (clusters) to the condensed phase (ice).

We have applied the new potential function in a study of molecular processes on the surface of ice I_h, an environment which is in between gas phase and solid phase. The proton disorder in ice I_h leads to interesting and complex phenomena at the ice surface. The diffusion mechanism and the activation barriers for diffusion of water molecules in ice were evaluated by finding minimum energy paths for various diffusion hops. The results were used in a kinetic Monte Carlo simulation of surface diffusion in order to determine the overall diffusivity and an effective activation energy barrier. Satisfactory agreement with experimental measurements is found, but the experimental data is quite limited.

TABLE OF CONTENTS

LIST OF FIGURES

LIST OF TABLES

ACKNOWLEDGMENTS

I would like to thank my advisor Prof. Hannes Jónsson for his guidance and support. His excitement and encouragement were also determinants in the success of this project.

I would also like to thank the people at the Physics and Chemistry Departments of the University of Washington for having allowed me to work in this academic environment. Particularly Professors Marcia and Marshall Baker for their contagious enthusiasm and interest in the physics of ice and for our interesting discussion.

Financial support and scientific collaboration with researchers from Pacific Northwest National Laboratory (PNNL) is acknowledged. Specially I would like to mention the year-long collaboration with Dr. Sotiris Xantheas and Dr. Bruce Kay, both of whom it was a pleasure to work with.

It was pleasure to work in collaboration with Blas Uberuaga during part of this project.

This work benefitted very much from stimulating discussions with the members of the Jónsson Research Group though all these years, to whom I thank very much.

I would like to finish by thanking Dr. Sam Fain and Marilyn Carlson for their careful reading and correction of this document.

To Horacio and Dorotea Batista,

my parents.

Chapter 1

INTRODUCTION

Many environmentally important processes involve ice surfaces in one way or another. One interesting question is what controls the habits of ice crystal growth. This, for example, relates to the richness and complexity of snowflakes. Another issue is the mechanisms of chemical reactions occuring on the surface of ice crystals in the upper atmosphere, resulting, for example, in ozone depletion. In the last few decades, the stratospheric ozone layer has received increasing attention. The reaction thought to be responsible for ozone depletion involves the formation of Cl_2 on polar stratospheric clouds (PSC). Chlorine species such as Cl_2 can be extracted from the abundant HCl through reactions of the type $HCl + H_2O \rightarrow Cl^- + HOH_2^+$. Many different molecular processes, such as desorption, adsorption, surface and bulk diffusion, etc., will affect the morphology of the surface and kinetics of the reactions. At the temperature characteristic of PSCs, 180 to 210K, the surface of ice crystals is very dynamic, evaporating and condensing at the rate of 10–1000ML/sec [5].

Another important incentive for studying self-diffusion in ice is to help gain information from deep ice cores. The ice glaciers in Antartica and Greenland that have been accumulating ice for 150 thousand years provide records of past climatic changes and some other atmospheric phenomena. Each layer of snow accumulated on the surface of a glacier stores a sample of the impurities present in the atmosphere. For example, isotopic ratios $^{18}O/^{16}O$ or D/H reflect

the temperature at which the vapor was transformed into ice [6], the acidity provides information about volcanic eruptions [7], etc. The deeper we look into an ice core, the farther back in time we sample the atmosphere.

Since these ice deposits have been sitting for such a long time, the diffusion of water molecules in the ice places a limit on the time resolution that can be obtained. With a clear understanding of the diffusion mechanism and quantitative estimates of the diffusivity, these effects could be corrected by reverse diffusion calculations [8, 9]

Another situation where the surface diffusion mechanism plays an important role is in the growth of ice crystals. The richness of growth habits indicates that the surface dynamics are complex. It has been hypothesised [10] that surface diffusion plays an important role here. The different growth modes regulate the size and shape of ice crystals in clouds that in turn determine the radiative and hydrological fluxes and chemical compositions of the troposphere [11]. There are still gaps in quantitative understanding of ice clouds that affect the forecast of the response of clouds. For example, one of the large puzzles is that the observed concentration of small ice crystals in clouds is orders of magnitude higher than would be expected from the abundance of heterogeneous nucleation particles [12].

The presence of a liquid layer on the surface of ice, at temperatures below the bulk melting temperature, was suggested in the last century by Faraday but is still subject of theoretical and experimental studies [13, 14]. The presence of a liquid layer on the surface of ice could have important consequences on the charge transfer between two colliding ice crystals and clouds electrification [15] and have important consequences for the onset of melting [16].

A few attempts have been made to measure surface diffusion of water molecules on ice [5, 17, 18, 19, 10]. Clear conclusions can still not be drawn from the available experimental data. Bulk diffusion is also not well understood.

Artificial single crystals revealed crystal edge effects that were associated with surface diffusion [18]. Brown and George [5] attempted to measure surface diffusion, but did not obtain a measurable signal from their apparatus. Their experiment provides an upper bound to the diffusivity of molecules on the surface. These are very difficult measurements because of the two dimensional nature of the problem. In an interesting experiment Mason estimated the mobility of molecules on the surface of ice by observing two approaching steps on the surface [19, 10]. The advance of the steps is fed by molecules adsorbed on the surface, diffusing on the terrace until they bind to the edge. Mason *et al* could observe that two approaching steps slowed down when they were close enough, and they interpreted this in terms of a competition between the two advancing steps for the admolecules on the surface. The separation of the steps at the time that their speeds drop then gives the distance that a molecule on the surface travels before desorbing, *i.e.* the diffusion length.

We decided to study surface diffusion by computer simulations. Since *ab initio* calculations are still far too expensive to be applied to this problem, the project involved developing a semi-empirical potential that could reproduce the interaction between the molecules. Molecules on the surface of a crystal, or molecules at a transition state for a diffusion hop, are in an environment that is neither characteristic of ice nor water vapor. Most H_2O potential functions available in the literature are developed to simulate either condensed phase or small water clusters. The potential functions developed to reproduce condensed phase properties [20, 21, 22, 23, 24] are mostly taylored to reproduce liquid water properties, but little attention has been given to crystalline ice. Some potentials are primarily fitted to properties of the water dimer [25, 26, 27] and do not work well for ice. We needed a potential function that could reproduce the interaction between water molecules at the surface of ice, which in a sense is intermediate between condensed phase and a small cluster. It is therefore

essential that we have a potential function that is transferable to different kinds of environments.

This thesis is divided in two parts. Chapters 2 through 7 discuss the development of our potential function and the remaining chapters discuss the application of this potential to the study of molecular processes at the ice surface.

In Chapter 2 we study the multipole moment of water molecules in ice I_h. Induction effects of 67% are observed in the dipole moment. We also revise the well-quoted calculation by Coulson and Eisenberg [28], finding that the discrepancy is due to their use cf less accurate values for the molecular multipoles of an isolated water molecule.

In Chapter 3 we present a study of the multipole moments of water molecules in ice and in water clusters. The molecular multipole moments were extracted from the charge density obtained from *ab initio* calculations using various schemes for dividing the electronic charge density among the water molecules, including Bader's zero flux surfaces and simple Voronoy partition schemes. The *ab initio* molecular multipoles are compared with results from an induction model where the molecules are represented with multipole moments and polarizabilities up to second order. We find that the values of the molecular multipole moments are ill-defined; a small change in the definition of a 'molecule' in the system leads to large changes in the deduced molecular moments.

In Chapter 4 we study the electric field near water clusters and in ice I_h using first principles calculations. We used Density Functional Theory with a gradient dependent functional (DFT/PW91) for ice I_h as well as the clusters and also used, for comparison, the Moller-Plesset perturbation theory (MP2) results of Xantheas for the clusters. The electric field obtained from these first principles calculations was used to test the predictions of the induction model

based on single center multipole moments and polarizabilities of an isolated water molecule. We found that the fields obtained from the induction model agree well with the first principles results when the multipole expansion is carried out up to and including the hexadecapole moment and when polarizable dipole and quadrupole moments are included. The molecular multipole moments presented in Chapter 3 were also used to study the rate of convergence of the electric field as function of the order of the multipole expansion. The induction model was found to give an electric field that agrees well with the *ab initio* calculations and can, therefore, be used to model the intermolecular interactions accurately.

Chapter 5 gives a detailed account of the potential model, including expressions for forces and torques to help implement the potential. Supported by the previous two chapters, we will adopt a one-center multipole representation with a multipolar expansion up to electric hexadecapole moment.

Chapter 6 explains the fitting procedure for the adjustable paramenters in our potential function. We explain in this chapter how we interpolate between the gas phase, clusters and the condensed phase (ice) to develop a transferable potential function. A comparison of the prediction of this potential with *ab initio* calculated clusters is presented in Chapter 7.

In Chapter 8 we present the applications. We present theoretical calculations of the adsorption, diffusion, and island formation of water admolecules on the basal plane surface of an ice I_h crystal. We map and classify the binding sites of admolecules on the surface of ice I_h. Since ice I_h is proton disordered, no two sites are exactly the same and there is a wide range of binding energies. The proton disorder also results in a range of activation energies for diffusion. After mapping out a large number of diffusion barriers using the Nudged Elastic Band method, a kinetic Monte Carlo calculation of the diffusion for a range of temperatures was performed to extract the effective diffusivity on the pro-

ton disordered surface. The energetics and dynamics of the formation of small islands on the ice surface have also been studied. It is found that islands up to and including pentamer are non-crystallographic, but the hexamer is crystallographic. While the formation of a crystallographic hexamer from a non-crystallographic pentamer and a new admolecule involves a complex concerted motion of all the island molecules and a large relaxation of the substrate, the activation energy for the process is estimated to be quite small, smaller than the admolecule diffusion barrier.

Chapter 2

MOLECULAR MULTIPOLE MOMENTS OF WATER MOLECULES IN ICE I_h

2.1 Abstract

We have used an induction model including dipole, dipole-quadrupole, quadrupole-quadrupole polarizability and first hyperpolarizability, as well as fixed octopole and hexadecapole moments to study the electric field in ice. The self-consistent induction calculations gave an average total dipole moment of 3.09 D, a 67% increase over the dipole moment of an isolated water molecule. A previous, less accurate induction model study by Coulson and Eisenberg [Proc. R. Soc. Lond. A **291**, 445 (1966)] suggested a significantly smaller average value of 2.6 D. This value has been used extensively in recent years as a reference point in the development of various polarizable interaction potentials for water, as well as for assessment of the convergence of water cluster properties to those of bulk. The reason for this difference is not due to approximations made in the computational scheme of Coulson and Eisenberg but rather due to the use of less accurate values for the molecular multipoles in these earlier calculations.

2.2 Introduction

An understanding of the properties of water and ice requires a quantitative description of the electric field created collectively by the water molecules and the influence the field can have on the atomic scale structure and dynamics. It

is, for example, expected that the dipole moment of a water molecule in liquid water is significantly larger than the dipole moment of an isolated water molecule, which has been experimentally measured to be 1.855 D [29]. The dipole moment of a water molecule in a condensed phase environment cannot be measured directly, but estimates based on the measured dielectric constant of water and assuming the molecules can be represented by dipole moments only indicate an increase of the molecular dipole moment by 0.6 D – 1.2 D [30, 31]. The change in molecular electric properties due to the local environment is, in particular, important for the development of accurate intermolecular potential functions describing water-water and water-solute interactions. While most of the attention has been focused on the dipole moment, it is clear that the quadrupole moment is also important for accurately describing the molecular interactions [27] and the macroscopic dielectric constant [32].

Ice is a natural starting point for systematically studying these issues since, apart from the proton disorder in ice I_h, the molecular structure is known. Liquid water has the additional complexity of irregular and poorly known ordering of the molecules. Over thirty years ago, Coulson and Eisenberg [28] carried out an ingenious calculation of the dipole moment in ice I_h using an induction model. Their calculation gave a net molecular dipole moment of 2.6 D. Unfortunately, their numerical result has frequently been misrepresented. Several authors have incorrectly quoted the paper by Coulson and Eisenberg as giving the molecular dipole moment in liquid water or, as giving the results of a measurement of the dipole moment in ice, or even as giving an experimental measurement of the molecular dipole moment in liquid water. These misquotations seem to perpetuate in the water modeling literature of recent years.

We describe here more accurate and detailed calculations that lead to a significantly larger molecular dipole moment in ice than the one obtained by Coulson and Eisenberg. Our calculations include several higher order terms in the

multipolar expansion and do not make some of the approximations invoked in the induction calculations of Coulson and Eisenberg. The self-consistent multipole iterative scheme that we employed, as well as the input parameters for the molecular multipoles, are described in Section 2.3. Otherwise, the results of high level *ab initio* calculations have been used. Our results are presented in Section 2.4. We address the differences between our calculations and those of Coulson and Eisenberg in Section 2.5. In view of the widespread confusion in the literature about their work, we describe their calculations in considerable detail. Our conclusions are presented in Section 2.6.

2.3 Multipole Iterative Method

The starting point of our calculations is the construction of a hexagonal lattice of water molecules representing ice I_h. For the oxygen-oxygen separation we used 2.76 Å, a value consistent with the measured density at 273 K [33]. It is well established that while the oxygen atoms are ordered on a lattice, the protons are to a certain extent disordered, but still follow the "ice rules" [34, 35], namely that (1) there is one and only one hydrogen atom between each pair of adjacent oxygen atoms, and (2) each oxygen atom has two hydrogens at a close distance (ca. 1.0 Å, covalently bonded) and two hydrogens at a larger distance (ca. 1.75 Å, hydrogen bonded).

The calculations were carried out as follows. A configuration of 2,592 water molecules was generated following the ice rules, filling a $40.6 \times 46.9 \times 44.2$ Å^3 simulation box. Periodic boundary conditions were imposed in all three directions to simulate a bulk ice environment. We generated an ice lattice: a 96 molecule unit cell with proton disorder, zero total dipole moment and periodic boundary conditions satisfied in all three directions. We followed the same procedure as Kroes [14]. This cell was periodically repeated three times in each direction

to generate the simulation box. The degree of randomness of the ice lattices generated by this method and by other methods was studied by Hayward and Reimers [36]. In the notation of Hayward and Reimers we generated a "3×2×2" lattice with constraints of the "C2" type. The randomness is characterized by the dipole-dipole autocorrelation coefficients ϕ_n for the n-th coordination shell that has radius r_n, defined as

$$\phi_n = \frac{\sum_{i=1}^{N} \sum_{j=i}^{i} \vec{\mathcal{P}}^{(i)} \cdot \vec{\mathcal{P}}^{(j)} \, \delta(R_{ij} - r_n)}{\sum_{i=1}^{N} \sum_{j=i}^{i} \delta(R_{ij} - r_n)} \tag{2.1}$$

where R_{ij} is the distance between dipoles and $\vec{\mathcal{P}}$ is the dipole moment vector. In our simulation cell $\phi_1 = 0.227$, $\phi_2 = -0.03$, $\phi_3 = -0.179$ and $\phi_4 = -0.015$.

The electric field at a molecule is the sum of the fields produced by its neighbors. In order to systematically study the effect of distant neighbors, only those closer than a given cutoff distance r_{cut} were included in the calculation of the electric potential. The full calculation was then repeated with different values of r_{cut}, up to 20 Å. It turns out (see Section 2.4) that it is sufficient to use $r_{\text{cut}} = 7$Å.

When calculating the electric field, each molecule was represented with a point dipole, quadrupole, octopole and a hexadecapole moment tensor at the center of mass. The electric field at a molecule due to its neighbors then induces both a dipole moment and a quadrupole moment in the molecule. The i-th component of the induced dipole moment is given by [37]

$$\Delta\mathcal{P}_i = \alpha_{ij} \, E_j + \frac{1}{3} \, A_{i,jk} \, \frac{\partial E_j}{\partial r_k} + \frac{1}{2} \, \beta_{ijk} \, E_j \, E_k \tag{2.2}$$

where E is the total electric field (cf. Appendix A), α_{ij} is the molecular dipole polarizability, $A_{i,jk}$ the dipole-quadrupole polarizability, and β_{ijk} the first hyperpolarizability. The repeated indices are to be summed over.

The induced quadrupole moment of the molecule is [37]:

$$\Delta\mathcal{Q}_{ij} = A_{k,ij} \, E_k + C_{ij,kl} \, \frac{\partial E_k}{\partial r_l} \tag{2.3}$$

where $C_{ij,kl}$ is the quadrupole-quadrupole polarizability.

Equations (2.2) and (2.3) are implicit equations of $\mathcal{P}_i$ and $\mathcal{Q}_{ij}$. A given molecule polarizes its neighbors and these neighbors in turn induce extra dipole and quadrupole. Since the effect is non-linear, an iterative procedure is used to solve the equations.

A first order correction to the dipole moment of each molecule is induced by the total electric field of the neighboring unpolarized molecules

$$\Delta\mathcal{P}_i^{(1)} = \alpha_{ij}\, E_j^{(0)} + \frac{1}{3}\, A_{i,jk}\, \frac{\partial E_j^{(0)}}{\partial r_k} + \frac{1}{2}\, \beta_{ijk}\, E_j^{(0)}\, E_k^{(0)} \tag{2.4}$$

and also a first order correction to the quadrupole moment is induced

$$\Delta\mathcal{Q}_{ij}^{(1)} = A_{k,ij}\, E_k^{(0)} + C_{ij,kl}\, \frac{\partial E_k^{(0)}}{\partial r_l} \tag{2.5}$$

The first order induced dipole moments create an additional electric field $\vec{E}_d^{(1)}$ and the induced quadrupole moments generate $\vec{E}_q^{(1)}$. The total first order correction field, $\vec{E}^{(1)} = \vec{E}_d^{(1)} + \vec{E}_q^{(1)}$ induces a second order correction to the dipole moments of

$$\Delta\mathcal{P}_i^{(2)} = \alpha_{ij}\, E_j^{(1)} + \frac{1}{3}\, A_{i,jk}\, \frac{\partial E_j^{(1)}}{\partial r_k} + \frac{1}{2}\, \beta_{ijk}\, E_j^{(1)}\, E_k^{(1)} \tag{2.6}$$

and a second order correction to the quadrupole moments of

$$\Delta\mathcal{Q}_{ij}^{(2)} = A_{k,ij}\, E_k^{(1)} + C_{ij,kl}\, \frac{\partial E_k^{(1)}}{\partial r_l}. \tag{2.7}$$

The new induced multipoles in turn, create an additional electric field $\vec{E}^{(2)}$. This procedure was continued until the magnitude of the n-th induced dipole,

$$\Delta\mathcal{P}_i^{(n)} = \alpha_{ij}\, E_j^{(n-1)} + \frac{1}{3}\, A_{i,jk}\, \frac{\partial E_j^{(n-1)}}{\partial r_k} + \frac{1}{2}\, \beta_{ijk}\, E_j^{(n-1)}\, E_k^{(n-1)} \tag{2.8}$$

and quadrupole moments

$$\Delta\mathcal{Q}_{ij}^{(n)} = A_{k,ij}\, E_k^{(n-1)} + C_{ij,kl}\, \frac{\partial E_k^{(n-1)}}{\partial r_l} \tag{2.9}$$

became smaller than a given tolerance, 10^{-6} D and 10^{-6} DÅ, respectively. Thus, self-consistency was obtained up to this level of accuracy. An ensemble average was obtained by averaging the induced dipole of each of the 2,592 water molecules in the simulation cell. Due to the proton disorder, both the magnitude and the direction of the local electric field at a molecule varies, as discussed below.

Ab-initio-calculated multipole moments for a water molecule up to hexadecapole as well as experimental values for the dipole [29] and quadrupole moments [1], are given in Table 2.1. The second column corresponds to MP2 level calculations with the aug-cc-pVQZ basis set at the minimum energy configuration (O-H distance 0.9590 Å and H-O-H angle 104.28 degrees) [3].

The column labeled GC in Table 2.1 correspond to the values of Glaeser and Coulson [2] which were used in the induction model calculation of Coulson and Eisenberg [28]. The GC multipoles were originally reported with respect to the oxygen atom, but in order to make the comparison with the other multipole values easier, we have translated them to a coordinate system with origin at the center of mass (see the Appendix B). The GC multipole moments were taken from a calculation by McWeeny and Ohno [38] using a very limited basis set, consisting of just seven atomic orbitals: an oxygen core orbital, two lone pair orbitals, two hydrogen orbitals and two bond orbitals. At the time Coulson and Eisenberg did their calculations experimentally measured values were not available.

It is evident from Table 2.1 that the results of these early *ab initio* calculations are in poor agreement with the experimentally measured values, especially for the quadrupole moment. The numerical values of the multipoles used as input in the induction model calculations are, in fact, very important in determining the resulting induced dipole moments, as discussed in Section 2.5.

Table 2.1: Multipole moments of a water molecule used in the self-consistent induction calculations and comparison with values used in previous calculations. The moments are computed using the definitions given in Appendix B. The origin of the coordinate system is located at the center of mass of the molecule. The experimental values for the quadrupole moment are from reference [1]. GC denote the multipole moments of Glaeser and Coulson [2] (which were used by Coulson and Eisenberg in their calculations). MP2 are the multipole moments calculated from the charge density from MP2 *ab initio* calculation [3]

		Exp	MP2	GC	
Dipole	$\mathcal{P}_3$	-1.855	-1.86	-1.76	$\times 10^{-18}$ e.s.u. cm
Quadrupole	$\mathcal{Q}_{33}$	-0.13	-0.1328	0.142	$\times 10^{-26}$ e.s.u. cm^2
	$\mathcal{Q}_{11}$	2.63	2.6135	0.961	
	$\mathcal{Q}_{22}$	-2.50	-2.4807	-1.103	
Octopole	$\mathcal{O}_{333}$		1.3565	0.470	$\times 10^{-34}$ e.s.u. cm^3
	$\mathcal{O}_{113}$		-2.3288	-0.851	
	$\mathcal{O}_{223}$		0.9723	0.381	
hexadecapole	$\mathcal{H}_{3333}$		-1.3637		$\times 10^{-42}$ e.s.u. cm^4
	$\mathcal{H}_{1133}$		1.6324		
	$\mathcal{H}_{2233}$		-0.2687		
	$\mathcal{H}_{1111}$		-0.3575		
	$\mathcal{H}_{1122}$		-1.2749		
	$\mathcal{H}_{2222}$		1.5436		

Our induction model calculations made use of the experimentally measured dipole and quadrupole moments. For the octopole and hexadecapole moments, we used the values computed at the MP2/aug-cc-pVQZ level of theory, listed in Table 2.1. The agreement of the dipole and quadrupole moments at the MP2/aug-cc-pVQZ level of theory with the experimental ones justifies the use of the higher moments (octopole and hexadecapole) computed at this level of theory. Additionally, the induction calculations made use of the experimentally measured molecular dipole polarizability, α_{ij} [39]. Results of previous *ab initio* calculations were used for the values of the dipole-quadrupole, $A_{i,jk}$, the quadrupole-quadrupole polarizability, $C_{ij,kl}$ [40], and the first hyperpolarizability, β_{ijk} [41]. The values that we used for the polarizabilities are given in Table 2.2.

2.4 Results

The average molecular dipole moment obtained in the self-consistent induction calculation is shown in Figure 2.1. as a function of the cutoff radius, r_{cut}. Clearly, the calculation has converged at $r_{\text{cut}} = 7$ Å. The converged value of the dipole moment is 3.09 D. The error bars shown in Figure 2.1 correspond to the variation among the molecules in the sample. Due to the proton disorder, no two molecules are in exactly the same environment. For a 20 Å cutoff, the standard deviation in the dipole moment is 0.03 D.

Figure 2.2 shows the magnitude and direction of the various components of the electric field at a typical molecule. The length of an arrow represents the magnitude of the electric field component averaged over the molecules in the sample: The induced quadrupole moment produces 20% of the quadrupole field, while the induced dipole moment accounts for 40% of the total field generated by the dipoles. The effect of the self-consistency in the calculation is significant:

Table 2.2: Values of the polarizabilities used in the self-consistent induction calculations. All quantities are expressed in atomic units ($[\alpha_{ij}] = a_0^3$, $[\beta_{ijk}] = a_0^6/e\ a_0$, $[A_{i,jk}] = a_0^4$ and $[C_{ij,kl}] = a_0^5$). The coordinate reference frame of the molecule is the one defined in Section 5.1

α_{11}	9.907±0.02
α_{22}	10.311±0.088
α_{33}	9.549±0.088
$\alpha_{\text{isotropic}}$	9.922
β_{111}	5.4715
β_{122}	0.5445
β_{133}	10.029
$A_{1,11}$	-1.355
$A_{1,22}$	4.754
$A_{1,33}$	-3.399
$A_{2,12}$	-8.258
$A_{3,13}$	2.477
$C_{11,11}$	28.632
$C_{11,22}$	-16.389
$C_{11,33}$	-12.243
$C_{12,12}$	18.869
$C_{13,13}$	31.540
$C_{22,22}$	28.043
$C_{22,33}$	-11.654
$C_{23,23}$	16.907
$C_{33,33}$	23.897

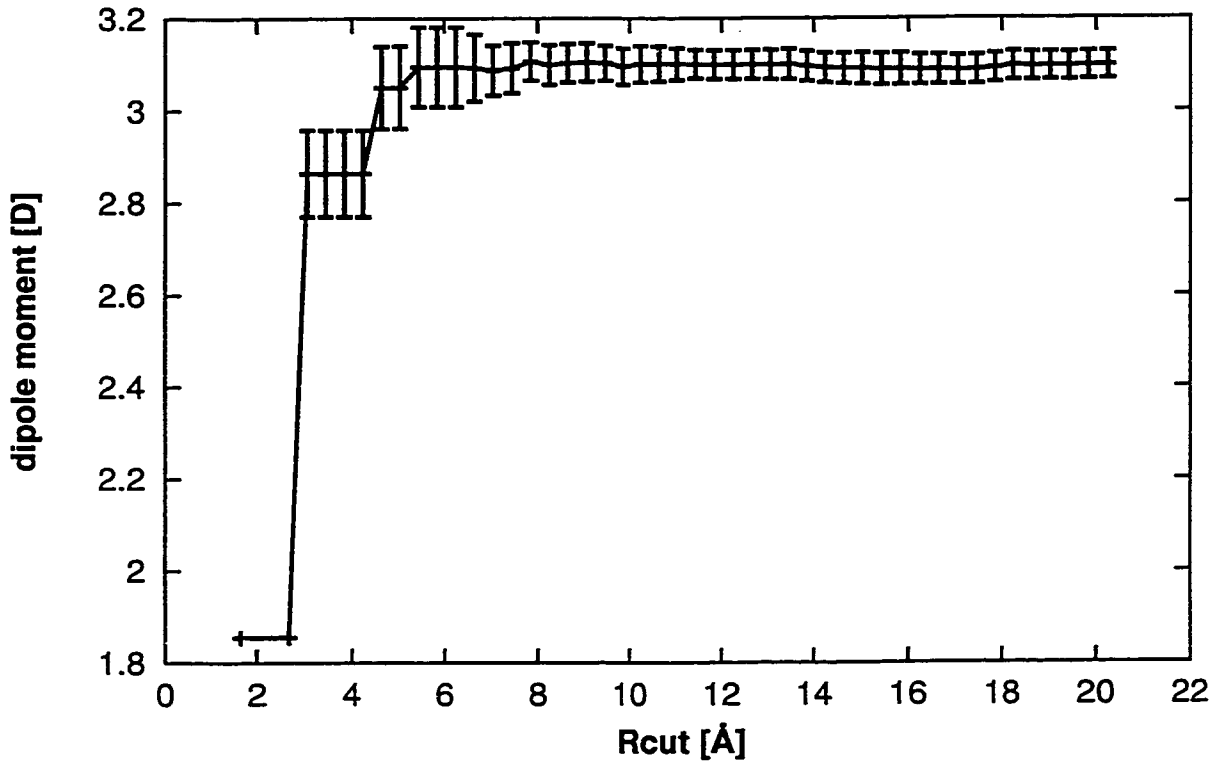

Figure 2.1: Convergence of the calculated molecular dipole moment as a function of the cut-off distance used in summing up the electric potential due to the neighbors. The error bars correspond to the fluctuations due to the different environments seen by the various molecules in the proton disordered ice I_h. The results show that it is sufficient to include only neighbors that are closer than 7 Å when evaluating the electric field at a given molecule.

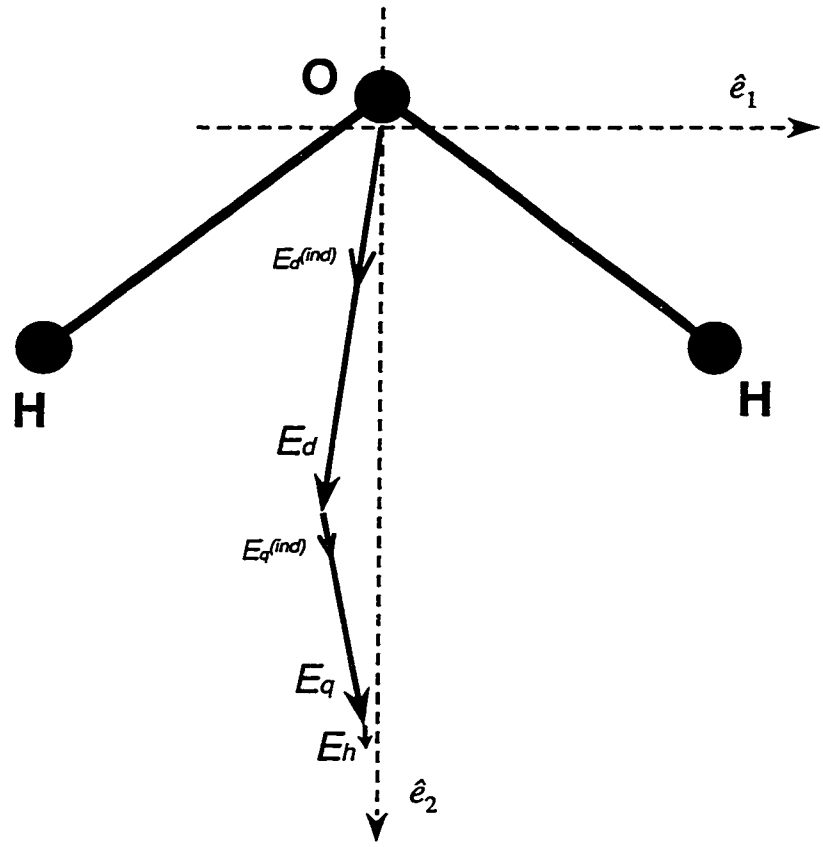

Figure 2.2: Various components of the local electric field at a typical molecule showing the magnitude and direction of the field with respect to the bisector of the molecule. The length of each arrow represents the magnitude of the electric field components averaged over all molecules in the ice sample. The dipole field vector is labeled E_d, the quadrupole field E_q, and the field due to higher multipoles E_h (octopolar plus hexadecapolar field). The angle between the arrows and the bisector of the molecule is the average of the polar angle of the electric field component when choosing the bisector as polar axis. The smaller superimposed arrows $E_d^{(ind)}$ and $E_q^{(ind)}$ are the electric fields due to the induced parts of the dipoles and quadrupoles. Even though the direction of the individual electric field components deviates somewhat from the direction of the bisector, the total field (and the induced dipole moment) to a good approximation pointing along the bisector.

The dipole after the first iteration is only 2.70 D and it increases by 14% in subsequent iterations. The dipolar and quadrupolar fields increase by 15% and 6%, respectively, in the second and subsequent iterations.

A large value for the induced quadrupole moment was obtained. The principal axes of the total quadrupole moment are almost the same as those of the free molecule. The angle between the original axes and the new principal axes is always less than 0.5°, with an average value of 0.15°. The average eigenvalues of the quadrupole moment are $(Q_{11}, Q_{22}, Q_{33}) = (3.29, -3.14, -0.15) \times 10^{-26}$ e.s.u. cm^2, an increase of 25%, 26% and 14%, respectively, over the value for an isolated molecule.

In order to quantify the effect of the dipole-quadrupole polarizability, $A_{i,jk}$, the quadrupole-quadrupole polarizability, $C_{ij,kl}$, the first hyperpolarizability, β_{ijk}, and the hexadecapole field, we calculated the induced dipole moment ignoring these contributions one at a time. We find that the dipole-quadrupole and the quadrupole-quadrupole polarizabilities have a significant and opposite effect. If $A_{i,jk}$ and $C_{ij,kl}$ are not taken into account, *i.e.*, when there are no induced quadrupole moments, the total dipole moment is predicted to be 3.05 D, which is 0.04 D smaller than the result of the full calculation. After including $A_{i,jk}$ the total dipole is 2.99 D and after including the quadrupole-quadrupole polarizability, $C_{ij,kl}$, the result is 3.09 D. Ignoring the nonlinear effects introduced by β_{ijk} we obtain a dipole moment of 3.10 D, showing that the effect of this correction is very small. Suppressing the hexadecapole moments had a small but significant effect. The total dipole moment predicted with a multipole expansion up to octopole is 3.04 D.

The above results are summarized in Table 2.3 for the various levels of molecular multipolar expansions ($\mathcal{P}, \mathcal{Q}, \mathcal{O}, \mathcal{H}$) and increasing levels of response to multipolar fields.

The anisotropy of the dipole polarizability was tested by using only the

Table 2.3: Calculated values for the molecular dipole moment of water in ice I_h at the various levels of the multipolar expansion and increasing levels of response to multipolar fields within the self-consistent induction scheme. All the dipole moments are expressed in Debye.

Expansion	α	α, A	α, A, C	α, A, C, β
$\mathcal{P}, \mathcal{Q}$	2.94	2.89	2.98	2.97
$\mathcal{P}, \mathcal{Q}, \mathcal{O}$	3.00	2.94	3.04	3.04
$\mathcal{P}, \mathcal{Q}, \mathcal{O}, \mathcal{H}$	3.05	2.99	3.10	3.09

isotropic component of the polarizability. Averaging the induced dipole moment over all possible directions of the electric field gives the average of the three eigenvalues of the anisotropic tensor. The anisotropy of the polarizability is quite important. The dipole induced with the isotropic part is 3.16 D, larger by 0.07 D than the dipole induced with the full anisotropic polarizability.

In the calculations of Coulson and Eisenberg, discussed below, the simplifying approximation is made that the dipolar component of the total electric field at each molecule points in the direction of the bisector of the molecule. We tested this assumption in our calculations and the results are shown in Figure 2.2. For each molecule in the sample, we defined the polar axis as the bisector of the molecule and evaluated the polar angle of the various electric field vectors. The average values of the polar angles are indicated by the arrows in Figure 2.2. The electric field due to the dipoles alone is as much as 16° off the bisector axis (with an average polar angle of 7°). However, the total electric field at a molecule lies very nearly along the direction of the bisector, with a maximum polar angle of 1.7° and a mean value of 0.7°. Even though the direction of the individual components deviates from the direction of the bisector of the molecule, the total field and the induced dipole moment are to a

good approximation pointing along the bisector.

2.5 The Method of Coulson and Eisenberg

We now review the induction calculation carried out by Coulson and Eisenberg. As noted earlier, the results of their calculation are still very widely referred to but are frequently misrepresented.

Coulson and Eisenberg included a molecular dipole moment, quadrupole moment and octopole moment, as well as an isotropic dipole polarizability in their model. The total electric field at a molecule was divided into two parts: The field produced by the dipoles, $\vec{E}_d$, and the field produced by the higher order multipoles (quadrupoles and octopoles), $\vec{E}_h$. The total field at a given molecule due to neighbors within a 9.6 Å radius induced a dipole moment given by

$$\Delta\vec{\mathcal{P}}^{(1)} = \alpha\vec{E} = \alpha\,(\vec{E}_d + \vec{E}_h) \tag{2.10}$$

where α is the isotropic molecular polarizability. A value of $\alpha = 1.59$ Å^3 was used in their calculations (induced quadrupoles or hyperpolarizabilities were not taken into account). An interesting simplifying assumption was made by Coulson and Eisenberg that enabled them to analytically sum up the iterative induction calculation to infinite order. The total dipole field, $\vec{E}_d$, at a molecule was assumed to be parallel to the unpolarized dipole moment ($\vec{\mathcal{P}}^{(0)}$) of the molecule

$$\vec{E}_d = c\,\vec{\mathcal{P}}^{(0)} \tag{2.11}$$

where c is a constant of proportionality. The first order correction to the dipole then becomes

$$\Delta\vec{\mathcal{P}}^{(1)} = \alpha\,(c\,\vec{\mathcal{P}}^{(0)} + \vec{E}_h) = \alpha\,c\left(\vec{\mathcal{P}}^{(0)} + \frac{\vec{E}_h}{c}\right). \tag{2.12}$$

Assuming that all the molecules in the bulk are equivalent, the same dipole moment is induced in all the molecules. The induced dipole moment in all the surrounding molecules then generates an extra dipole field, $\vec{E}_d^{(1)}$, proportional to the first order correction of the dipole moment,

$$\vec{E}_d^{(1)} = c\,\Delta\vec{\mathcal{P}}^{(1)}, \tag{2.13}$$

that induces a second order correction to the dipole moment

$$\Delta\vec{\mathcal{P}}^{(2)} = \alpha\vec{E}_d^{(1)} = (\alpha\,c)^2\,\left(\vec{\mathcal{P}}^{(0)} + \frac{\vec{E}_h}{c}\right). \tag{2.14}$$

The n-th order correction to the dipole moment is

$$\Delta\vec{\mathcal{P}}^{(n)} = \alpha\,\vec{E}_d^{(n-1)} = \alpha\,c\,\Delta\vec{\mathcal{P}}^{(n-1)} = (\alpha\,c)^n\,\left(\vec{\mathcal{P}}^{(0)} + \frac{\vec{E}_h}{c}\right) \tag{2.15}$$

and the total induced dipole moment is

$$\Delta\vec{\mathcal{P}} = \sum_{n=1}^{\infty}\Delta\vec{\mathcal{P}}^{(n)} = \left(\vec{\mathcal{P}}^{(0)} + \frac{\vec{E}_h}{c}\right)\,\sum_{n=1}^{\infty}(\alpha\,c)^n \tag{2.16}$$

$$\Delta\vec{\mathcal{P}} = \frac{\alpha\,c}{1-\alpha\,c}\,\left(\vec{\mathcal{P}}^{(0)} + \frac{\vec{E}_h}{c}\right) = \frac{\alpha}{1-\alpha\,c}\,(\vec{E}_d + \vec{E}_h) \tag{2.17}$$

$$\Delta\vec{\mathcal{P}} = \frac{|\vec{\mathcal{P}}^{(0)}|\,\alpha\,\vec{E}}{|\vec{\mathcal{P}}^{(0)}| - \alpha\,|\vec{E}_d|}. \tag{2.18}$$

Thus, by making a simplifying assumption about the direction of the induced dipole, Coulson and Eisenberg were able to calculate analytically the total induced dipole moment in a bulk molecule in terms of the multipoles of the isolated molecule and the dipole polarizability.

After averaging over the possible orientations of each molecule in a configuration of molecules satisfying the ice rules, Coulson and Eisenberg predicted a total dipole moment of 2.6 D for the water molecule in ice I_h. This number

represents an average over different arrangements of protons, with some orientations resulting in molecular dipole moments as low as 1.9 D and others as high as 3.1 D. This result is significantly smaller than the value of 2.95 D that we obtain using a more elaborate scheme and the question naturally arises as to what the important difference is.

We repeated our numerical induction calculation using the same input parameters as Coulson and Eisenberg (multipoles and molecular polarizability), neglecting dipole-quadrupole polarizability, hyperpolarizability and the hexadecapole moment of the molecule. Using a system size similar to theirs that includes 121 molecules and averaging over 50 configurations, we obtained a net dipole moment of 2.65±0.08 D, in good agreement with the result of Coulson and Eisenberg. This shows that the simplifying assumption made in their calculation, namely that the total dipole field is parallel to the permanent dipole moment of the molecule, Eq. (2.11), is in fact sufficient. This is also evident from the analysis of our results, presented in Section 2.4, which show that although the field does not lie exactly along the bisector of the molecule, the deviations are effectively small.

We then repeated the calculation, now including the experimentally determined dipole and quadrupole moments and dipole polarizability, and the MP2 calculated octopole and hexadecapole moments as given in Tables 2.1 and 2.2. The resulting net dipole moment was 3.04±0.04 D. This shows that the low value obtained by Coulson and Eisenberg is a result of the numerical values of the multipole moments they used as input in their model.

2.6 Conclusions

We have used a self-consistent induction model to study the electric field in ice and found that the best estimate for the dipole moment of a water mole-

cule in ice I_h is 3.09 D. This value represents a 67% increase over the dipole moment of an isolated water molecule. Our estimate is significantly higher than the one reported earlier by Coulson and Eisenberg who also used a similar but more approximate induction model. The main reason for the difference between our results and the earlier estimates lies in the numerical values for the quadrupole moment of the isolated molecule. Coulson and Eisenberg relied on the best estimates of multipole moments from first principle calculations at the time, which included a very small basis set. We have used the experimental values for the dipole and quadrupole moments (the latter obtained after Coulson and Eisenberg carried out their calculation) and the results of accurate *ab initio* calculations for the higher octopole and hexadecapole moments. When the same set of multipoles are used as input, the method of Coulson and Eisenberg gave results very similar to our more detailed model, indicating that the approximations used by Coulson and Eisenberg to simplify the induction calculations are quite valid.

The multipole expansion for the electric field in the ice crystal was carried out to what seems to be a reasonably good convergence. As an indicator of the effect of various terms in the expansion, we have focused on the net dipole and quadrupole moment per molecule obtained in the self-consistent calculation. The inclusion of dipole-quadrupole and quadrupole-quadrupole polarizabilities has small but significant effect on the dipoles; it increases the dipole moment of the water molecules by 0.04 D. These polarizabilities have a more dramatic effect on the quadrupoles, increasing the magnitude by 14% to 25%, depending on the component. It is important to go beyond the quadrupole and include also the (fixed) octopole moment of the molecules. This increases the net dipole moment by 0.07 D. The hexadecapole moment, however, has a small effect on the dipole moment (increasing it by 0.05 D).

A remarkable feature in the self-consistent calculations is how little effect

distant neighbors have on the field at a given molecule. It is sufficient to include the electric field from neighbors within a 7 Å radius in order to get the converged, large system value of the induced dipole moment to 99% (see Figure 2.1), as was already done by Coulson and Eisenberg. This is, in fact, not true when the molecules are modeled by point charges, as is most frequently done in simulation studies of water and water solutions.

Chapter 3

MULTIPOLE MOMENTS OF WATER MOLECULES IN CLUSTERS AND ICE I_h FROM FIRST PRINCIPLES CALCULATIONS

3.1 Abstract

We obtained *molecular* multipole moments for water molecules in clusters and in ice I_h by partitioning the charge density obtained from first principles calculations. Various schemes for dividing the electronic charge density among the water molecules were used. They include Bader's zero flux surfaces and simple Voronoy partition schemes. These results were also compared with the ones obtained from an induction model that includes dipole, dipole-quadrupole, quadrupole-quadrupole polarizability and first hyperpolarizability, as well as fixed octopole and hexadecapole moments. We have found that the different density partitioning schemes lead to widely different values for the molecular multipoles, illustrating how poorly defined molecular multipoles are in clusters and condensed environments. For instance, the magnitude of the molecular dipole moment in ice I_h ranges between 2.3 D and 3.1 D, depending on the scheme used.

3.2 Introduction

Molecular systems are often described in terms of properties of the individual molecules and their interactions [42, 43]. These molecular properties are,

in general, environment-dependent and can, for example, be significantly different in a condensed environment than in a gas phase environment. It is interesting to investigate how such molecular properties evolve gradually in clusters of increasing size. Water is a particularly important example of such a system. Clusters of water molecules have been used to probe important properties of water and ice, such as cooperative [44, 45], structural [46] and electrical trends [47, 48]. These properties serve as important benchmarks in the development and parametrization of interaction potentials for water molecules. For instance, some of the most sophisticated potential functions for water include a molecular point dipole that is evaluated self-consistently via an induction scheme [27, 49, 50]. Therefore, the *molecular* dipole moment of water has received a great deal of attention and there have been many previous studies of the dipole moment of water molecules in various environments, ranging from clusters to liquid water and ice (see, for example, refs. [47, 48, 50, 28, 30, 31, 51, 52, 53, 54, 55, 56, 3]). As a general rule, the molecular dipole moment increases as a result of the interaction with other, neighboring water molecules.

The dipole moment of water molecules in ice was studied a long time ago using a simple induction model[28]. In a recent study [47], molecular dipole moments of water clusters up to the hexamer were obtained using a distributed multipole analysis (DMA) method [57, 58]. The results indicated that the molecular dipole moment of the water hexamer is very similar to that of ice I_h and it was inferred that the dominant interactions that occur in condensed-phase environments are reasonably well represented in clusters even this small (hexamer) [47]. This is an unexpected result, because water molecules in ice have many more neighbors than water molecules in a hexamer cluster. We have recently re-evaluated the molecular dipole moment in ice I_h using the induction model [3] and obtained 3.1 D, a value significantly larger than the previously

reported one [28], 2.6 D. We have attributed this difference to the use of less accurate values for the molecular quadrupole moment in the previous calculation, as experimental values for this quantity were not yet available at the time of that study. Our value for the molecular dipole moment in ice I_h is 0.4 Debye larger than the one previously obtained for the water hexamer with both the induction and DMA methods [47], a fact that suggests that the dipole moment increase for the hexamer is not of a similar magnitude as that of ice I_h. Nevertheless, the importance of this issue for the development of water potentials warrants further studies that treat both water clusters and ice I_h on the same theoretical footing and therefore allow for a direct comparison of the results.

The individual molecular moments in a system containing two or more molecules cannot be measured directly from experiment. Only the total moment of the system is an observable. Attempts have, nevertheless, been made to estimate the molecular dipole moment from measured macroscopic quantities for both ice [31] and liquid water [51]. A common method for constructing molecular multipoles in a condensed phase environment is via the induction model, where a multipole expansion of the molecular charge density is carried out and the multipoles are then modified using polarizabilities of the isolated molecule. The success of this method is not guaranteed since, for instance, the polarizability of a molecule in a cluster or condensed phase environment may be significantly different from that of an isolated molecule. A more rigorous way to estimate molecular multipoles is to use first principles calculations. Several previous studies have reported values for the molecular dipole moment of water in various environments [47, 52, 53, 54, 55, 56]. One drawback of this approach is that there is no *a priori* criterion that dictates how to partition either the wavefunction or the electronic charge density among the individual molecules. Several partitioning schemes have been proposed [57, 58, 59, 60, 61, 62, 63] based on various different criteria on either the electron density or the wave-

function of the system.

In this study, we report the molecular dipole moments, as well as the higher order multipole moments of water molecules in clusters and in ice I_h. We compare various methods for extracting the molecular multipole moments and discuss their convergence with cluster size to the ice I_h values. In Section 3.3 we outline the technical details of the first principles calculations. The various schemes used to partition the charge density are given in Section 3.4. Our results and additional discussion are presented in Section 3.5.

3.3 Computational Details

The electronic density for the water clusters up to and including the hexamer was calculated using the second order Moller-Plesset perturbation [64] theory (MP2) at the previously reported optimal cluster geometries [65, 46, 45, 66] obtained with the aug-cc-pVDZ basis set [67]. For the trimer through pentamer clusters, the global minima have quasi-planar, ring homodromic arrangements. For the hexamer, the ring structure corresponds to a local minimum with the cage structure being slightly lower in energy [68]. There exist three isomers within 1 kcal/mol from the global minimum [66].

We have also computed the electronic density in the water clusters and ice I_h using the plane wave based Density Functional Theory (DFT) method. The advantage of using this theoretical method is that it can be applied both to ice I_h, as well as the clusters. In these calculations the wave functions were expanded in a plane wave basis set with an energy cutoff of 70 Ry. A total of 16 molecules were included in the unit cell configuration for ice I_h. Only the Γ point was used in the Brillouin zone sampling. The pseudopotentials of Troullier and Martins [69] were used. As shown previously by Lee *et. al.* [70], the Local Density Approximation (LDA) produces a nearest-neighbor O-O sep-

aration for ice I_h that is 10% smaller than the experimental value of 2.75 Å while the Becke-Perdew (BP) gradient-corrected functional [71, 72] yields a value that is only 2% smaller than experiment. We used the Perdew-Wang (PW91) gradient-corrected functional [73, 74] and obtained an O-O distance of 2.7 Å at 0 K, which is just 2% smaller than the experimental value. During the DFT calculations, both the cluster and ice configurations were relaxed until the magnitude of the force on each of the ions dropped below 0.1 eV/Å.

The ice I_h configuration was constructed to satisfy the 'ice-rules' [75] and the proton ordering was chosen to be anti-ferroelectric, rather than random. This choice was made because of the small unit cell size.

The electron density was evaluated over a 3 dimensional rectangular grid of 150x150x150 evenly distributed points. The dimensions of the grid were chosen so the error in the integrated density is less than 0.03 electrons (0.1 electrons for the hexamer).

We calculated traceless multipoles with respect to the center of mass of each molecule by partitioning the electronic density and assigning it to individual molecules using the four schemes outlined below. We used the notation in the Appendix of Ref. [3] for the definition of the multipoles.

3.4 Partitioning Schemes

We applied four different algorithms for partitioning the electronic charge density obtained from the first principles (MP2 and DFT) calculations. The first three of the methods are spatial decompositions, *i.e.*, each point in space is assigned to only one molecule and there is no overlap of the electronic charge density assigned to two different molecules.

The four schemes used are as follows:

(i). The charge density is partitioned among the molecules according to the

Atoms In Molecules (AIM) method by Bader [63]. According to this method, the optimal partition into subsystems is achieved using a surface where the gradient of the charge density is parallel to the surface at all points, *i.e.*, the charge density is stationary in the direction normal to the surface

$$\vec{\nabla}\rho \cdot \hat{n} = 0 \tag{3.1}$$

where $\hat{n}$ is the normal to the surface and ρ is the charge density. The zero flux surfaces were calculated using an elastic sheet algorithm [76]. For the dimer, tetramer and pentamer we repeated the same calculation with the Atoms in Molecules (AIM) module of the Gaussian-94 suite of programs [77], which is based on an algorithm of Stefanov and Cioslowski [78]. The two methods agreed to within 1%. For the trimer and ring hexamer, the AIM calculation as implemented in Gaussian-94 did not converge while the elastic sheet method did. To test how sensitive the calculated molecular multipole moments are to slight changes in the partitioning of the charge density, we devised two other spatial partitioning schemes.

(ii). *Voronoy I* (V-I): The charge density is divided into Voronoy cells [79] using the center of charge on each molecule as the center of the Voronoy cell. The charge closest to the center of ionic charge of a given molecule is assigned to that particular molecule. The molecule is then described by only one point, namely the center of charge. Thus, no information regarding the geometry and orientation of the molecule is used in this scheme.

(iii). *Voronoy II* (V-II): The charge density is divided into Voronoy cells taking the position of individual atoms into account. If the hydrogen atoms are treated on an equal footing as the oxygen atoms, then the Voronoy construction divides the space near a hydrogen bond midway between the

hydrogen and oxygen atoms. The region associated with a hydrogen atom then cuts significantly into the charge density that is centered at oxygen atoms in neighboring molecules. We, therefore, have chosen to shift the Voronoy center associated with the hydrogen atoms along the O-H bonds towards the oxygen to make it lie closer to the minimum of the electron density. By inspection of contour plots of the charge density, we chose to displace the Voronoy centers for the hydrogen atoms by 60% from the hydrogen atom nucleus towards the oxygen nucleus in the molecule.

Figure 3.1 shows a contour plot of the charge density of the pentamer in the plane of the cluster as well as Voronoy I and Voronoy II dividing surfaces. In each of the three previously described spatial decomposition methods the volume associated with a water molecule is the volume corresponding to each of the two hydrogen atoms plus the volume corresponding to the oxygen atom.

(iv). *Molecular Proportion Partitioning Method* (MPP): The electronic charge density of the cluster at any point in space is partitioned among the individual molecules in proportion to the electronic charge density of the isolated molecules at that point.

The results for the multipoles obtained with the above four schemes are compared with the ones obtained from an induction model which is described in detail in Ref. [3]. Briefly, every water molecule is represented in the induction model as a point dipole, quadrupole, octopole and hexadecapole moment tensor placed at the center of mass of the molecule. The electric field at a molecule due to its neighbors induces both a dipole and a quadrupole moment. We used the experimentally measured values for the dipole and quadrupole moments, the MP2/aug-cc-pVQZ values for the octopole and hexadecapole moments, the experimentally measured molecular dipole polarizability, α_{ij} [39] and the results

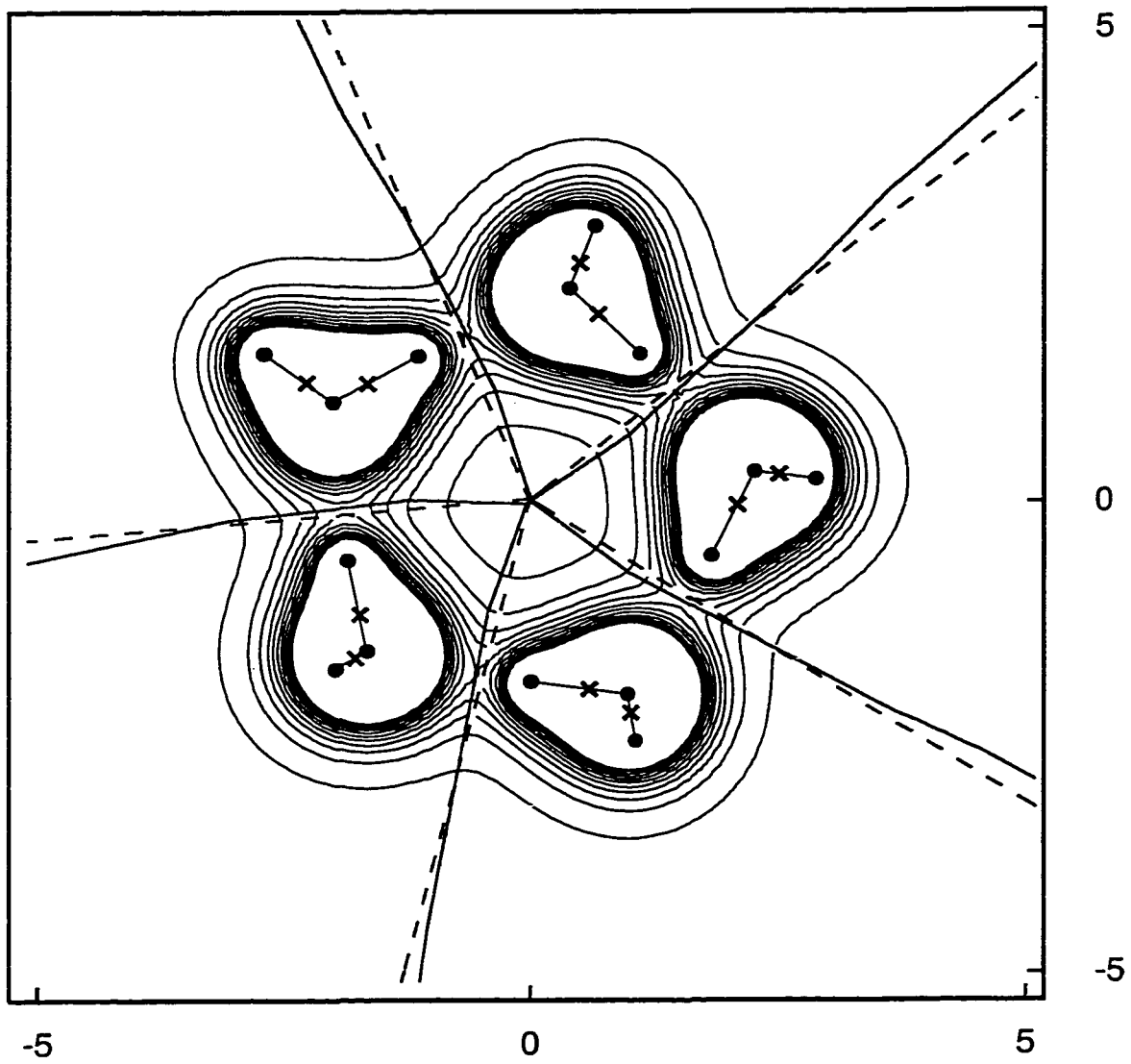

Figure 3.1: Contour plot of the charge density of the water pentamer in the plane of the cluster. The figure displays the charge density partitioned in the Voronoy I (dotted line) and Voronoy II (solid line) schemes (see text). In the Voronoy I scheme, the Voronoy cell is constructed around one center per molecule, placed at the center of ionic charge. In Voronoy II, the Voronoy cells are around three "atomic" centers per molecule one at the oxygen atom and the other two (shown with crosses) on the O-H bonds, at 40% of the displacement from the oxygen atom to the hydrogen nucleus. Although both surfaces are very similar, the latter passes closer through the minimum of the charge density between the molecules.

of previous *ab initio* calculations for the dipole-quadrupole, $A_{i,jk}$, quadrupole-quadrupole polarizability, $C_{ij,kl}$ [80] and the first hyperpolarizability, β_{ijk} [41]. The values of the moments and polarizabilities used here are the ones shown in Tables 5.1 and 2.2.

3.5 Results and Discussion

The variation of the average dipole moment with cluster size is shown in Figure 3.2. The different partition schemes of the charge density clearly lead to very different dipole moments. The average dipole moment of a molecule in ice I_h ranges from 2.3 D for the Voronoy II scheme to 3.1 D for the Voronoy I scheme. The AIM scheme gives intermediate results. Due to proton disorder, the dipole moment varies slightly from one molecule to another in a given ice I_h configuration (the standard deviation is 0.04 Debye). The dipole moments deduced from the MP2 and DFT calculations differ by less than 0.1 D for all the clusters. The results of the MPP scheme were also intermediate between the two Voronoy schemes, 2.05 D for the average molecular dipole moment in the dimer, and 2.19 D in the pentamer. The induction model gives larger dipole moments than any of the schemes used to partition the charge density obtained from first principles calculations for both the clusters and ice I_h.

Despite the large range of values obtained for the molecular dipole moment, it is, nevertheless, clear that the dipole moment of a water molecule in a hexamer does not converged to the dipole moment of a water molecule in ice I_h. Irrespective of which scheme is used, the molecular dipole moment in ice I_h is larger by up to 15% than the corresponding one in the hexamer. This result is to be expected from the fact that a molecule in the ice lattice has twice as many nearest neighbors as in the planar hexamer cluster and many more next nearest and distant neighbors, as well, which contribute to the polarization.

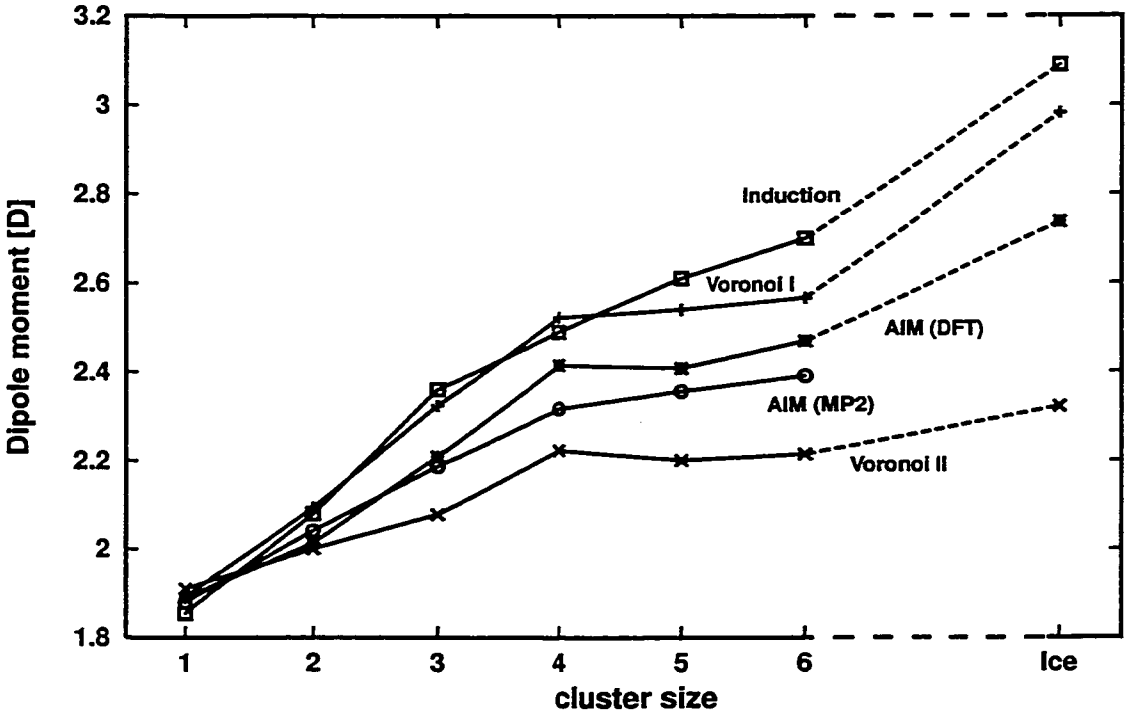

Figure 3.2: Magnitude of the molecular dipole moment as a function of the size of the cluster and for ice I_h. The calculations are based on the charge density obtained from MP2 calculations for the clusters, and DFT calculation of ice I_h as well as of the clusters. The difference between dipole moments obtained from the DFT calculation and the MP2 calculation is less than 0.1 D. Different ways of partitioning the charge density are compared: In AIM the charge density is partitioned with zero flux surfaces as proposed by Bader (∗). In the Voronoy I scheme the cells are constructed around the center of charge of each molecule (+). In Voronoy II the cells are constructed for each atom but the hydrogen atom centers are shifted by 60% of the distance towards the oxygen nucleus (see text and fig. 3.1) (×). The induction method includes polarizable dipole and quadrupole moments and fixed molecular octopoles, and hexadecapoles (□). Clearly, the value of the molecular dipole moment depends very strongly on how the electron density of the cluster is partitioned among the molecules. But, for all schemes, the value of the dipole moment in antiferroelectric ice is larger than for the clusters.

The calculated molecular quadrupole moments are shown in Figure 3.3. Here we have chosen to display the components of the tensor along the three principal axes. Clearly, there is not a smooth trend as the clusters increase in size. In ice I_h, the variation of the quadrupole moment due to proton disorder amounts to 0.02 Debye Å. It turns out to be very important to include the quadrupole moment, as well as octopole and hexadecapole moments, in order to reproduce the electric field around water clusters at a distance where additional water molecules could attach to the cluster.

It is important to realize that the only well-defined multipole moments are the multipole moments for the cluster as a whole. All the various schemes used here necessarily yield the same total dipole moment, for example, even though the molecular dipole moments differ greatly. A larger molecular dipole moment can be accommodated by changing the orientation of the molecular dipole moment vectors in such a way that larger cancellation occurs. The various schemes for decomposing the charge density yield, in fact, a rather similar rate of convergence for the multipole expansion of the electric field. This will be discussed in more detail in Chapter 4.

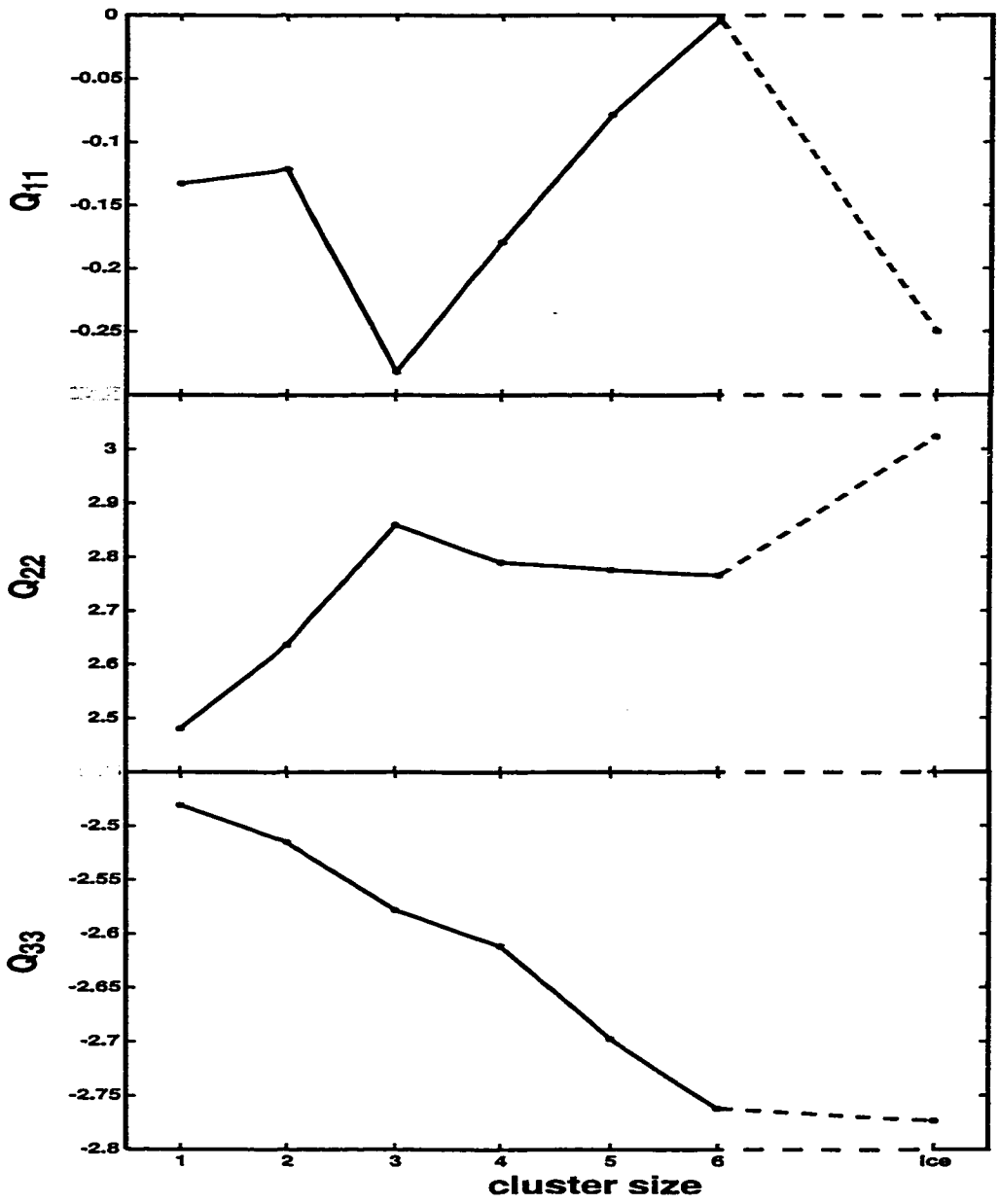

Figure 3.3: Quadrupole moment as a function of the cluster size. The graphs trace the average of each eigenvalue of the quadrupole tensor over the values for each fragment in the cluster. The quadrupole moments were calculated dividing the MP2 charge density with zero flux surfaces and integrating over the regions of each molecule. In a free molecule axis 1 is along the bisector of the molecule, axis 2 is perpendicular to 1 and in the plane of the molecule and axis 3 is an axis perpendicular to 1 and 2.

Chapter 4

ELECTRIC FIELDS IN ICE AND NEAR WATER CLUSTERS

4.1 Abstract

We have studied the electric field near water clusters and in ice I_h using first principles calculations. We used Moller-Plesset perturbation theory (MP2) for clusters up to and including the hexamer, and Density Functional Theory with a gradient dependent functional (DFT/PW91) for ice I_h, as well as for the clusters. The electric field obtained from the first principles calculations was used to test the predictions of an induction model based on single center multipole moments and polarizabilities of an isolated water molecule. We found that the fields obtained from the induction model agree well with the first principles results when the multipole expansion is carried out up to and including the hexadecapole moment and when the polarizable dipole and quadrupole moments are included. This implies that accurate empirical water interaction potential functions, transferable to various environments such as water clusters and ice surfaces, could be based on a single center multipole expansion carried out up to the hexadecapole. Since point charges are not included, the computationally intensive Ewald summations can be avoided. Molecular multipole moments were also extracted from the first principles charge density using zero flux dividing surfaces, as suggested by Bader. Although the values of the various molecular multipoles obtained with this method are quite different from the ones resulting from the induction model, the rate of convergence of the electric

field is, nevertheless, quite similar. This illustrates how ill-defined molecular multipole moments are in clusters and condensed phases.

4.2 Introduction

The interaction between water molecules, including hydrogen bonding, is believed to be largely electrostatic and is typically modeled simply by placing point charges on or near the O atom and on the H atoms in each water molecule. Such models are typically tailored to be consistent with various properties of liquid water, but may not accurately reproduce the electric fields in other environments, such as water clusters, ice, surfaces and interfaces. The more sophisticated point charge models also include polarizable point dipoles, which greatly improve their ability to reproduce diverse environments[81, 49, 50]. A frequently discussed quantity is the dipole moment of water molecules in various environments, such as clusters and condensed phases (see, for example, refs. [50, 28, 30, 31, 51, 52, 53, 54, 55, 56, 47, 48, 3]). The dipole moment of a water molecule in ice is estimated to be significantly larger than the dipole moment of an isolated water molecule [3].

A systematic approach to modeling the electric field around water molecules is the induction model, where a multipole expansion of the electron density is carried out [28, 27, 42, 37]. The effect of the external field on the multipoles is included via the molecular polarizability. The most straightforward approach is to expand the electron density about one center on each molecule, for example the center of mass. It is not clear, however, what order in the multipole expansion is required to accurately represent the electric field at distances relevant to molecular interactions, and whether polarizabilities of isolated molecules can be used for water molecules in condensed phases, such as ice. More sophisticated multipole expansions have been used by Stone and Buckingham and

coworkers [42, 37], where several multipole expansion centers are included on each molecule, which is known as the distributed multipoles approach. The expansion then typically includes point charge terms, even for neutral molecules such as water.

First principles calculations can nowadays be carried out at a level that is sufficient to accurately reproduce the interaction between water molecules. Such calculations can provide important information about the electric field and can be used to test various empirical or semi-empirical descriptions. The first principles calculations can also be used to extract molecular multipoles. Several first principles studies have reported values for the molecular dipole moment of water in various environments [52, 53, 54, 55, 56, 47]. It is, however, not clear how to partition the wavefunction or the electronic charge density among the individual molecules in a system of two or more molecules. Several schemes for achieving this have been proposed [59, 60, 57, 58, 61, 62, 63] invoking different criteria for assigning pieces of the electron density or the wavefunction to individual molecules. Nevertheless, different partition schemes can lead to widely different values for the multipole moments as we show in Chapter 3.

We report here on studies of the electric field in water clusters and ice I_h based on first principles calculations. We compare the electric field obtained from the first principles calculations with electric fields predicted by a simple induction model based on a multipole expansion around the center of mass of the molecules. This calculation establishes the order in the multipole expansion that is required to reproduce the *ab initio* electric field and tests whether the use of gas phase molecular polarizabilities is appropriate in order to model condensed phase environments. It has been previously shown that for clusters of diatomic molecules, such as HF and CO, it is sufficient to include up to quadrupole terms [82], but H_2O is likely to require higher multipoles. Self-

consistent field (SCF) calculations of polarizabilities of urea dimer and trimer have suggested that additivity of molecular polarizabilities yield a good approximation for small clusters [83]. Changes in the polarizability due to slight changes in the molecular geometry have also been found to be small [84, 85, 86]. These earlier studies support the notion that an induction model may indeed be a good approximation for describing molecular interactions. In this study, we carry out rigorous tests of this proposition for water clusters by investigating how accurately the induction model reproduces the electric field obtained from first principles calculations.

We have also used the results of first principles calculations to extract the molecular multipole moments and we compare them with values obtained from the induction model. In Section 4.3, we outline the technical details of the first principles calculations. For completeness, the induction model is described in Section 4.4. Our results are presented in Section 4.5 and are discussed further in Section 4.6.

4.3 First Principles Calculations

We have carried out calculations of water clusters and ice I_h using density functional theory (DFT) [87, 88]. Only the valence electrons are explicitly included in the calculations; the pseudopotentials of Troullier and Martins [69] were used. The wave functions were expanded in a plane wave basis set with an energy cutoff of 70 Ry. A total of 16 molecules were included in the ice I_h configuration. Only the Γ point was used in the Brillouin zone sampling. As was shown by Lee *et. al.* [70], the Local Density Approximation (LDA) gives a lattice constant for ice I_h that is 10% smaller than the experimental value, while gradient dependent functionals resulted in a much better agreement with the experimental value. We have used the PW91 gradient corrected functional

[73, 74] and obtained a nearest neighbor O-O separation of 2.7 Å at 0 K, which is just 2% smaller than the experimental value. Both the cluster and ice configurations were relaxed until the magnitude of the force on each of the ions dropped below 0.1 eV/Å.

The ice I_h configuration was constructed in order to satisfy the 'ice-rules' [89] and the proton ordering was chosen to be anti-ferroelectric, rather than random because of the small system size. In order to probe the electric field in a region that is relevant for intermolecular interactions, we removed one molecule from the ice configuration to create a vacancy. The configuration was then relaxed. The four molecules adjacent to the vacancy moved towards the vacancy site by 0.53 Å, 0.51 Å, 0.31 Å, and 0.15 Å, respectively. The charge density was then used to calculate the total electric field at various points in the vacancy region.

Calculations of the multipole moments of an isolated water molecule and of the field near water clusters were also carried out using second order Moller-Plesset perturbation theory (MP2), which were similar to previous MP2 calculations of water clusters [65, 46, 44, 45, 66]. The aug-cc-pVDZ basis set [67] was used. The MP2 multipole moments of an isolated water molecule were used in the induction model (see Section 4.4). The electric field at the water clusters obtained from the MP2 was very similar to that obtained from the DFT calculations.

4.4 The Induction Model

The same induction model presented in Section 2.3 was used to calculate the polarized multipoles.

The induction model uses information only from isolated water molecules. The polarizability of each molecule is taken into account by allowing the total

field at a water molecule to induce dipole and quadrupole moments, thereby taking into account, to some extent, the environment of the molecule. The i-th component of the induced dipole moment is given by [37]

$$\Delta \mathcal{P}_i = \alpha_{ij}\, E_j + \frac{1}{3}\, A_{i,jk}\, \frac{\partial E_j}{\partial r_k} + \frac{1}{2}\, \beta_{ijk}\, E_j\, E_k. \tag{4.1}$$

Here, E is the total electric field, α_{ij} is the molecular dipole polarizability, $A_{i,jk}$ the dipole-quadrupole polarizability, and β_{ijk} the first hyperpolarizability. (Note that the sum over the repeated indices is implicit).

The electric field also induces a quadrupole moment on each molecule [37]

$$\Delta \mathcal{Q}_{ij} = A_{k,ij}\, E_k + C_{ij,kl}\, \frac{\partial E_k}{\partial r_l} \tag{4.2}$$

where $C_{ij,kl}$ is the quadrupole-quadrupole polarizability.

Equations (4.1) and (4.2) are implicit equations of $\mathcal{P}_i$ and $\mathcal{Q}_{ij}$. A given molecule polarizes its neighbors and these polarized neighbors are the ones that induce the additional dipole and quadrupole. We adopted an iterative procedure to solve these non-linear equations.

There is no *a priori* guarantee that the induction model will accurately predict the electric field in and around configurations of water molecules. The molecular polarizability could, for example, change significantly in going from an isolated molecule to a water cluster and to ice. In the next section, we describe tests of the induction model where the predicted electric field is compared to the one obtained from first principles calculations.

4.5 Results

The dominant attractive interaction between water molecules is the electrostatic interaction. To compare the induction model with the first principles calculations, we computed the total electric field at points located in a vacancy

in the ice I_h lattice and around water clusters. We calculated the elctric potential, $U(\mathbf{r})$, and the electric field, $\mathbf{E}(\mathbf{r})$, in two distinct ways: The electrostatic potential and electric field were calculated from the DFT charge density as

$$U(\mathbf{r}) = \int_{\text{all space}} d^3r' \, \frac{\rho(\mathbf{r}')}{|\mathbf{r} - \mathbf{r}'|} \tag{4.3}$$

and,

$$\mathbf{E}(\mathbf{r}) = \int_{\text{all space}} d^3r' \, \frac{\rho(\mathbf{r}') \, (\mathbf{r} - \mathbf{r}')}{|\mathbf{r} - \mathbf{r}'|^3}. \tag{4.4}$$

We also calculated the same quantities from the molecular multipole description of the system (see equations (A.1) and (A.3) in Appendix A).

Figure 4.1 shows the magnitude of the electric field in a vacancy of an ice I_h crystal†. The field predicted by the induction model reproduces quite well the electric field calculated directly from the first principles DFT charge density, provided that the multipole expansion is carried out up to and including the hexadecapole. A total of 33 points were sampled inside the vacancy. The points were distributed along the line segments between the center of the vacancy towards the nearest molecules. The distance from each sampling point to the center of charge of the nearest molecule in the crystal is shown in Figure 4.2. (Note from Figure 4.1 that the field due to only the molecular dipoles is significantly smaller than the total field). Adding the quadrupole and octopole contributions increases the field significantly and actually overshoots the total field when the octopole is added. The hexadecapole contribution then reduces its magnitude and yields a very good agreement with the total field. These calculations show that an induction model including hexadecapoles could yield a good representation of the electrostatic interactions of water molecules for the intermolecular separations typical of condensed phases.

Table 4.1 shows the convergence of the electric field as a function of the

---

†All the electric fields are given in Debye per Å^3.
D/Å^3 = 1.44 10^{11} Volt meter^{-1} = 4.8 10^6 statvolt cm^{-1}

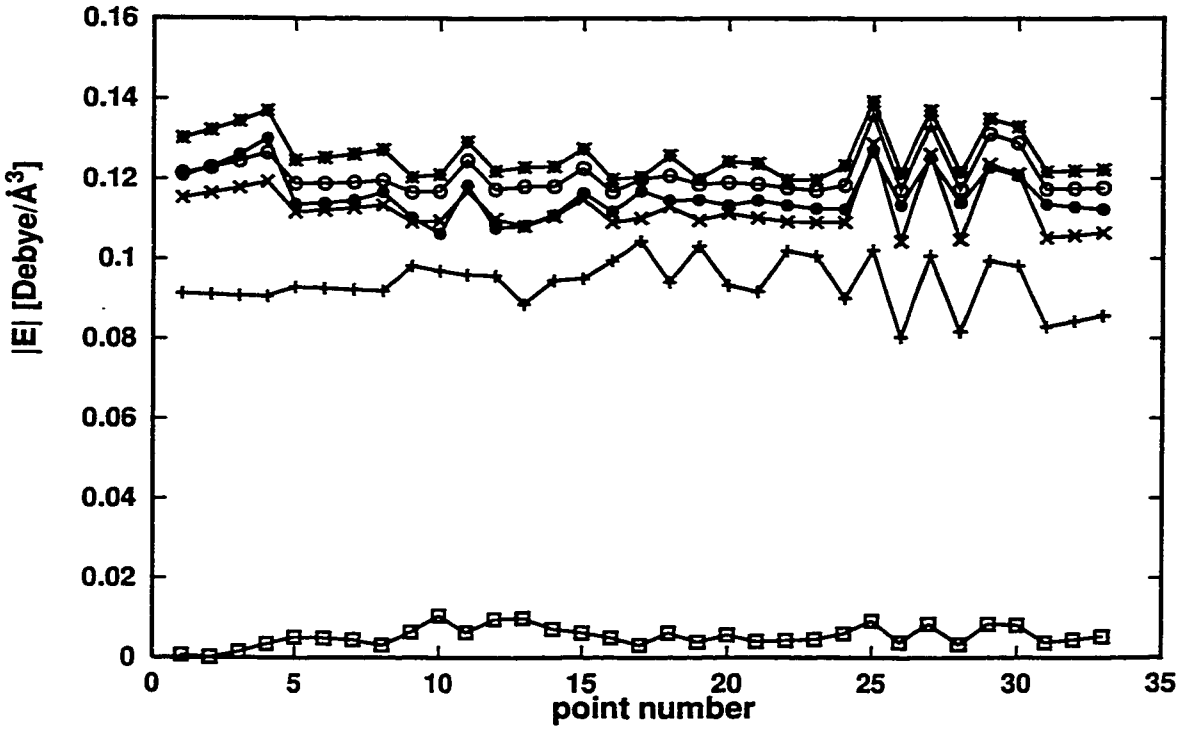

Figure 4.1: Magnitude of the electric field inside a vacancy in ice I_h calculated using the DFT charge density (•) and the induction model. While the dipole field (+) of the induction model is the largest component, it only accounts for 70 to 80% of the total field. For a better description of the electric field it is necessary to include quadrupole (×), octopole (∗) and hexadecapole contributions (○). The open squares show the difference between the difference between the DFT field and the miltipole field including up to hexadecapoles. The points are sorted according to increasing distance to the nearest center of charge which is given in Figure 4.2.

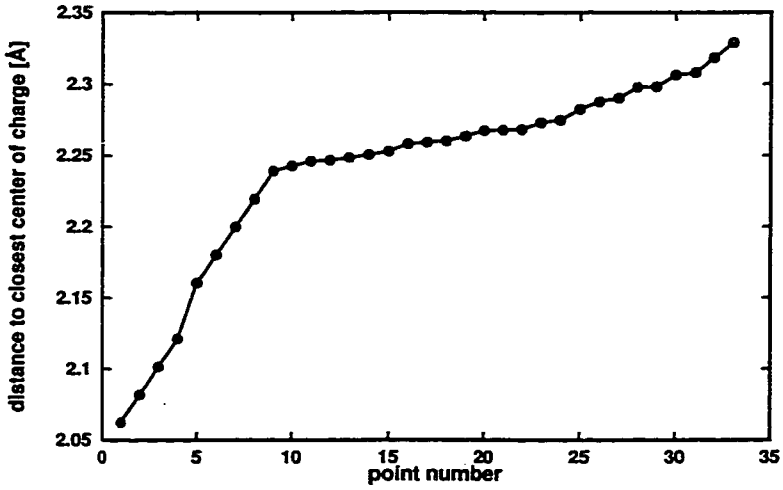

Figure 4.2: Distance from the various points inside the vacancy in ice at which the electric field is sampled (see Figures 4.1, 4.3 and 4.4) to the center of charge of the nearest water molecule in the ice lattice.

Table 4.1: Ratio of the magnitude of the electric field in a vacancy in ice calculated using the multipole expansion and the magnitude of the field calculated from the DFT charge density. The convergence of the multipole expansion can be seen as more terms are added to the expansion: $\mathcal{P}$ stands for dipole, $\mathcal{Q}$ for quadrupole, $\mathcal{O}$ for octopole and $\mathcal{H}$ for hexadecapole. The average over the various points inside the vacancy is given, as well as the standard deviation.

	AIM	Voronoy I	Voronoy II	Induction
$\mathcal{P}$	0.73±0.05	0.76±0.06	0.66±0.05	0.74±0.05
$\mathcal{P}$+$\mathcal{Q}$	0.88±0.03	0.94±0.03	0.82±0.02	0.92±0.03
$\mathcal{P}$+$\mathcal{Q}$+$\mathcal{O}$	1.10±0.03	1.17±0.03	1.04±0.02	1.04±0.02
$\mathcal{P}$+$\mathcal{Q}$+$\mathcal{O}$+$\mathcal{H}$	1.03±0.02	1.07±0.03	0.96±0.02	1.00±0.02

order of the multipole expansion. Each entry in the table is an average over the sampled points. The table gives the ratio of the miltipole field to the total field calculated from the DFT charge density. Even though the dipole field is the most important contributor to the total electric field, it is important to also include higher order multipoles, up to hexadecapole, because of the proximity to the neighboring water molecules.

The question naturally arises whether first principles calculations can be used to extract multipole moments that can be used in an induction model. The decomposition of the charge density into molecular fragments is, in fact, very arbitrary and many different decomposition methods have been proposed. We first used the Atoms in Molecules (AIM) method of Bader [63], where zero flux surfaces are used as dividing surfaces between the different molecules. The calculation was carried out using an elastic sheet method for finding the zero flux surfaces[76]. The resulting molecular dipole moments of water molecules in ice I_h are given in Table 4.2.

The AIM scheme produces significantly smaller dipole moments than the induction model. The field inside a vacancy in ice, calculated using the multipole moments of the AIM molecules, is shown in Figure 4.3. While this dipole field is smaller than the dipole field in the induction model, convergence to the full field is nearly reached when moments up to the hexadecapole are included. Significantly different values of the molecular multipoles can, therefore, be equally valid for practical purposes. To test how sensitive the first principles molecular moments are to the partitioning scheme, we also partitioned the calculated electron density using a Voronoy cell construction with a center placed at the center of mass of each molecule (Voronoy I scheme), as well as a Voronoy cell construction where a center is placed on each of the oxygen atoms and on each of the O-H bonds, located at a point 40% of the total distance from O to H (Voronoy II scheme), (see Chapter 3). By including three centers, the bound-

Table 4.2: Average molecular dipole moment of a water molecule in ice I_h calculated by various methods. The induction model includes polarizable dipole and quadrupole as well as fixed octopole and hexadecapole and uses exclusively parameters from an isolated water molecule. The AIM method of Bader divides the electronic charge density with zero flux surfaces. The Voronoy I scheme involves constructing Voronoy cells around the center of mass of each molecule. In the Voronoy II scheme three Voronoy centers are used for each molecule, one placed at the oxygen atom, and the other two placed on the H-O bonds, located at a point 40% of the total distance from O to H. The resulting values for the dipole moment are very different, even though the multipole expansion of the electric field converges at a rate very similar to the field obtained from the full electron density (see Figures 4.1, 4.3 and 4.4).

Method	$\mathcal{P}$ (Debye)
Induction	3.10
AIM	2.75
Voronoy I	2.97
Voronoy II	2.33

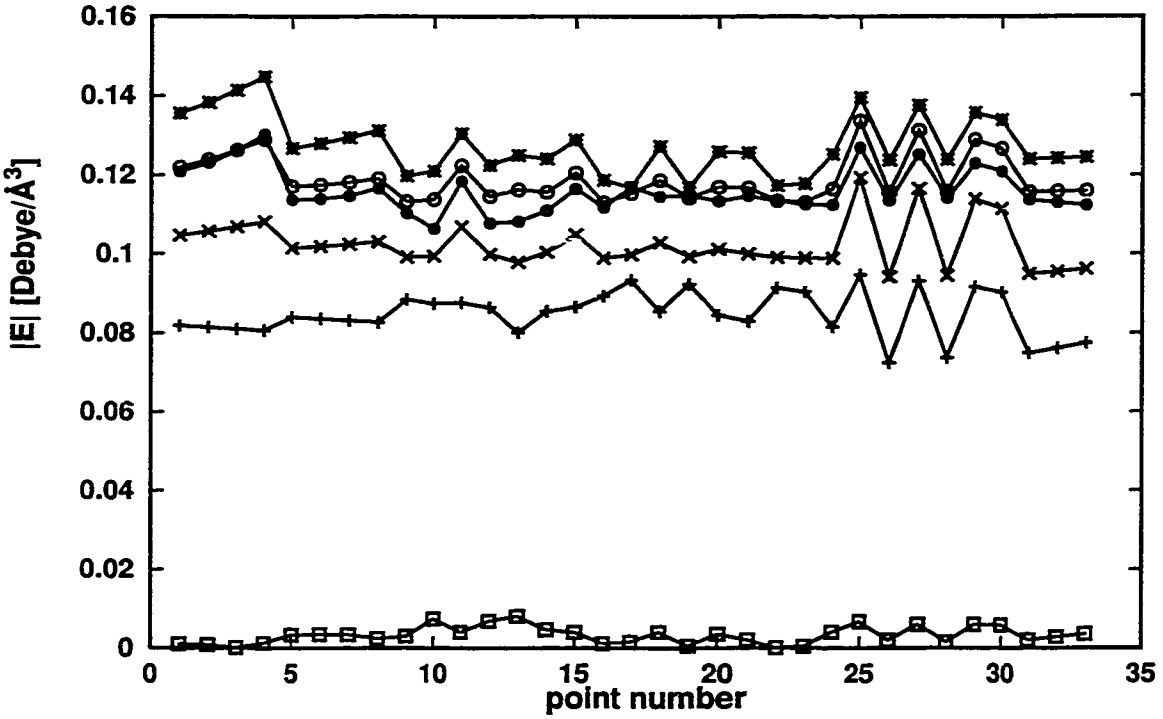

Figure 4.3: Magnitude of the electric field inside a vacancy in ice I_h calculated using multipoles obtained from the AIM decomposition of the DFT charge density and from the DFT charge density directly (•). While the dipole field is significantly smaller using the AIM dipoles rather than the induction model, the AIM multipole expansion converges at a rate similar to that of the induction model. Good agreement is obtained with the field deduced from the full DFT charge density at the hexadecapole. Various components of the AIM field are shown (the notation of the various components is the same as in Figure 4.1).

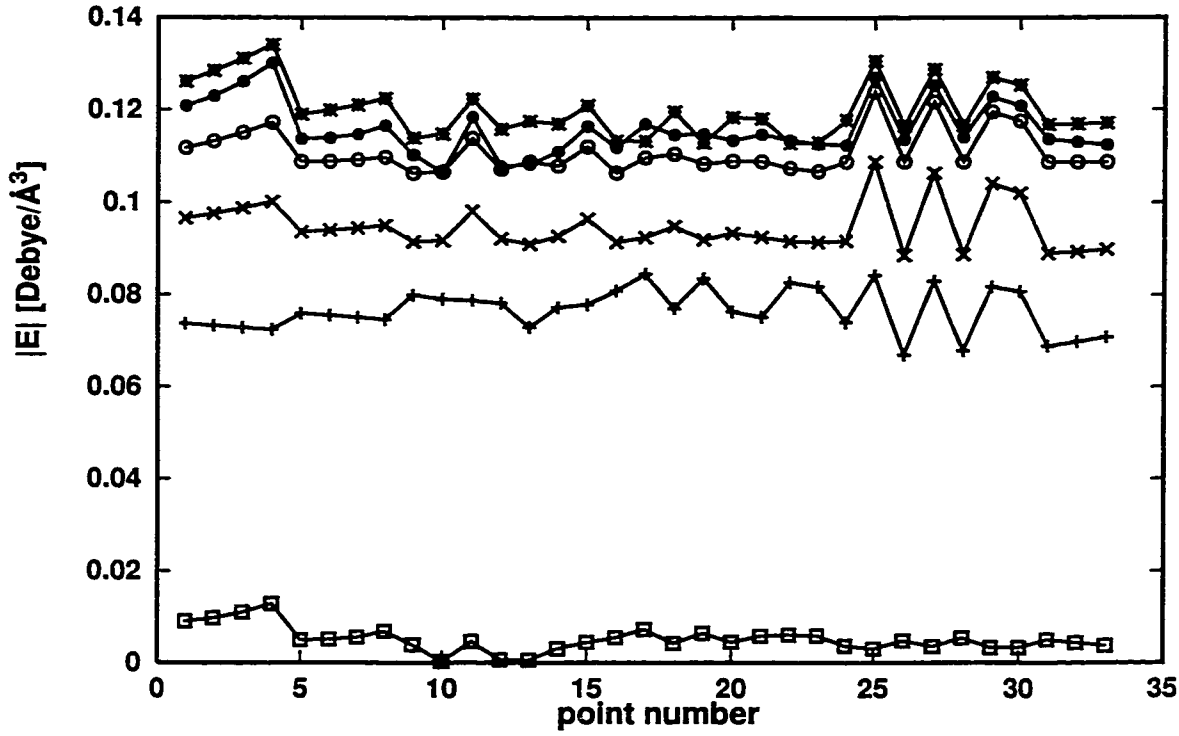

Figure 4.4: Magnitude of the electric field inside a vacancy in ice I_h calculated using multipoles obtained from the Voronoy II decomposition of the DFT charge density and from the DFT charge density directly (•). The Voronoy II multipole expansion converges at a similar rate as the induction model and the AIM multipole expansion. Good agreement is obtained with the field deduced from the full DFT charge density at the hexadecapole. Various components of the AIM field are shown (the notation of the various components is the same as in Figure 4.1)

aries of the Voronoy cells can be made to lie near the region of minimal electron density between the molecules. While these two Voronoy schemes give significantly different values for the molecular dipole moment (see Table 4.2), the rate of convergence to the electric field obtained from first principles is again quite similar, as can be seen in Figure 4.4. The convergence of the Voronoy I scheme is, however, slightly slower. The rate of convergence of the electric field using the various decomposition schemes for defining the molecular multipole

moments is so similar that it is difficult to say that one is distinctly better than another.

The same conclusions are reached from studies of the electric field around small water clusters. Figure 4.5 shows the electric field on a sphere of 4 Å radius around the water trimer cyclic minimum computed from the MP2 charge density (•) and by summing up the various contributions using the induction model (solid line). About 1177 points were uniformly sampled on the surface of the sphere starting at the north pole and moving down in circles of decreasing latitude towards the equator which contains the three oxygen atoms. Only the field on the northern hemisphere is shown (600 points). The zigzag pattern is the result of the sampling of points on circles of increasing radius from zero to 4 Å. This is a stringent test because this is as close as an additional molecule can get to the cyclic trimer in the plane of the cluster to form bound states that are connected with hydrogen bonds. From Figure 4.5, one can see that the agreement is fairly good and that it gets better farther away from the cluster. Closer to the center of the cluster, the electric charge density becomes significant. Since the multipole expansion of a charge density converges only when the field point is outside the charge distribution, the two calculations start to disagree significantly at distances shorter than 4 Å.

4.6 Discussion

The success of the induction model, which only requires data that can be obtained from first principles calculations of the isolated water molecule, is very encouraging. This suggests that an accurate description of the electrostatic interaction of water molecules can be achieved without having to carry out the computationally demanding first principles calculations for large systems. We are currently developing an empirical potential function based on the multi-

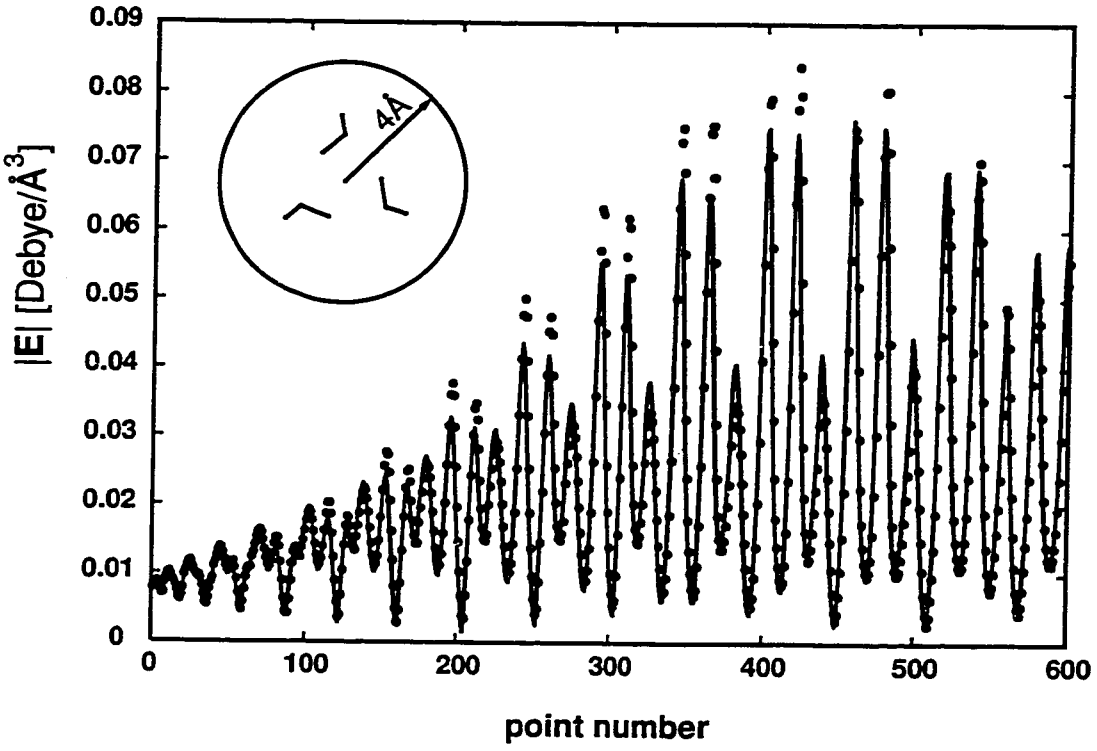

Figure 4.5: Magnitude of the electric field around a water trimer calculated from the MP2 charge density (•) and the field predicted by the induction model (solid line). The field was calculated on a sphere of 4Å radius. Multipoles up to hexadecapole are included. The field on the upper hemisphere is shown (the lower hemisphere gave similar results). The horizontal axis is the sample point number. 1177 points were sampled uniformly over the surface of the sphere starting at the upper pole and moving down to the equator which contains the three oxygen atoms.

pole expansion including the hexadecapole and both dipole and quadrupole polarizabilities. Interaction potentials for water molecules based on distributed multipole expansions have been previously introduced [57, 58], but they are very costly to evaluate and thus have so far only been applied to small clusters. By including only multipoles with respect to the center of mass, as seems to be adequate from Figures 4.1 and 4.5, the evaluation of the electric field can be done quite efficiently. Since no point charges are included, it is not necessary to use Ewald summation. In fact, it is sufficient to include only the field from neighbors within an 8 Å radius [3]. The multipole description of the electrostatic interactions is much more accurate than the various point charge models which are frequently used in computer simulations of water. Since the Ewald sum can be avoided, the evaluation of the multipole expansion does not involve significantly larger computational effort than the simple point charge models. The electric field generated by a typical point charge model does not agree well with the one obtained from first principles calculations. For example, the field calculated using the TIP4P point charge model [21], an empirical potential which has been very successful in reproducting properties of bulk liquid water, gives an electric field that is about 20% larger than the one obtained from first principles in the ice vacancy. Our results suggest that an accurate interaction potential for water that is transferable to various environments, such as small clusters and ice surfaces, can be constructed using a single center multipole expansion with a computational effort that is quite similar to that of simple pair potentials which are only applicable to bulk water and ice.

Finally, the large range of values of the molecular dipole moments in ice, obtained by using different reasonable schemes for extracting molecular dipole moments from first principles charge densities, illustrates how poorly defined the molecular multipole moments are. The fact that the different schemes give very similar rate of convergence to the full electric field means that there is not

a clear compelling reason in this case to choose one over the other.

Chapter 5

POTENTIAL OF INTERACTION H_2O-H_2O

The development of a potential energy function describing the interaction of molecules relies on an educated "guess" for the functional form of the potential energy of the system as a function of the molecular coordinates. This potential energy function and its derivatives should reproduce the known properties of the system under study. A "guess" for the functional form of the potential energy relies on physical intuition and knowledge of various properties of the system. In the case of the water molecule interactions, the electric and dielectric properties appear to dominate the attractive interaction. While there also must be some covalent effects, the magnitude of the covalent contribution seems to be negligible compared with the electrostatic one. This will be justified later when a detailed analysis of the dimer interaction is discussed. We, therefore, decompose the potential energy of a system of water molecules in the following way:

- Electrostatic energy, $U^{(es)}$, described in Section 5.2
- Effects due to the polarization of the molecules, $U^{(pol)}$, described in Section 5.4
- Dispersion energy, $U^{(disp)}$, described in Sections 5.3 and 5.6
- Repulsion due to the overlapping electronic clouds, $U^{(rep)}$, described in Section 5.7.

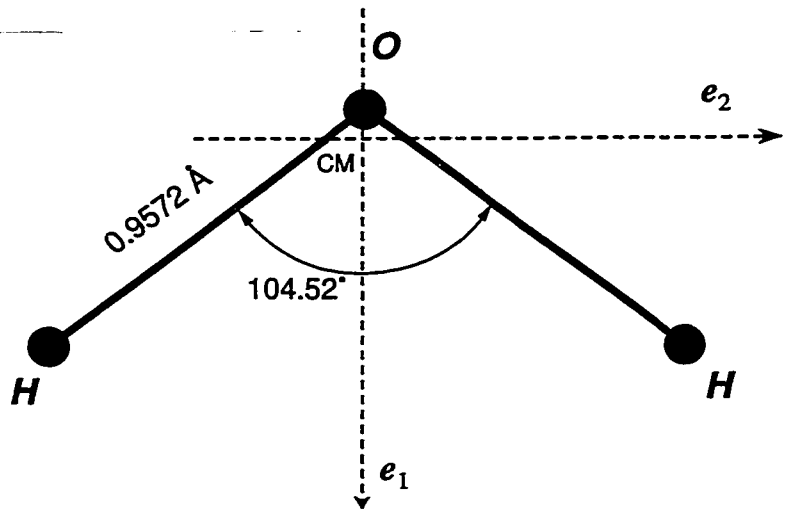

Figure 5.1: Geometry of the water molecule. The molecule is considered a rigid body with the angle and O-H distances shown in the figure

5.1 Molecular Geometry

Each water molecule is treated as a rigid body composed of three particles, a particle representing the oxygen atom (mass of 15.9994 amu) and two particles representing the hydrogen atoms (each with a mass of 1.00794 amu). The hydrogen atoms are located 0.9572 Å away from the oxygen atom and the $\widehat{\mathrm{HOH}}$ angle is taken to be 104.52°. With these definitions, the principal axes of the inertia tensor are: $\hat{e}_1$ along the bisector of the molecule (see Figure 5.1), axis $\hat{e}_2$ perpendicular to $\hat{e}_1$ and on the plane of the molecule, and axis $\hat{e}_3 = \hat{e}_1 \times \hat{e}_2$. The center of mass of the molecule is at $0.0656\,\hat{e}_1$ and the principal moments of inertia respect to the center of mass are $I_1 = 1.155$, $I_2 = 0.615$ and $I_3 = 1.770$ amu Å^2.

5.2 *Electrostatic Energy*

The electrostatic interaction between the molecules is described in terms of a multipole expansion. The molecules were modeled as a collection of multipole moments located at their center of mass. It was found that in order to reach convergence in the multipole expansion of the electric field, at distances that are typical molecular distances in ice, the multipole expansion has to be carried out up to and including the hexadecapole moment. Therefore, the electrostatic potential at point $\mathbf{r}_i$, generated by a molecule located at point $\mathbf{r}_j$, is

$$U = \frac{\mathcal{P}_i\, r_i}{r^3} + \frac{\mathcal{Q}_{ij}\, r_i\, r_j}{r^5} + \frac{\mathcal{O}_{ijk}\, r_i\, r_j\, r_k}{r^7} + \frac{\mathcal{H}_{ijkl}\, r_i\, r_j\, r_k\, r_l}{r^9} \tag{5.1}$$

where $\mathbf{r} = \mathbf{r}_i - \mathbf{r}_j$ and $\mathcal{P}$, $\mathcal{Q}$, $\mathcal{O}$, $\mathcal{H}$ are the dipole, quadrupole, octopole and hexadecapole moments, respectively.

In the rest of this section, the calculation of the forces and torques on a molecule is given in detail. Explicit expressions for the first and second derivatives of the potential function are given in the Appendix A.

The total force on a molecule due to the field of the rest of the crystal can be split into the force on each multipole term

$$\mathbf{F} = \mathbf{F}_d + \mathbf{F}_q + \mathbf{F}_o + \mathbf{F}_h \tag{5.2}$$

where $\mathbf{F}_d$ is the force on the dipole given by

$$F_d(\mathbf{r})_n = -U_{;in}\mathcal{P}_i. \tag{5.3}$$

Here we adopted the notation that subindices after the semi-colon (;) indicate partial derivatives, therefore,

$$U_{;in} = \frac{\partial^2 U(\mathbf{r})}{\partial r_i \partial r_n} = -\frac{\partial E_i(\mathbf{r})}{\partial r_n} = -E_{i;n} \tag{5.4}$$

where $\mathbf{E}(\mathbf{r})$ is the electric field at $\mathbf{r}$. The force on the quadrupole moments, $\mathbf{F}_q$, is given by

$$F_q(\mathbf{r})_n = -U_{;ijn}\mathcal{Q}_{ij}. \tag{5.5}$$

$\mathbf{F}_o$ is the force on the octopole

$$F_o(\mathbf{r})_n = -U_{;ijkn}\mathcal{O}_{ijk}. \tag{5.6}$$

$\mathbf{F}_h$ is the force on the hexadecapole

$$F_h(\mathbf{r})_n = -U_{;ijkln}\mathcal{H}_{ijkl} \tag{5.7}$$

where

$$U_{;ijkln} = \frac{\partial^5 U(\mathbf{r})}{\partial r_i \partial r_j \partial r_k \partial r_l \partial r_n}. \tag{5.8}$$

All these partial derivatives were evaluated analytically.

The total torque on the molecules can be evaluated from the same partial derivatives of the electrostatic potential. We decompose the total torque into the torques on each multipole term,

$$\tau(\mathbf{r}) = \tau_d + \tau_o + \tau_q + \tau_h \tag{5.9}$$

where the torque on the dipole moment is

$$\tau_d(\mathbf{r})_i = -(\mathcal{P}_j U_{;k} - \mathcal{P}_k U_{;j}). \tag{5.10}$$

The three components of the torque are obtained upon cyclic permutations of the indices (i, j, k). The torque on the quadrupole moment is

$$\tau_q(\mathbf{r})_i = -2(\mathcal{Q}_{jq}U_{;kq} - \mathcal{Q}_{kq}U_{;jq}) \tag{5.11}$$

where the repeated index q is to be summed from 1 to 3. The three components are obtained from cyclic permutations. The torque on the octopole moment is calculated as

$$\tau_o(\mathbf{r})_i = -3(\mathcal{O}_{jqr}U_{;kqr} - \mathcal{O}_{kqr}U_{;jqr}) \tag{5.12}$$

and the torque on the hexadecapole moment is calculated as

$$\tau_h(\mathbf{r})_i = -4(\mathcal{H}_{jqrs}U_{;kqrs} - \mathcal{H}_{kqrs}U_{;jqrs}) \tag{5.13}$$

where the repeated indices q, r and s are summed from 1 to 3.

5.3 Induction Effects

The induction effect on the dipole and quadrupole moments were taken into account up to second order. The electric field at a molecule due to its neighbors then induces both a dipole moment and a quadrupole moment in the molecule. The i-th component of the induced dipole moment is given by [37]

$$\Delta\mathcal{P}_i = -\alpha_{ij}\, U_{;j} - \frac{1}{3}\, A_{i,jk}\, U_{;jk} \tag{5.14}$$

where α is the dipole-dipole polarization tensor and A is the dipole-quadrupole polarizability.

The induced quadrupole moment of the molecule is [37]:

$$\Delta\mathcal{Q}_{ij} = -A_{k,ij}\, U_{;k} - C_{ij,kl}\, U_{;kl} \tag{5.15}$$

where C is the quadrupole-quadrupole polarizability.

Equations (5.14) and (5.15) are implicit equations of $\mathcal{P}_i$ and $\mathcal{Q}_{ij}$. A given molecule polarizes its neighbors and these neighbors in turn induce an extra dipole and quadrupole on the first molecule. Even though these equations represent a linear system that could be solved by matrix inversion, the dimensionality of the problem makes this approach inappropriate. We took a more efficient approach by using an iterative procedure. We start with the multipole moments of an isolated molecule and calculate the induction contribution. Then, we repeat the calculation with the induced multipoles until convergence is achieved.

The electric field was switched off at short distances using a switching function of the form

$$f_{\mathrm{sf}}(r) = \left[1 - \mathrm{e}^{-a\,r} \sum_{k=0}^{n} \frac{(-a\,r)^k}{k!}\right]^{1/2} \tag{5.16}$$

where $n = 6$ and the parameter $a = 4.4\ \text{Å}^{-1}$ is the inverse of the decay length of the charge density of the water monomer.

5.4 Polarization Energy

The polarization of the molecules results in a decrease of the energy. Indeed, the polarization of the molecules can be found by minimizing the total electrostatic energy with respect to the induced multipoles

$$\frac{\partial(U^{(\mathrm{es})} + U^{(\mathrm{pol})})}{\partial \Delta \mathcal{P}_j^{(i)}} = 0 \tag{5.17}$$

and

$$\frac{\partial(U^{(\mathrm{es})} + U^{(\mathrm{pol})})}{\partial \Delta \mathcal{Q}_j^{(i)}} = 0. \tag{5.18}$$

The energy due to the polarization of the molecules is given by [37]

$$U^{(\mathrm{pol})} = U_{dd} + U_{dq} + U_{qq} \tag{5.19}$$

where U_{dd} is the energy due to the dipole-dipole polarization, U_{dq} is the dipole-quadrupole polarization energy and U_{qq} is the quadrupole-quadrupole polarization energy.

The dipole-dipole polarization energy is given by

$$U_{dd} = \frac{1}{2}\alpha_{ij}\, U_{;i}\, U_{;j} \tag{5.20}$$

where α is the dipole-dipole polarizability tensor. The dipole-quadrupole polarization energy is given by

$$U_{dq} = -\frac{1}{3}A_{i,jk}\, U_{;i}\, U_{;jk} \tag{5.21}$$

where A is the dipole-quadrupole polarizability, and the quadrupole-quadrupole polarizability is

$$U_{qq} = -\frac{1}{6}C_{ij,kl}\, U_{;ij}\, U_{;kl} \tag{5.22}$$

where C is the quadrupole-quadrupole polarizability.

5.5 Multipoles and Polarizabilities

For the electrical properties of the water molecules, experimental values of the polarizabilities and multipole moments were used where available. In other cases, available *ab initio* calculated values were used.

5.5.1 Multipoles

Experimental values were available for dipole [29] and quadrupole moments [1]. For the octopole and hexadecapole moments, we used the values computed at the MP2/aug-cc-pVQZ level of theory, listed in Table 5.1. The agreement of the dipole and quadrupole moments at the MP2/aug-cc-pVQZ level of theory with the experimental ones justifies the use of the higher moments (octopole and hexadecapole) computed at this level of theory.

5.5.2 Polarizabilities

We made use of the experimentally measured molecular dipole polarizability, α_{ij} [39], but used results of previous *ab initio* calculations for the values of the dipole-quadrupole, A and quadrupole-quadrupole polarizability, C [80]. The values of the polarizabilities are those already given in Table 2.2.

5.6 Dispersion Energy

The dispersion interaction arises because the charge distribution of the molecules are constrantly fluctuating [37]. The motion of the electrons in two molecules become correlated, in such a way that lower-energy configurations are favoured and higher-energy ones disfavoured. The average effect is a decreace of the energy, and since the correlation effect becomes stronger as the molecules come together, the result is an attraction. We included the first three terms of

Table 5.1: Multipole moments of a water molecule used in the self-consistent induction calculations and comparison with values used in previous calculations. The moments are computed using the definitions given in Appendix B. The origin of the coordinate system is located at the center of mass of the molecule. The experimental values for the quadrupole moment are from reference [1].

		Exp	MP2	
Dipole	$\mathcal{P}_1$	-1.855	-1.86	$\times 10^{-18}$ e.s.u. cm
Quadrupole	$\mathcal{Q}_{11}$	-0.13	-0.1328	$\times 10^{-26}$ e.s.u. cm^2
	$\mathcal{Q}_{22}$	2.63	2.6135	
	$\mathcal{Q}_{33}$	-2.50	-2.4807	
Octopole	$\mathcal{O}_{111}$		1.3565	$\times 10^{-34}$ e.s.u. cm^3
	$\mathcal{O}_{122}$		-2.3288	
	$\mathcal{O}_{133}$		0.9723	
hexadecapole	$\mathcal{H}_{1111}$		-1.3637	$\times 10^{-42}$ e.s.u. cm^4
	$\mathcal{H}_{1122}$		1.6324	
	$\mathcal{H}_{1133}$		-0.2687	
	$\mathcal{H}_{2222}$		-0.3575	
	$\mathcal{H}_{2233}$		-1.2749	
	$\mathcal{H}_{3333}$		1.5436	

the dispersion interaction:

$$U^{(\mathrm{disp})} = -\frac{C_6}{r^6}\, g_6(r) - \frac{C_8}{r^8}\, g_8(r) - \frac{C_{10}}{r^{10}}\, g_{10}(r). \tag{5.23}$$

For the coefficients of the dispersion interaction we used the values recommended by Margofiash [90]: $C_6 = 27.751$ eV Å^6, $C_8 = 191.035$ eV Å^8, $C_{10} = 1566.902$ eV Å^{10}. At short distances the dispersion is switched off by the function $g_n(r)$ developed by Tang and Toennies [91]:

$$g_n(r) = 1 - \mathrm{e}^{-a\,r} \sum_{k=0}^{n} \frac{(-a\,r)^k}{k!} \tag{5.24}$$

The parameter a is the decay length of the electron charge density of an isolated molecule. The value $a = 4.4$ Å^{-1} was determined from the *ab initio*-calculated charge density.

5.7 Repulsive Core Energy

The term representing the repulsive interaction, due to the overlap of the electronic clouds, was obtained by fitting the difference between the results of the MP2 *ab initio* calculations of a water dimer at various distances and the sum of the electrostatic and dispersion interactions described above. The following functional form was used for the repulsive interaction:

$$U_I = A^{(\mathrm{rep})} \sum_{i=1}^{N} \sum_{j \neq i}^{N} r_{ij}^{b}\, \mathrm{e}^{-c\,r_{ij}} \tag{5.25}$$

Here, r is the vector separation between the oxygen atoms of the two molecules. The dimer energy curve was fitted using non-linear χ^2 minimization for 2.4 Å$\leq r \leq$ 10 Å, which yielded $A_{\mathrm{rep}} = 49710.86$ eV Å$^{(-b)}$, $b = 0.485$ and $c = 4.623$Å^{-1}.

To the repulsive interaction U_I we added a density-dependent term, a physical interpretation of which is given in Section 6.3. This extra term has the

same functional form as U_I, except that A_{rep} depends on the local density of water molecules and the exponential factor has a slower decay:

$$U_{II} = \sum_{i=1}^{N} B(\rho_i) \sum_{j \neq i} r_{ij}^{b} \, \mathrm{e}^{-c r_{ij}/1.325}. \tag{5.26}$$

The function $B^{(\text{rep})}(\rho)$ was adjusted to the properties of water clusters of up to six molecules and also the properties of ice $\mathrm{I_h}$ crystal:

$$B^{(\text{rep})}(\rho) = \begin{cases} 0 & \text{for } \rho \leq 1600 \\ \sum_{n=0}^{5} a_n \, \rho^n & \text{for } 1600 < \rho < 8000 \\ 0.012 & \text{for } 8000 \leq \rho \end{cases} \tag{5.27}$$

where $a_0 = 5.660\,10^{-3}$, $a_1 = -9.785\,10^{-6}$, $a_2 = 6.075\,10^{-9}$, $a_3 = -1.681\,10^{-12}$, $a_4 = 2.197\,10^{-16}$, $a_4 = -1.048\,10^{-20}$.

The local density was defined as a sum of exponential weights over the neighboring molecules as

$$\rho_i = \sum_{j \neq i}^{N} C \, \mathrm{e}^{-r_{ij}/d} \, r_{ij}^{-3} \tag{5.28}$$

where $C = 2.5\ 10^5 \text{Å}^3$ is an arbitrary scaling constant and $d = 1.5\text{Å}$.

Thus, the total repulsive energy for a system of N molecules takes the form

$$U^{(\text{rep})} = \frac{1}{2} A^{(\text{rep})} \sum_{i=1}^{N} \sum_{j \neq i}^{N} r^{b} \, \mathrm{e}^{-cr} + \frac{1}{2} \sum_{i=1}^{N} B^{(\text{rep})}(\rho) \sum_{j \neq i}^{N} r^{b} \, \mathrm{e}^{-cr/1.325}. \tag{5.29}$$

Since the expression for the force is quite complicated due to the density dependent term, we give explicit expressions for $\nabla U^{(\text{rep})}$.

$$\mathbf{F}_k^{(\text{rep})}(r) = -\frac{\partial U^{(\text{rep})}}{\partial \mathbf{r}_k} \tag{5.30}$$

The right hand side of the above equation is the gradient of equation (5.29)

$$\begin{aligned}\frac{\partial U^{(\mathrm{rep})}}{\partial \mathbf{r}_k} &= A^{(\mathrm{rep})} \sum_{i\neq k}^{N} \left(-c - \frac{1}{r}\right) r^b \, \mathrm{e}^{-cr} \, \hat{\mathbf{r}}_{ki} \\ &\quad \frac{1}{2}\sum_{i\neq k}^{N}[B(\rho_k) + B(\rho_i)] \left(-\frac{c}{1.325} - \frac{1}{r}\right) r^b \, \mathrm{e}^{-cr/1.325} \, \hat{\mathbf{r}}_{ki} \\ &\quad + \frac{1}{2}\sum_{i=1}^{N} \frac{\mathrm{d}B(\rho_i)}{\mathrm{d}\rho} \frac{\partial \rho_i}{\partial \mathbf{r}_k} \, \hat{\mathbf{r}}_{ki} \sum_{j\neq i}^{N} r^b \, \mathrm{e}^{-cr/1.325} \end{aligned} \tag{5.31}$$

where $\hat{\mathbf{r}}_{ki}$ is the unit vector from oxygen i to oxygen atom k. The gradient of the density function is given by

$$\frac{\partial \rho_i}{\partial \mathbf{r}_k} = \begin{cases} C \sum_{j\neq k}^{N} \left(-\frac{3}{r_{ki}} - \frac{1}{d}\right) \mathrm{e}^{-r_{kj}/d} \, r_{kj}^{-3} & \text{if } k = i \\ C \left(-\frac{3}{r_{ki}} - \frac{1}{d}\right) \mathrm{e}^{-r_{ki}/d} \, r_{ki}^{-3} & \text{if } k \neq i \end{cases} \tag{5.32}$$

5.8 Effect of the Switching Function

In order to make the interaction potential of finite range, the total potential energy was multiplied by the following switching function [92]

$$f_{\mathrm{sf}}(\mathbf{r}) = \begin{cases} 1 & \text{for } x \leq 0 \\ 1 + x^3(-6\,a^2 + 15\,x - 10) & \text{for } 0 < x < 1 \\ 0 & \text{for } 1 \leq x \end{cases}$$

where $x = (r - r_{\mathrm{low}})/(r_{\mathrm{high}} - r_{\mathrm{low}})$, $r_{\mathrm{low}} = 9$ Å and $r_{\mathrm{high}} = 11$ Å.

The effect of the switching function is that the results of simulations are independent of the size of the simulation box. Two aspects are important in chosing the switching function. First, the cut-off radius has to be large enough so that the interactions are not affected significantly. We chose a cut-off distance of 11 Å. This choice was based on our calculation of the induced molecular dipole moment as function of the cut-off, which indicated that the dipole moments are already converged to the long range limit at 11 Å (see section 2.4).

It is important to let the switching function act over a large enough interval. If the switching is too abrupt, the derivatives of the switching function in the intermediate region can introduce spurious forces that result in an extra "kick" on the particles. A switching region of 2 Å gave a smooth enough interaction with no appreciable extra "kick".

Chapter 6

FITTING OF THE H_2O-H_2O POTENTIAL FUNCTION

Most of the parameters in the potential function described in the previous chapter are known either from experimental measurements or *ab initio* calculations. This includes the parameters for the multipole moments and polarizabilities of the molecules in $U^{(es)}$ (see Section 5.2) and $U^{(pol)}$ (see Sections 5.3 and the dispersion interaction.

However, there are a few unknown parameters that have to be determined by fitting, *i.e.*, the values of the parameters are adjusted so as to reproduce known properties of the system under consideration. These unknown parameters are in the repulsive interaction, as well as in the short range switching function for the electrostatic field. We used results of MP2 and DFT *ab initio* calculations on water clusters and ice, as well as experimental measurements of the cohesive energy and lattice constant of ice to determine the free parameters.

6.1 Switching Function for Electrostatic Interaction at Short Distances

Since the multipole expansion only applies to far fields and uniform polarizabilities, adjustments need to be made in the functional form in order to reproduce the electric field at short distances.

In order to address this issue and to test the quality of the multipole expansion, we studied the electric field inside of a vacancy in ice. The field calculated from the full charge distribution, obtained from *ab initio* DFT calculations, was

compared with the results of the multipole expansion. While the agreement was very good for distances greater than 4 Å, a switching function had to be applied to the electric field in order to reproduce the *ab initio* calculations at short range.

Again, we used a Tang-Toennies type function

$$f_{\rm sf}(r) = \left[1 - {\rm e}^{-a\,r} \sum_{k=0}^{n} \frac{(-a\,r)^k}{k!}\right]^{1/2} \tag{6.1}$$

where $n = 6$. The parameter a was varied in order to reproduce as best as possible the electric field inside of the ice vacancy. The optimal value was found to be a=4.4 Å^{-1}. Figure 6.1 shows the electric field calculated from the DFT charge density, compared to the electric field from the semiempirical potential. The convergence as function of the multipole expansion is also shown. The '+' is the electric field due to dipoles, '×' is the expansion up to quadrupoles, '∗' for multiple expansion up to octopoles and 'o' includes hexadecapole moments. The electric field from the DFT charge density is represented using '•'.

6.2 Fitting of the Water Dimer

To determine the repulsive interaction, a pairwise contribution was first extracted from MP2/aug-cc-pVTZ calculations on the water dimer as a function of the distance between the molecules. For a fixed value of the distance between the two oxygen atoms, the orientational degrees of freedom, as well as the internal coordinates of the water molecules, where allowed to relax to the minimum energy configuration (see Figure 6.2).

The repulsive term in the potential energy was fitted to the difference between the *ab initio* curve and the electrostatic, induction and dispersion interactions. In Figure 6.2 we see the *ab initio* potential energy curve, as well as the electrostatic plus dispersion energies. The difference between these two curves

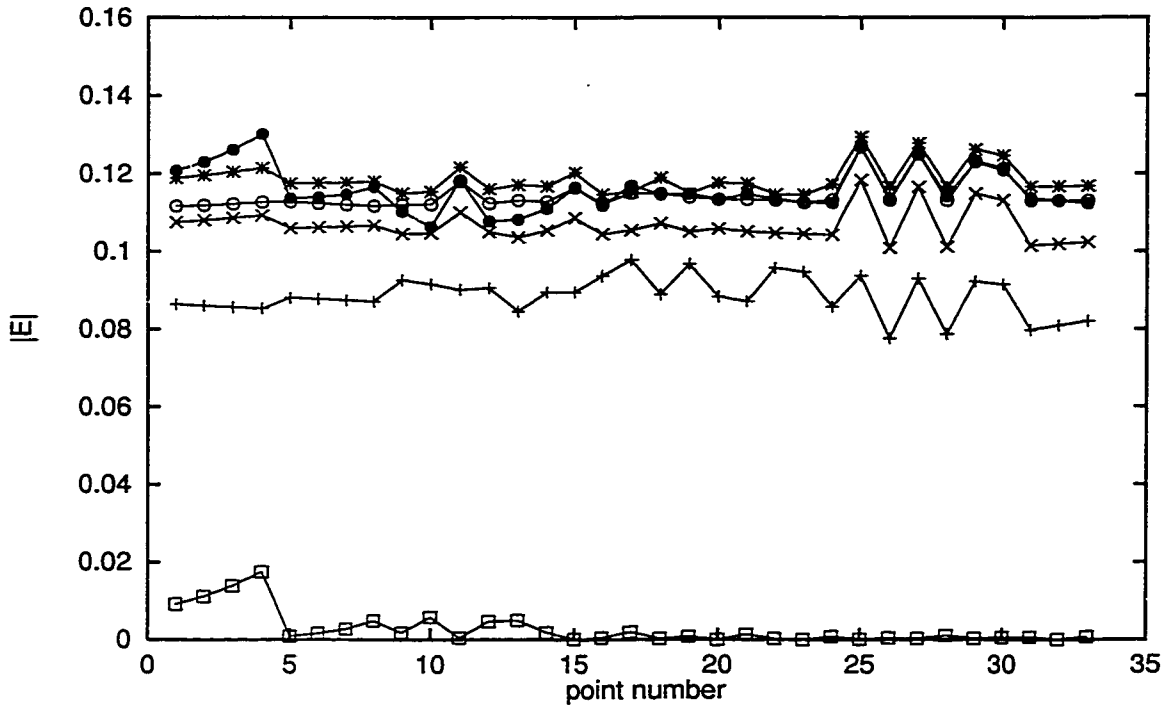

Figure 6.1: Electric field inside of a vacancy in ice I_h. The filled circles '•' are the field from DFT and the empty circles, 'o' represent the field from the multipole expansion up to hexadecapole moments. The cumulative field due to dipole, '+', quadrupole, '×' and octopole moments, '∗' are also shown. The difference between the DFT electric field and the field up to hexadecapole moments is indicated with '□'.

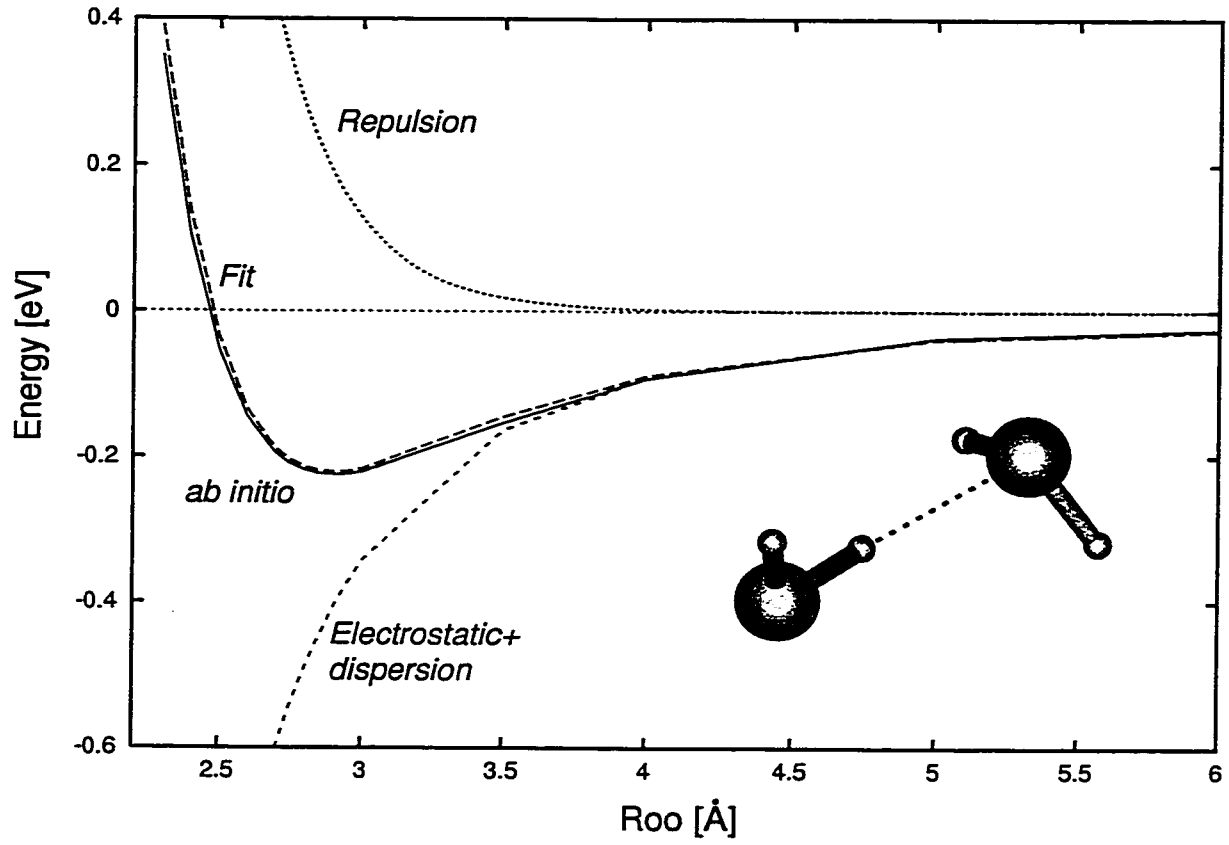

Figure 6.2: Potential energy of a water dimer as a function of the oxygen-oxygen separation. The total energy from *ab initio* calculations, as well as the semi-empirical terms $U^{(\mathrm{es})} + U^{(\mathrm{ind})} + U^{(\mathrm{disp})}$ are shown (labeled "*Electrostatic+dispersion*"). The difference (labeled "*overlap repulsion*") corresponds to the repulsion due to overlapping electronic clouds.

Table 6.1: Parameters of the overlapping interaction energy obtained after fitting the dimer potential energy curve

A	47798.9 eV $Å^{(-b)}$
b	0.485
c	4.623 $Å^{-1}$

is also shown labeled "overlap repulsion".

The functional form of the pairwise repulsion was chosen to be

$$U = A \sum_{i=1}^{N} \sum_{j \neq i}^{N} r_{ij}^{b} \, e^{-c r_{ij}} \tag{6.2}$$

and the parameters A, b and c varied to minimize the difference between the two curves in a least squares sense at 35 points along the curve. The parameters obtained from the fit are presented in Table 6.1. Since the fit is not perfect, the location of the minimum is shifted from 2.907 Å to 2.89 Å. In order to reproduce the *ab initio* oxygen-oxygen separation, we increased the fitted parameter A by 2%. That gives the right separation but it underestimates the binding energy by 0.005 eV, which is within the accuracy of the *ab initio* calculation.

6.3 Density Dependent Interaction

In the same manner as the electrostatic interaction has a many-body dependence, we expect the repulsion energy term to have many-body effects. This additional term increases the repulsion between molecules as the density of neighboring molecules increases. Effectively, this is a way to take into account the increase in the volume of the molecules as they become polarized.

This density dependent term also includes the change in internal energy of each molecule due to the zero point motion for the nuclei. Using the vibrational

frequencies from ref. [46] we observe that the internal frequencies change depending on the environment of the molecule. The zero point motion energy per molecule is: 0.584eV for the water monomer, 0.581eV for the water dimer, 0.567eV for the water trimer and 0.559eV for molecules in a water tetramer. In going from the monomer to the tetramer, the zero point energy decreased of each molecule by 0.025eV, 10% of the binding energy of a water dimer.

As the density increases the zero point energy decreases while the opposite trend is observed for the effect due to the overlapping electron clouds. We found that the net effect has to be repulsive.

The density-dependent term was taken to decay less rapidly than the pairwise part presented in Section 6.2. This is consistent with the slower decay length of excited state orbitals, which are mixed in as the molecules polarizes.

We adopted the same functional form as for the pairwise part, but now the pre-exponential factor increases with the density

$$U = \sum_{i=1}^{N} B(\rho_i) \sum_{j \neq i} r_{ij}^{b} \, \mathrm{e}^{-c r_{ij}/1.325}. \tag{6.3}$$

The density of molecules at a given molecule was defined as the sum over exponential weight functions, located at each one of the neighboring molecules

$$\rho_i = \sum_{j \neq i}^{N} C \, \mathrm{e}^{-r_{ij}/d} \, r_{ij}^{-3}. \tag{6.4}$$

The parameter d was taken to be 1.5Å, so as not to introduce a large distinction between clusters, surface molecules and bulk molecules. This decay length yields a density that has a main contribution from the nearest-neighbor molecules (at distances between 2.7 and 2.9 Å), while at the next-nearest-neighbor distances (located at about 4.4Å) the density is 8% of the value at the first neighbors and the rest of the molecules have a minor contribution. The value of $B(\rho)$ was chosen to be zero for the dimer density. We found that a value of

$B = 0.012$ yields a cohesive energy of 0.58 eV in ice I_h, in agreement with the experimental value of 0.58 eV at zero kelvin [35]. The same value of B yields a density corresponding to an oxygen-oxygen distance of 2.75 Å, in agreement with the experimental value of 2.75 Å.

A third value of the $B(\rho)$ function was obtained from the hexamer. Even though there are several possible structures for a water hexamer, we fitted the ring structure, as all the molecules are in the same environment and, therefore, they all have the same density.

Using these three values of $B(\rho)$, we fitted a polynomial that passes through all three points and has zero derivative at the end points:

$$B^{(\mathrm{rep})}(\rho) = \begin{cases} 0 & \text{for } \rho \leq 1600 \\ \sum_{n=0}^{5} a_n \rho^n & \text{for } 1600 < \rho < 8000 \\ 0.012 & \text{for } 8000 \leq \rho \end{cases} \tag{6.5}$$

where $a_0 = 5.660\,10^{-3}$, $a_1 = -9.785\,10^{-6}$, $a_2 = 6.075\,10^{-9}$, $a_3 = -1.681\,10^{-12}$, $a_4 = 2.197\,10^{-16}$, $a_4 = -1.048\,10^{-20}$. For densities smaller than that of the molecules in the dimer, the function B was assumed to be zero, leaving only the fitted dimer interaction potential (equation (6.2)). For molecules with higher densities than ice I_h, the function was also assumed to be constant. Figure 6.3 shows the interpolated function B as a function of the density, where the density values range from the density of the molecules in the water dimer to the density of a water molecule in ice I_h. We have indicated the densities for molecules in the different ring clusters; for the trimer and pentamer we have indicated an average over the densities of the molecules.

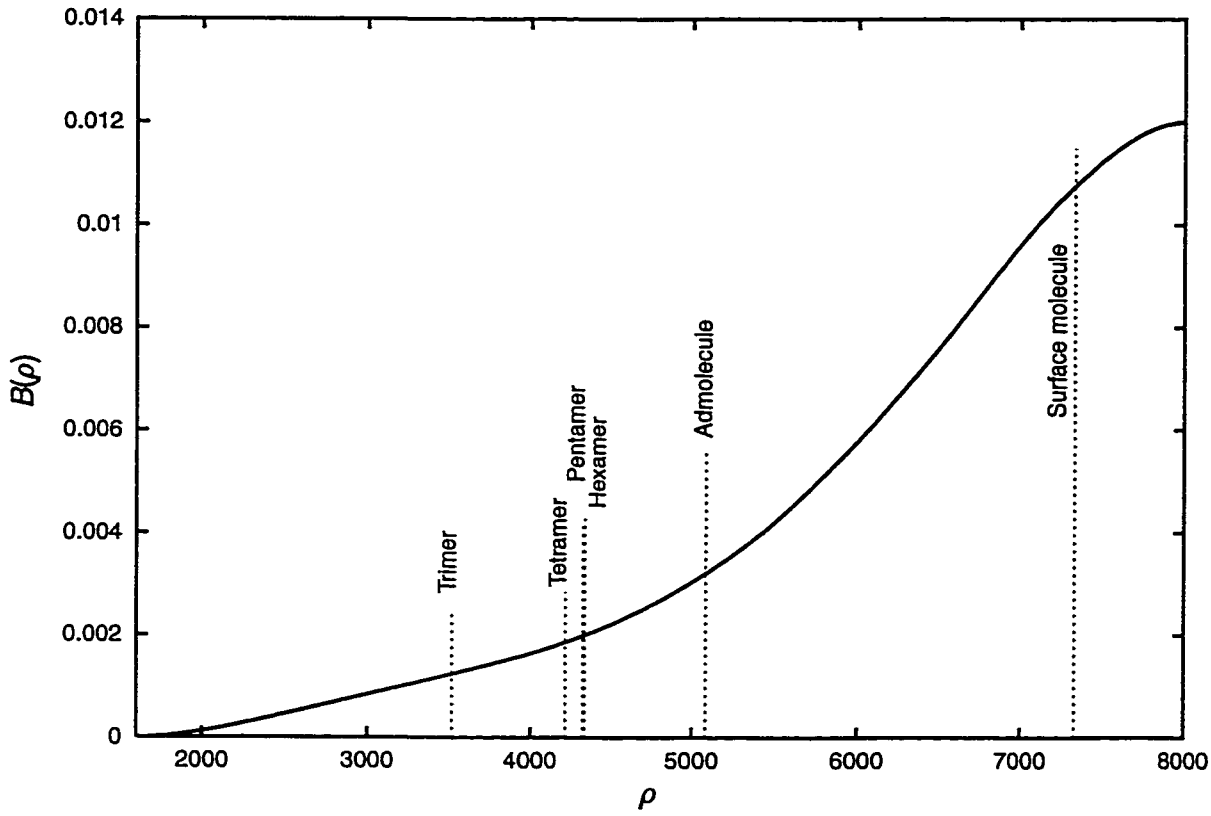

Figure 6.3: Function to interpolate the pre-exponential factor in the overlap repulsion, energy as a function of the local density of the molecule. Dotted lines indicate the density of the molecules in the different types of ring clusters and, in a typical molecule on the surface of ice I_h.

Chapter 7

TESTING THE NEW POTENTIAL

The potential developed in the previous chapters was tested against the properties of water clusters. Many-body interactions and minimum-energy configurations for the new potential were compared with the values calculated using first principles calculations.

7.1 Geometries

The minimum-energy configurations for clusters of two to six molecules were calculated using the new semi-empirical potential and *ab initio* MP2/aug-cc-pVDZ.

7.1.1 The Water dimer

We tested the accuracy of our potential of a water dimer. Figure 7.1 shows the

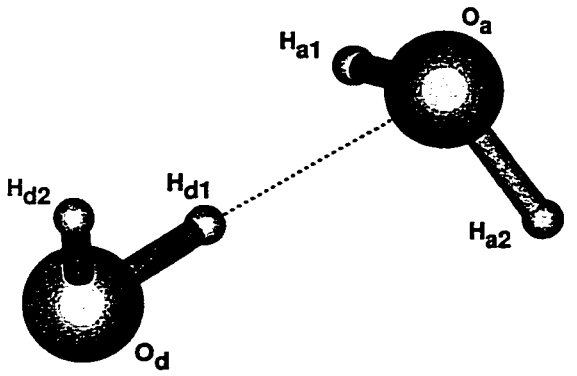

Figure 7.1: Water dimer in its optimal configuration

Table 7.1: Comparison among trimer geometries for MP2 (*ab initio* calculations), BJX (our newly developed potential), and the standard potentials, TIP4P and RWK2. The subscripts 'a' and 'd' label the acceptor and donor molecules respectively.

Property	MP2	BJX	TIP4P	RWK2
E/bond [eV]	0.224	0.219	0.270	0.278
R(O-O)	2.907	2.907	2.748	2.734
$R(O_d\text{-}H_{d1})$	0.960	0.957	0.957	0.957
$R(O_d\text{-}H_{d2})$	0.969	0.957	0.957	0.979
$R(O_a\text{-}H_{a1})$	0.962	0.957	0.957	0.961
$R(O_a\text{-}H_{a2})$	0.962	0.957	0.957	0.961
$H_{d1}\text{-}O_d\text{-}H_{d2}$	104.485	104.520	104.520	104.140
$H_{a1}\text{-}O_a\text{-}H_{a2}$	104.531	104.520	104.520	104.771
$O_d\text{-}H_{d1}\text{-}O_a$	171.574	174.364	178.169	175.989

water dimer at the minimum-energy configuration. The figure also defines the labeling of atoms. Since we fitted the potential to reproduce the energy curve of the water dimer, we necessarily obtained good agreement with the *ab initio* values of energy and distances. Table 7.1 gives a detailed comparison of the two calculations. We also include geometries and energies of two potentials used in the literature, TIP4P [21] and RWK2 [20, 93]. Since we used a rigid model to describe the water molecules, there is necessarily some discrepancy due to changes in the internal degrees of freedom in the *ab initio* calculations. The molecules in TIP4P are rigid and non-polarizable, while RWK2 is a flexible model which allows for the polarization of the molecules.

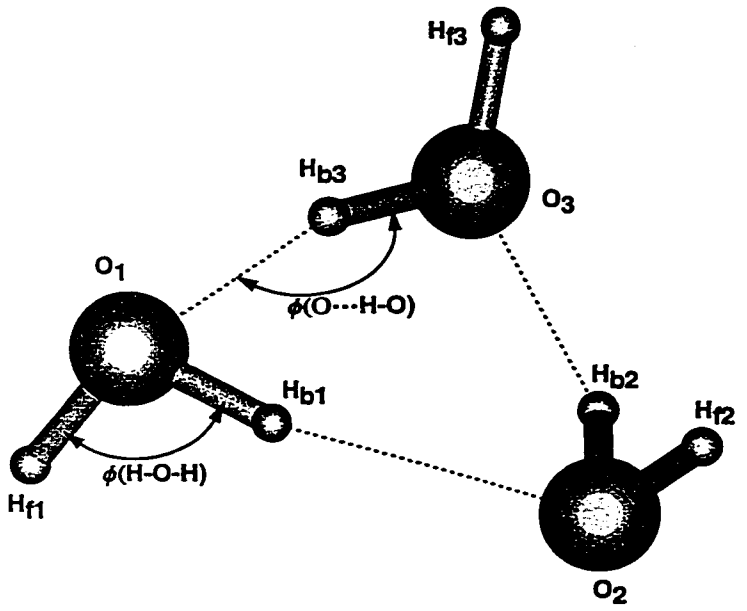

Figure 7.2: Water trimer in its optimal configuration

7.1.2 The Water Trimer

Comparing the water trimer is important because it is the smallest cluster that can show the effect of the three-body energy (this will be discussed in Section 7.2). The optimized configuration is shown in Figure 7.2, along with the labels of the atoms and angles. In Table 7.2, we compare again our prediction with *ab initio* results and commonly used empirical potentials. Since the molecules are not equivalent to each other, the O-H and O-O bond distances are not all the same. To make the comparison easier, we averaged these numbers in Table 7.2. The oxygen-oxygen distances in the *ab initio* calculations have a dispersion of 0.001Å, our potential has a dispersion of 0.008Å, TIP4P has a dispersion of 0.007Å and RWK2 has a dispersion of 0.05Å. The RWK2 potential seems to reproduce the geometry of the cluster very well only when the average value of the O-O distances is compared, however, the length of the individual bonds is, in fact, not well reproduced. The same averaging problem appears in

Table 7.2: Comparison among trimer geometries for MP2 (*ab initio* calculations), BJX (our newly developed potential), and the standard potentials, TIP4P and RWK2. Averages are being quoted for the bond distances and angles but not for the dihedral angles.

Property	MP2	BJX	TIP4P	RWK2
E/bond [eV]	0.226	0.242	0.242	0.230
R(O-O)	2.799	2.813	2.761	2.795
R(O-H_f)	0.965	0.957	0.957	0.959
R(O-H_b)	0.978	0.957	0.957	0.979
R(O$\cdots$H)	1.907	1.900	1.859	1.884
ϕ(H_f-O-H_b)	105.193	104.520	104.520	104.508
ϕ(O$\cdots$-H_b-O	150.256	158.832	156.020	154.048
H_{b1}-O_1-O_2-O_3	118.385	108.699	127.859	107.981
H_{b2}-O_2-O_3-O_1	196.030	174.176	169.394	178.878
H_{b3}-O_3-O_1-O_2	180.560	173.169	177.969	183.628
H_{f1}-O_1-O_2-O_3	118.385	108.699	127.859	107.981
H_{f2}-O_2-O_3-O_1	237.288	250.775	221.458	249.050
H_{f3}-O_3-O_1-O_2	230.874	247.185	208.924	234.933

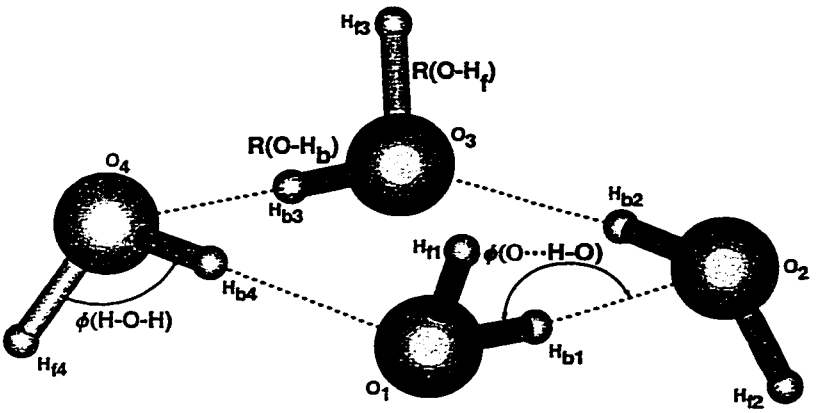

Figure 7.3: Water tetramer in its optimal configuration

R(O···H). The actual distances from the *ab initio* results are 1.901, 1.901 and 1.920Å, from TIP4P they are 1.845, 1.856 and 1.876 Å, from RWK2 they are 1.830, 1.827 and 1.994 Åand from our new potential (New Pot.) they are 1.890, 1.895 and 1.914 Å. Again, the dispersion is bigger in TIP4P, overestimating the longer bond and underestimating the shorter ones.

7.1.3 The Water Tetramer

The optimal configuration of the water tetramer with S_4 symmetry is shown in Figure 7.3, along with definitions of internal coordinates. Due to the high symmetry of this cluster, all the molecules are equivalent, making the description much simpler.

Table 7.3 shows a comparison of the geometries from *ab initio* at the MP2 level of theory, with the optimal geometries of our potential, as well as TIP4P and RWK2. The error in the oxygen separation is less than 4% and the energy per hydrogen bond is overestimated by 4%.

Table 7.3: Comparison among the S_4 tetramer geometries for *ab initio* MP2 calculation our newly developed potential (BJX) and the optimal geometries calculated with TIP4P and RWK2.

Property	MP2	BJX	TIP4P	RWK2
E/bond [eV]	0.310	0.322	0.302	0.315
R(O-O)	2.743	2.733	2.723	2.710
R(O-H_b)	0.965	0.957	0.957	0.960
R(O-H_f)	0.985	0.957	0.957	0.988
R(O_1-H_{b2})	1.773	1.780	1.774	1.730
ϕ(H_f-O-H_b)	105.008	104.520	104.520	104.490
ϕ(O$\cdots$H-O)	167.643	173.982	170.595	170.721
H_f-O_1-O_2-O_3	0.823	358.208	10.377	0.413
H_b-O_1-O_2-O_3	247.615	250.963	254.169	250.777

7.1.4 The Water Pentamer

The symmetry of the water pentamer, as with the trimer, is broken by the hydrogen atoms. The optimal configuration is shown in Figure 7.4, together with the labeling of the atoms and angles. None of the molecules are equivalent to each other and, therefore, the oxygen-oxygen and hydrogen-hydrogen bond distances are all different. For the sake of simplifying the comparison of the structures predicted by different potentials and *ab initio*, we give average values for these quantities Table 7.4. Quite close agreement is obtained for the distances between oxygen atoms. The structure derived from *ab initio* calculations has oxygen separations of (2.725, 2.722, 2.723, 2.726, 2.734) Å, our new potential predicts (2.726, 2.725, 2.724, 2.721, 2.738) Å, TIP4P predicts (2.721, 2.718, 2.718, 2.718, 2.722, 2.729) Å and RWK2 predicts (2.710, 2.708, 2.709,

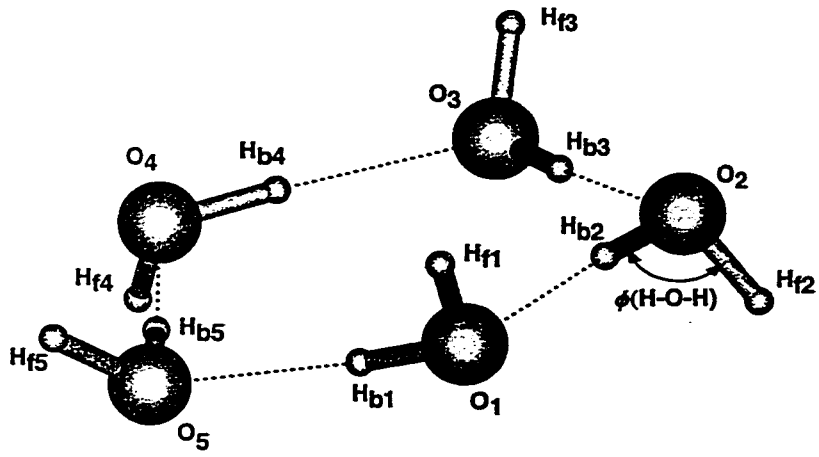

Figure 7.4: Water pentamer in its optimal configuration

Table 7.4: Comparison among the pentamer geometries for *ab initio* MP2 calculation our newly developed potential (BJX), TIP4P and RWK2.

Property	MP2	BJX	TIP4P	RWK2
E/bond [eV]	0.330	0.332	0.315	0.327
R(O-O)	2.726	2.727	2.721	2.710
R(O-H_f)	0.986	0.957	0.957	0.987
R(O-H_b)	0.964	0.957	0.957	0.959
R(O_1-H_{b2})	3.139	3.078	3.096	3.112
ϕ(H-O-H)	104.855	104.520	104.520	104.406
ϕ(O$\cdots$H-O)	175.611	176.624	176.578	176.974
O_1-O_2-O_3-O_4	344.539	2.815	330.346	339.915
O_1-O_2-O_3-O_5	350.523	355.220	347.712	349.110
O_2-O_3-O_4-H_{b4}	359.338	357.764	357.713	0.543
O_2-O_3-O_4-H_{f4}	121.185	110.347	126.644	122.169

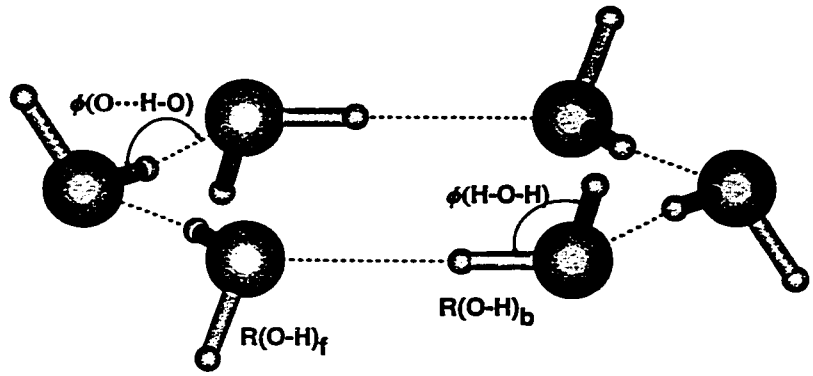

Figure 7.5: Water hexamer in its optimal configuration

2.709, 2.709, 2.715) Å. Our new potential (New Pot.) predicts the R(O-O) distance with an error 0.04% and the energy per hydrogen bond is overestimated by 0.6%.

7.1.5 The Water Hexamer

The nearly planar hexamer cluster was instrumental in going from the clusters to ice when the many-body repulsion was fitted. The configuration with S_6 symmetry is shown in Figure 7.5. Because of the high symmetry of this cluster, all the molecules have the same geometry, making the comparison simpler. Angles and bond distances are displayed in Table 7.5 The agreement is satisfactory, even though we only used the oxygen-oxygen separation during the fit. The R(O-O) distance predicted by our new potential is 0.5% longer than the *ab initio* results as a force due to the interpolating function (see Section 6.3) was neglected during the fit (a constant value of the B coefficient had been assumed). The binding energy is overestimated by 0.9%.

Table 7.5: Comparison among the hexamer geometry for *ab initio* MP2 calculation our newly developed (BJX) potential and two standard potentials. The subindices 'f' and 'b' label the free and the bonding hydrogen atom, respectively.

Property	MP2	BJX	TIP4P	RWK2
E/bond [eV]	0.330	0.333	0.320	0.330
R(O-O)	2.716	2.729	2.721	2.712
R(O-H_f)	0.986	0.957	0.957	0.986
R(O-H_b)	0.964	0.957	0.957	0.959
R(O$\cdots$$H_b$)	1.730	1.776	1.765	1.725
ϕ(H-O-H)	104.739	104.520	104.520	104.315
ϕ(O$\cdots$H-O)	178.727	172.811	176.729	178.818
O_1-O_2-O_3-O_4	162.034	195.646	143.168	147.066
O_1-O_2-O_3-O_5	162.034	195.646	143.168	147.066

7.1.6 Summary

We summarize the above comparison by plotting the evolution of the oxygen atom separation as a function of the cluster size. These curves, including the predicted distance for ice I_h, are shown in Figure 7.6; Note that for the trimer and pentamer, we have plotted the average value of R(O-O).

In Figure 7.7, we display the evolution of the energy per hydrogen bond for ring clusters of up to 6 molecules. Our value for ice was fitted to the experimental value of 0.58 eV / molec [35] while RWK2 predict 0.555 eV/molec and TIP4P 0.54 eV/molec. The agreement is clearly very good.

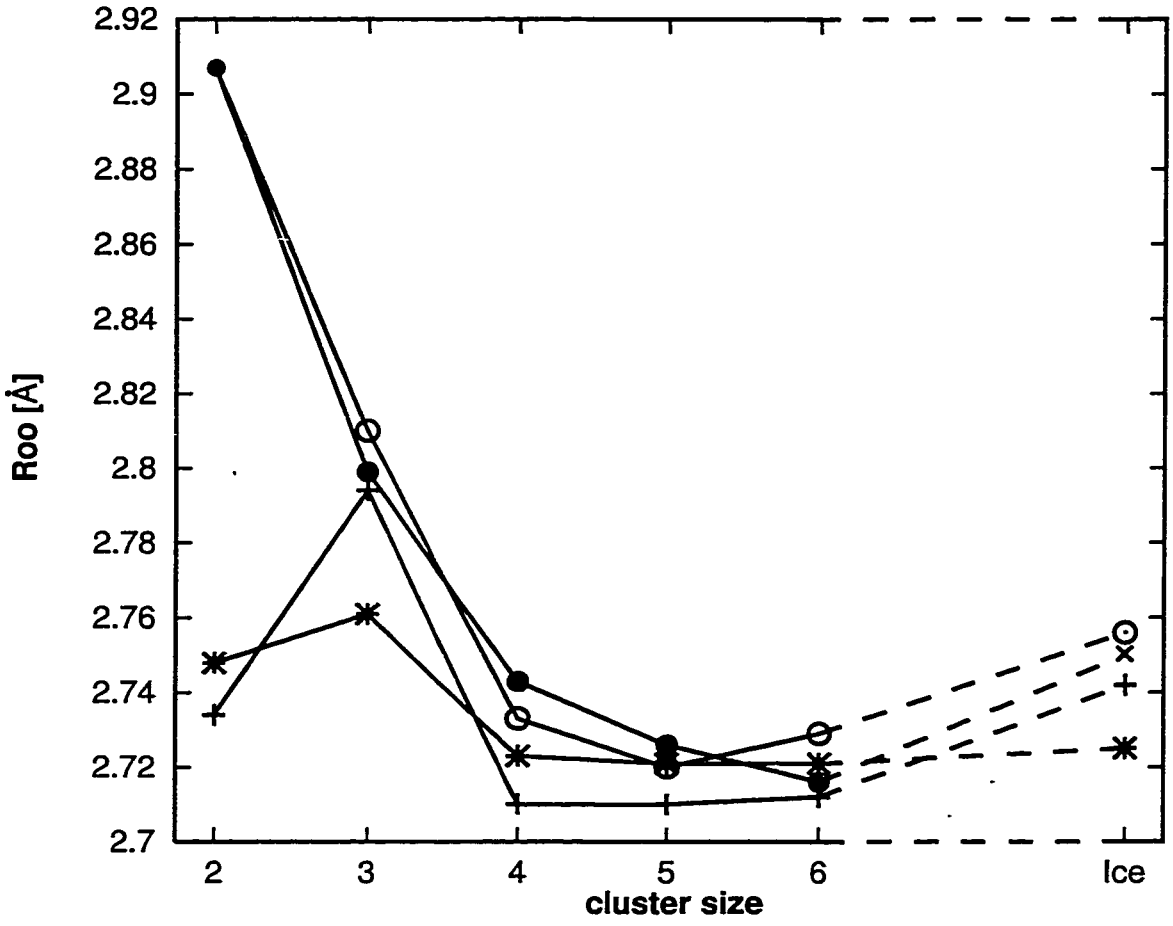

Figure 7.6: Oxygen-oxygen distance for ring clusters and for ice. The '•' represents the value for clusters calculated *ab initio*, 'o' is our new potential, '*' corresponds to TIP4P and '+' are the values for RWK2. The '×' for R(O-O) in ice I_h corresponds to the experimental value.

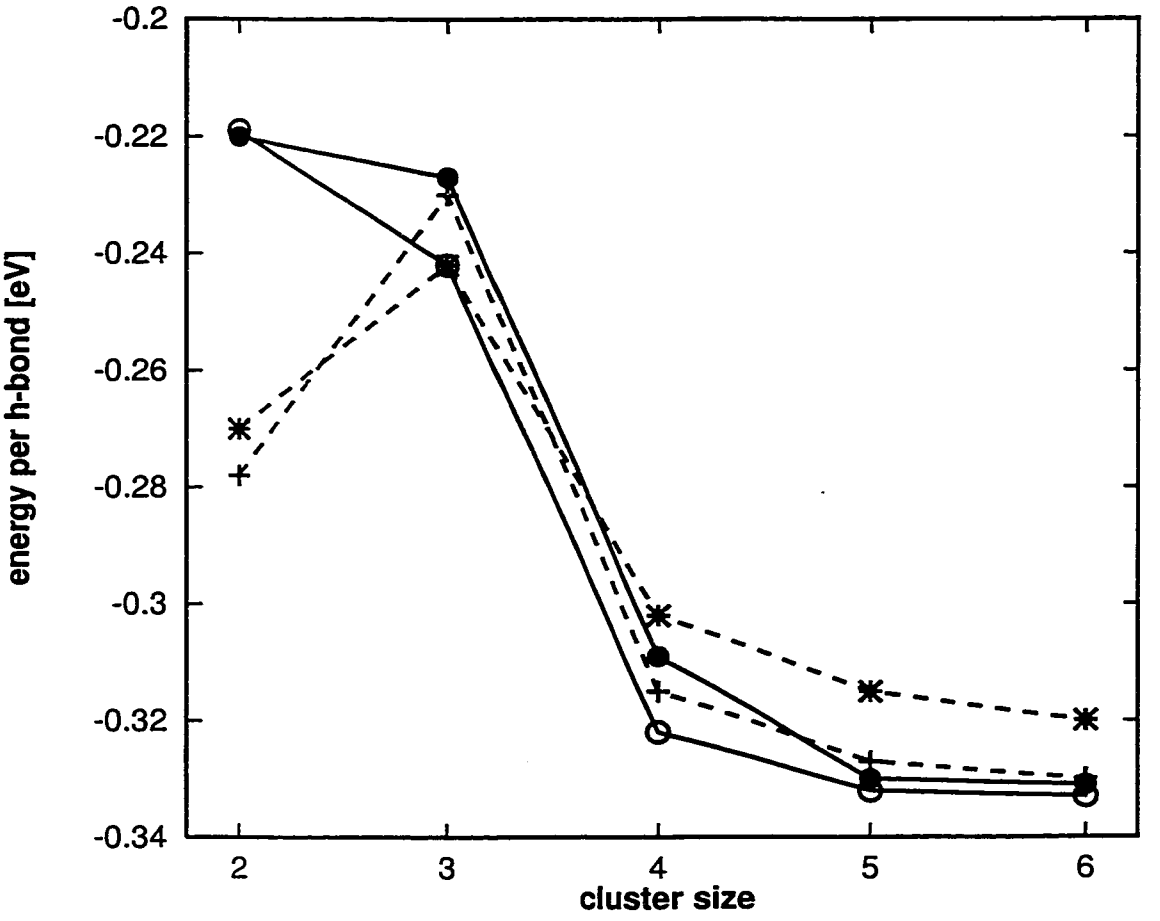

Figure 7.7: Evolution of the energy per bond as a function of the cluster size. The '•' represents the value for clusters calculated *ab initio*, 'o' is our new potential, '∗' correspond to TIP4P and '+' are the values for RWK2.

7.2 *Many-Body Energies*

The polarization of the molecules introduces many-body interactions. The total energy no longer can be written as a sum of pair-wise additive energy terms. The total energy can be written as a series of many-body interaction terms defined as

$$\begin{aligned} U(N) &= U(\mathbf{r}_1, \mathbf{r}_2, \ldots, \mathbf{r}_N) \\ &= \sum_{i=1}^{N} U^{(1)}(\mathbf{r}_i) \\ &\quad + \sum_{i=1}^{N}\sum_{j>i}^{N} U^{(2)}(\mathbf{r}_i, \mathbf{r}_j) \\ &\quad + \sum_{i=1}^{N}\sum_{j>i}^{N}\sum_{k>j}^{N} U^{(3)}(\mathbf{r}_i, \mathbf{r}_j, \mathbf{r}_k) \\ &\quad + \sum_{i=1}^{N}\sum_{j>i}^{N}\sum_{k>j}^{N}\sum_{l>k}^{N} U^{(4)}(\mathbf{r}_i, \mathbf{r}_j, \mathbf{r}_k, \mathbf{r}_l) \\ &\quad \vdots \\ &\quad + U^{(\mathrm{N})}(\mathbf{r}_i, \ldots, \mathbf{r}_N) \end{aligned} \tag{7.1}$$

Here $U^{(1)}$ is the one-body energy. This term is zero in our potential as we do not have internal degrees of freedom. $U^{(2)}$ is the two-body energy, *etc.*

The many-body energy terms can be calculated by freezing the coordinates of the cluster at the desired configuration and calculating the energies of all possible sub-clusters. Then, the two-body interaction terms can be expressed as

$$U^{(2)}(\mathbf{r}_i, \mathbf{r}_j) = U(\mathbf{r}_i, \mathbf{r}_j) - [U^{(1)}(\mathbf{r}_i) + U^{(1)}(\mathbf{r}_j)], \tag{7.2}$$

the three-body energy as

$$\begin{aligned} U^{(3)}(\mathbf{r}_i, \mathbf{r}_j, \mathbf{r}_k) &= U(\mathbf{r}_i, \mathbf{r}_j, \mathbf{r}_k) - [U^{(1)}(\mathbf{r}_i) + U^{(1)}(\mathbf{r}_j) + U^{(1)}(\mathbf{r}_k)] \\ &\quad - [U^{(2)}(\mathbf{r}_i, \mathbf{r}_j) + U^{(2)}(\mathbf{r}_i, \mathbf{r}_k) + U^{(2)}(\mathbf{r}_j, \mathbf{r}_k)], \end{aligned} \tag{7.3}$$

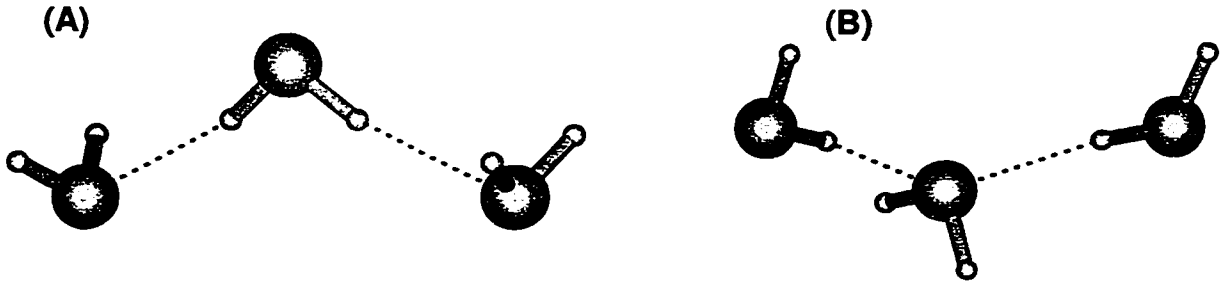

Figure 7.8: Optimized bifurcated water trimer geometries

the four-body energy as

$$\begin{aligned} U^{(4)}(\mathbf{r}_i,\mathbf{r}_j,\mathbf{r}_k,\mathbf{r}_l) &= U(\mathbf{r}_i,\mathbf{r}_j,\mathbf{r}_k,\mathbf{r}_l) - [U^{(1)}(\mathbf{r}_i)+U^{(1)}(\mathbf{r}_j)+U^{(1)}(\mathbf{r}_k)+U^{(1)}(\mathbf{r}_l)] \\ &\quad -[U^{(2)}(\mathbf{r}_i,\mathbf{r}_j)+U^{(2)}(\mathbf{r}_i,\mathbf{r}_k)+U^{(2)}(\mathbf{r}_i,\mathbf{r}_l)+U^{(2)}(\mathbf{r}_j,\mathbf{r}_k) \\ &\quad +U^{(2)}(\mathbf{r}_j,\mathbf{r}_l)+U^{(2)}(\mathbf{r}_k,\mathbf{r}_l)] - [U^{(3)}(\mathbf{r}_i,\mathbf{r}_j,\mathbf{r}_k)+U^{(3)}(\mathbf{r}_i,\mathbf{r}_j,\mathbf{r}_l) \\ &\quad +U^{(3)}(\mathbf{r}_i,\mathbf{r}_k,\mathbf{r}_l)+U^{(3)}(\mathbf{r}_j,\mathbf{r}_k,\mathbf{r}_l)], \end{aligned} \tag{7.4}$$

etc.

ab initio-calculated values of these many-body energy terms, for various water clusters, are available in the literature [94, 4]. We studied three different forms of the water trimer; the ring structure described in Section 7.1.2 and two linear forms of the so-called bifurcated trimers (donor-acceptor-donor and acceptor-donor-acceptor). They are shown in figure 7.8.

The many-body expansion (equation (7.1)) for a trimer terminates at the three-body term. In order to get information about higher-order many-body interactions, we studied the ring tetramer and pentamer introduced in Sections 7.1.3 and 7.1.4, respectively. Table 7.6 shows the comparison of the many-body energy terms, calculated *ab initio* [4], with the prediction of the semiempirical potential presented in this work. Our agreement is reasonably satisfactory with an error of 10% in the total energies. It has been stated in the literature [95] that electrostatic models cannot reproduce well the three-body

Table 7.6: Comparison of the many-body energy terms predicted by our new potential with the values from *ab initio* calculations at MP2 level of theory [4]. All the energies are given in eV.

Cluster	MP2	New Pot.
Trimer:		
[ring structure]		
Total 2-body	-0.512	-0.602
Total 3-body	-0.106	-0.095
(A) [acceptor-donor-acceptor]		
Total 2-body	-0.363	-0.409
Total 3-body	+0.020	+0.020
(B) [donor-acceptor-donor]		
Total 2-body	-0.357	-0.410
Total 3-body	+0.013	+0.018
Tetramer:		
[ring structure]		
Total 2-body	-0.805	-0.901
Total 3-body	-0.270	-0.261
Total 4-body	-0.024	-0.046
Pentamer:		
[ring structure]		
Total 2-body	-0.995	-1.105
Total 3-body	-0.396	-0.363
Total 4-body	-0.051	-0.079
Total 5-body	-0.004	-0.014

energy for bifurcated trimers, yet the three-body energies from our potential agree rather well with the high accuracy *ab initio* MP2 calculated energies. The higher order many-body interactions are also well reproduced, considering the small magnitude of these effects. This illustrates that the dominant many-body effects in the interaction of water molecules come from the electric polarization.

7.3 *Ice I_h Bulk Modulus*

The bulk modulus B, defined as

$$B = \left[V \left(\frac{\partial^2 U}{\partial V^2} \right)_{T=0} \right]_{V=V_0}, \tag{7.5}$$

measures the stiffness of the lattice at its minimum energy configuration. A comparison of the experimental value, *ab initio* DFT and empirical potential is presented in Table 7.7. The table also compares the volume per molecule at the minimum energy configuration at 0 K and the sublimation energy. We found that our new potential predicts these three quantities in agreement with the experimental values. Although the parameters of the new potential (BJX) were chosen to reproduce the experimental values of the density and the cohesive energy, the curvature of the potential energy surface of ice, and therefore the bulk modulus, B, was not taken into consideration during the fitting of the potential parameters.

7.4 *Covalency of the Hydrogen Bond*

In ice I_h hydrogen forms two different types of bonds with its neighboring oxygen atoms, one short ($\sim$ 1Å) and the other long ($\sim$ 1.75Å). The short bond is covalent, but the long one, refered as a hydrogen-bond, is still the subject of the

Table 7.7: Comparison of bulk properties of ice I_h calculated with *ab initio* Density Functional Theory, the empirical potentials TIP4P and RWK2, our new potential (BJX) and experimental values.

Model	Volume [Å^3]	Bulk Modulus [GPa]	Sublimation Energy [eV]
DFT (PW91)†	31.35	13.5	0.55
TIP4P	38.89	16.6	0.585
RWK2§	31.73	18.0	0.555
BJX	32.02	10.9	0.58
Exp.‡	32.05	10.9	0.58

† Ref. [96], § Ref. [20],

‡ Ref. [35]

debate as to whether or not it is purely electrostatic or not (see Reference [97] and references therein).

Our results indicate that an extra term describing the covalency of the hydrogen bond might be necessary. This is noted in the geometry of the water dimer, where the angle between the bisector of the acceptor molecule and the oxygen-oxygen axis form an angle of 103°, instead of the tetrahedral angle (~109.5°) found in the *ab initio* geometries. Also, the energy per hydrogen bond is overestimated in the water trimer and tetramer clusters. A covalent term, mimicking the sp^3 hybridization of the oxygen atoms would include a penalty on these small clusters where the hydrogen bonds are strained, forming angles smaller than 90°, and it would decreace the energy per hydrogen bond. Finally, the difference respect to the *ab initio* values in the two-body energies is larger than that of the three-body energy. An extra two-body term for the hydrogen

bond could help to fix the two-body energies without affecting the agreement already achieved in the three-body energies.

Chapter 8

DIFFUSION AND ISLAND FORMATION ON THE ICE I_h BASAL PLANE SURFACE

8.1 Abstract

In this chapter, we present theoretical calculations of the adsorption, diffusion, and island formation of water admolecules on the basal plane surface of an ice I_h crystal. These calculations were done using the semi-empirical potential of interaction developed in the previous chapters of this thesis. At low coverage, we find that an admolecule prefers to sit at non-crystallographic sites on the surface (*i.e.* sites that do not fit into the ice lattice). Since ice I_h is proton-disordered, no two sites are exactly the same and there is a wide range of binding energies. For some local environments, the binding energy is on the order of, or even larger than, the cohesive energy. The proton disorder also results in a range of activation energies for diffusion. After mapping out a large number of diffusion barriers, using the Nudged Elastic Band method, a kinetic Monte Carlo calculation of the diffusion at 140 K was performed. At early time, the mean-squared displacement has anomalous scaling with time as is common for diffusion on random lattices. However, at longer time, the scaling is normal and a diffusion coefficient can be obtained. The diffusivity is consistent with a recent experimental upper bound given by Brown and George. The energetics and dynamics of the formation of small islands on the ice surface have also been studied. It is found that islands up to and including pentamer are non-crystallographic, but the hexamer is crystallographic. While the formation of

a crystallographic hexamer from a non-crystallographic pentamer and a new admolecule involves a complex concerted motion of all the island molecules and a large relaxation of the substrate, the activation energy for the process is estimated to be quite small, smaller than the admolecule diffusion barrier.

8.2 Introduction

It is well known that ice I_h is disordered in that even though the oxygen atoms are placed on a regular, hexagonal lattice, the protons can be pointing in various directions [89]. This results in a significant excess entropy at low temperature, where the rearrangement of the orientation of the molecules is too slow to reach a perfectly ordered crystal. The disorder also has very interesting consequences for the surface dynamics, as described below.

Computer simulation studies of ice surface dynamics necessarily require efficient potential energy functions to describe the intermolecular interactions. While it is beginning to be possible to do *ab initio* DFT calculations of ice surfaces, the size of the simulation cell and the complexity of the phenomena make *ab initio* calculations still far too CPU intensive. Many different empirical potential functions have been proposed to describe water [25, 26, 27, 20, 21, 22, 23, 24]. Most of these have been developed mainly to reproduce liquid water properties with little attention paid to crystalline ice. We will be using the potential introduced in previous chapters (see Chapter 5), which we expect will work better for molecules that are on the surface and/or at transition states along a diffusion path, that is, neither in the gas phase nor in the bulk.

8.3 Basal Plane Surface of Ice I_h

A sample of ice I_h is shown in Figure 8.1. This represents the simulation cell used in most of the calculations presented here. The top layer is the surface

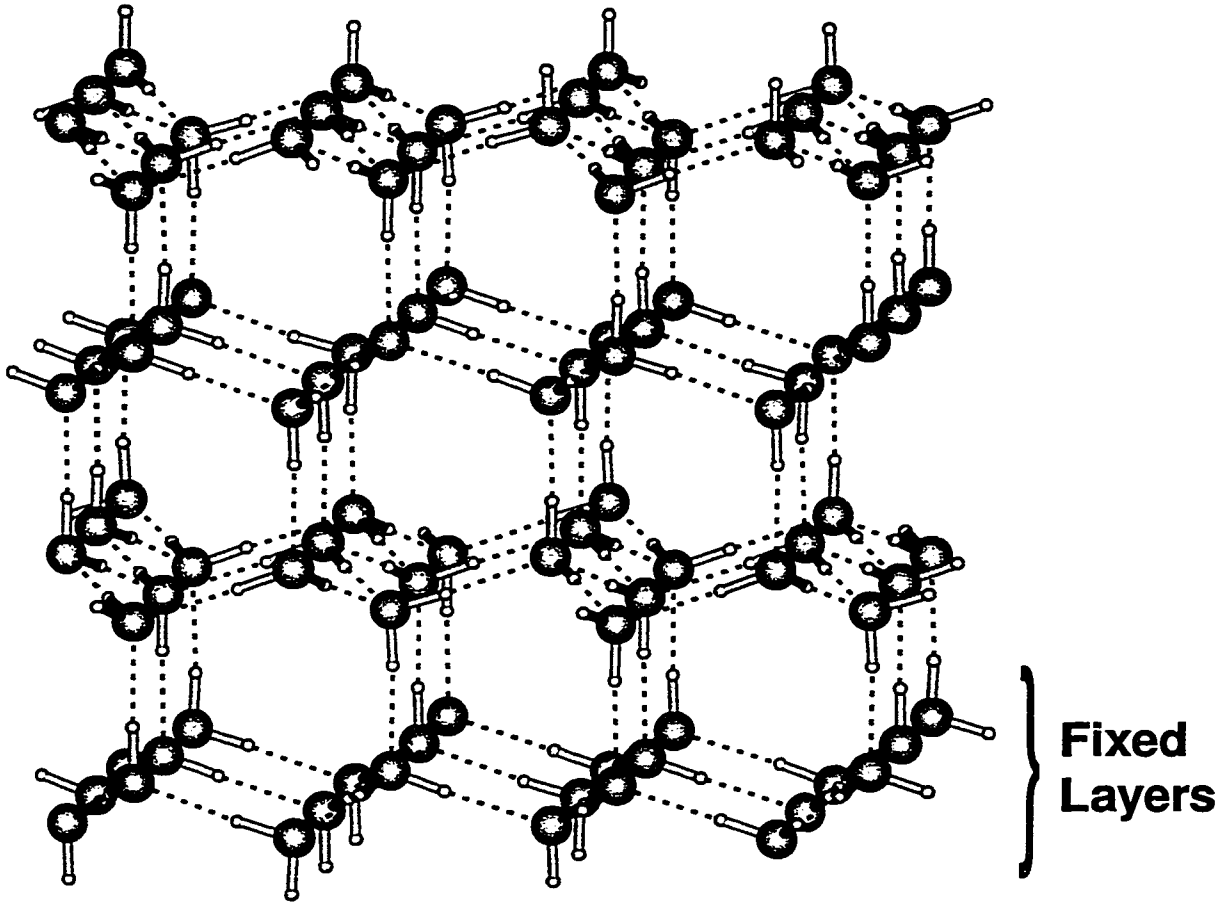

Figure 8.1: A side view of a slab of four bilayers of proton disordered ice I_h used for most of the surface studies presented here. The basal plane surface is the top-most layer. The bottom bilayer is held rigid. Periodic boundary conditions are used to mimic bilayers of infinite extent.

layer. This cut of the crystal gives a basal plane surface. Pairs of layers are close together, in so called bilayers, while the distance between the pairs is quite large. On average, 50% of the molecules have a proton pointing out of the surface. In order to mimic the attachment of this slab to a semi-infinite crystal, the bottom two layers of the slab are held fixed during the simulations and periodic boundary conditions are imposed on the lateral edges of the simulation box.

Recent helium atom scattering results have shown clearly that the ice surface at about 140 K is indeed very regular [98]. There is no sign of surface reconstruction at this low temperature. He-atom scattering is very sensitive to defects, so the fact that intense and narrow diffraction peaks are observed means that the abundance of defects is low (see, for example, Ref. [99, 100]). LEED experiments indicate that the top layer has a large mean squared displacement, on the order of 0.25 Å, and this has been supported by dynamics simulations using the TIP4P potential [101, 102].

8.4 Adsorption Sites

We have identified the various adsorption sites by simulating deposition of molecules on the surface and then quenching the system to the nearest local minimum on the potential surface. The sticking coefficient was found to be unity for vapor deposition [103].

Due to the proton disorder, there are many different adsorption sites on the surface. While long-range effects are important, mainly because of the long-range electrostatic interaction, it is useful to group the sites into categories according to the local, nearest-neighbor environment. In all cases, there are three molecules in the surface plane that are close to the admolecule. The binding energy strongly depends on how many of the protons in these surface

molecules are pointing up from the surface. There can be at most three protons pointing up, one from each of the surface molecules, or there can be two, one or no protons pointing up (see Figure 8.2). The strongest binding is found when one proton is pointing up. Representative configurations are shown in Figures 8.2a and 8.3a. We call these sites A-sites. The oxygen atom on the admolecule attracts the proton of the surface molecule while the two protons of the admolecule get attracted towards the oxygen atoms on the surface molecules that do not have a proton pointing away from the surface. Slightly weaker binding (on average) is found when two surface protons are pointing up towards the admolecule. One of the protons of the admolecule then ends up pointing up away from the surface. We call these B-sites. Figures 8.2b and 8.3b show representative configurations. Much weaker binding is found when none of the three neighboring surface molecules has a proton pointing up from the surface, so called C-sites. When all three have a proton pointing up, most of the times a stable binding sites for the admolecule is not formed. When placed above and in between the three surface molecules, the admolecule slides over to an adjacent A- or B-site. In rare occasions, the surface can get stressed and give rise to a weakly bound D-site.

In A- and B-sites, the admolecule forms three strained hydrogen bonds. The binding energy is, therefore, quite close to the cohesive energy in ice, which corresponds to two hydrogen bonds per molecule. The A-sites are, in fact, found to have binding energiies in the range of 0.56 ± 0.06 eV, 10% of them binding an adatom stronger than a kink-site (where the binding energy is necessarily equal to the cohesive energy, 0.58 eV). This is a very unusual situation. It can only arise because there is a large variety of binding sites on the surface. It means that admolecules will prefer to sit at these strongly binding A-sites, rather than attach to kink-sites. The surface will therefore tend to have a certain, low coverage of admolecules, even when the mobility is great enough

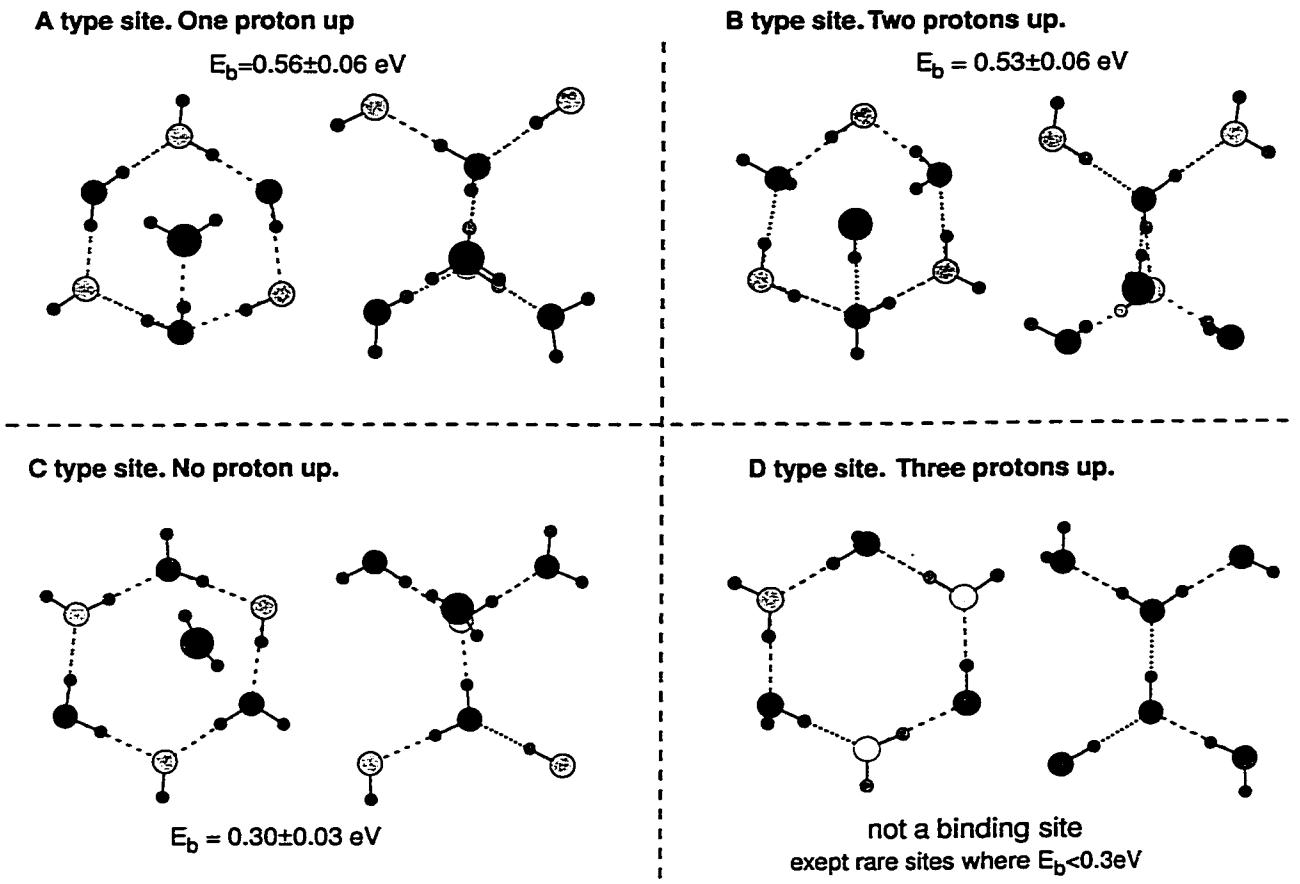

Figure 8.2: Various types of binding sites for admolecules on the basal plane surface. The figure shows molecules in the top bilayer as well as the admolecule. The strongest binding is at A-type sites where one of the three neighboring surface molecules has a proton pointing up (out of the surface). After the admolecule binds to the site, the proton is pointing towards the admolecule. At B-type sites there are two protons pointing up, at C-type sites there is none. If all three neighboring surface molecules have a proton pointing up, the admolecule does not have a stable binding site (D-type). For the A-type sites it makes a significant difference whether the lower layer in the bilayer has a molecule directly underneath the admolecule or not. Surprisingly, the binding energy at A-type sites can be significantly larger than the cohesive energy. Note the large relaxation in the top layer due to the binding of the admolecule.

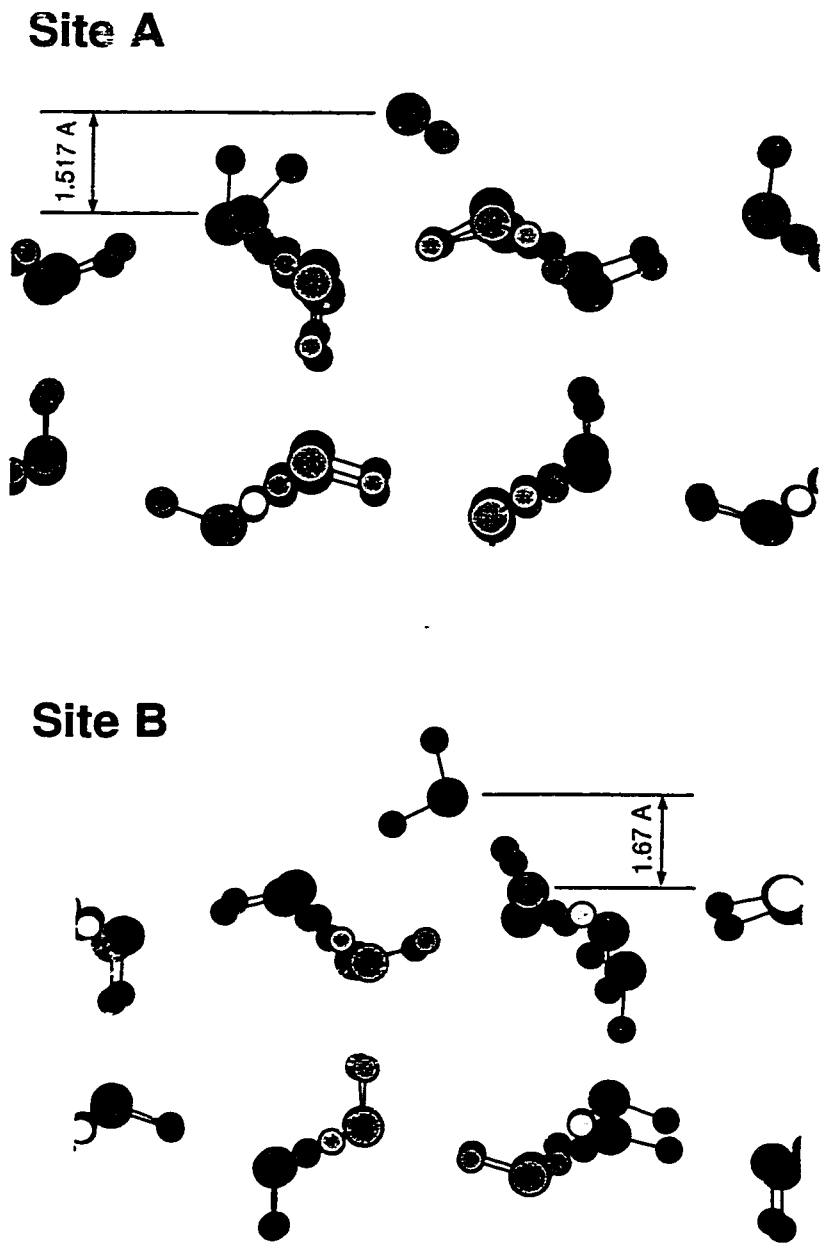

Figure 8.3: A side view of the relaxed configuration of an admolecule at an A-type site (top) and at a B-type site (bottom). At the A-type site the two protons of the admolecule are pointing towards oxygen atoms in the surface layer, while a proton from the third neighboring surface molecule points towards the oxygen atom of the admolecule. In this configuration, three weak hydrogen bonds form and the binding energy can be greater than the cohesive energy of the solid (which amounts to two hydrogen bonds). At the B-type site, one of the protons of the admolecule is pointing up while the other points down towards an oxygen atom in the surface layer. Two protons from the top layer are pointed towards the oxygen atom of the admolecule.

for the atoms to diffuse to the kink-sites.

Some of the B-sites also have binding energy larger than the cohesive energy, but only a very small fraction. The binding energy is in the range of 0.53 ± 0.06 eV, overlapping to some extent with the range of binding energy for A-sites. The classification of sites according to the nearest three surface molecules only gives a rough indication of the properties of the site. The fact that there are long-range Coulomb interactions and that the relaxation of the disordered lattice is very substantial means that any short-range classification scheme is necessarily incomplete. The C-sites lead to a distinctly smaller binding energy than the A- and B-sites, 0.30 eV. A full histogram of the binding energies for proton-disordered ice surfaces is shown in Figure 8.4 At low temperature, a diffusing admolecule will largely be confined to A- and B-sites (see section 8.6).

The surface molecules bound to the admolecule undergo a substantial relaxation, the oxygen atoms sometimes moving by more than half an Ångstrom. In the absence of surface relaxation, the binding energy is typically 0.1 to 0.2 eV lower. In an earlier study by Hale and coworkers involving a frozen substrate, the binding energies they found [104, 105] were smaller than the ones we deduced. While they used a different interaction potential, the main reason for the difference is the lack of surface relaxation in their calculations. When we freeze the surface molecules in our calculations, we get results that are quite similar to the results of Hale and coworkers.

8.5 Diffusion Barriers

Calculating the activation energy barriers for diffusive hops of the admolecule is challenging since many degrees of freedom are involved, not just the coordinates of the admolecule but also those of the nearby surface molecules, as there

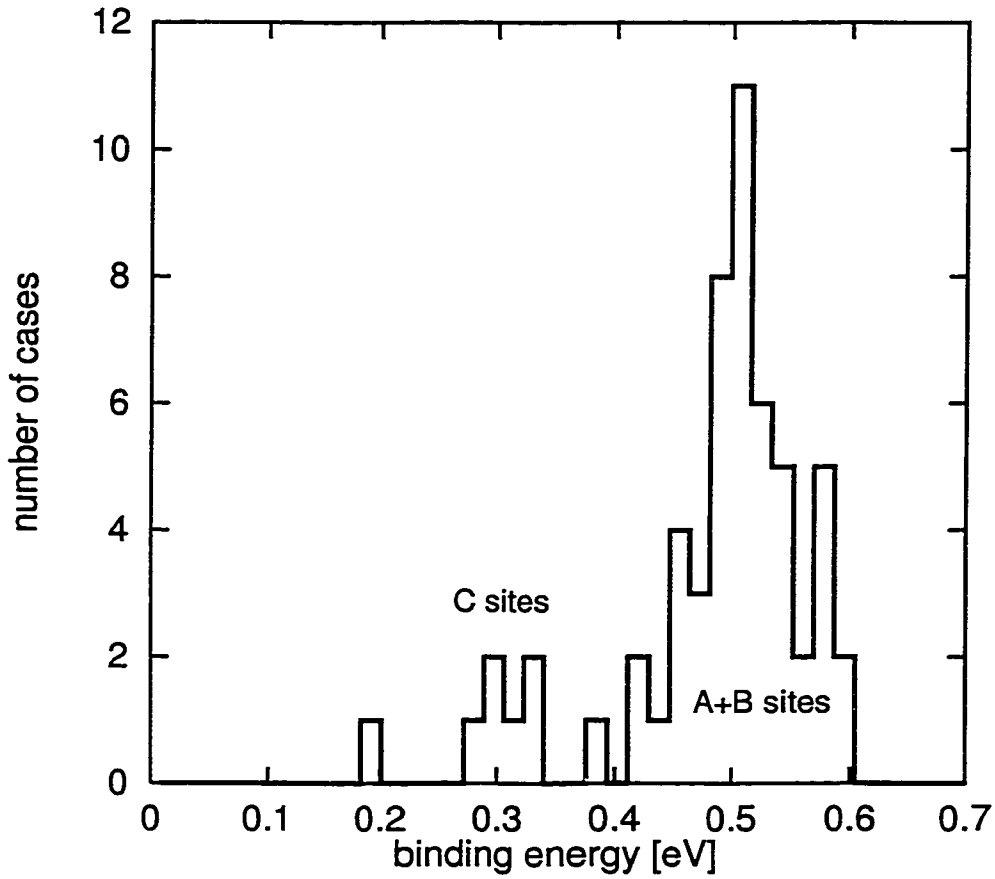

Figure 8.4: Histogram of the binding energy for an admolecule on the surface of ice I_h. The dispersion in the binding energy is due to the proton disorder present in ice.

are large relaxations in the substrate. We have used the 'Nudged Elastic Band' method to obtain a discrete representation of the minimum-energy paths for various diffusion hops [106, 107]. An example of such a calculation is given in Figure 8.5 where a hop from an A-site to an adjacent B-site is shown with 11 replicas of the system discretizing the minimum-energy path. The calculation was started by first creating a straight line interpolation between the initial and final sites, sometimes making intermediate guesses in the interpolation. These intermediate points were found by constraining some degrees of freedom at and letting the others relax. The algorithm for relaxing the chain of images to the minimum energy path has been described by Mills *et al* [106, 107]. Sometimes more than one minimum-energy path exists between a given initial and final state. Therefore, several different initial paths were tried, corresponding to different orientations of the admolecule at the mid-point of the path. The activation-energy barrier was then extracted as the maximum potential energy along the optimal minimum-energy path.

This analysis gave a range of barriers, depending on the environment of the diffusing molecule. For hops between the lowest energy sites, the A- and B-sites, the barriers range around 0.2 eV, but they can be as low as 0.05 eV and as high as 0.3 eV. Hops into C-sites have larger barriers, typically larger than 0.30 eV. Again, it is very important to include the surface relaxations in the calculations. If the substrate is kept frozen, the barriers are lower by about 0.1 eV.

We have carried out preliminary analysis of the prefactor, ν, in the Arrhenius expression for the rate

$$k = \nu \, e^{-E_a/kT} \tag{8.1}$$

by simulating the classical dynamics of the system ('molecular dynamics' simulation [108]) and extracting vibrational frequencies from the velocity autocor-

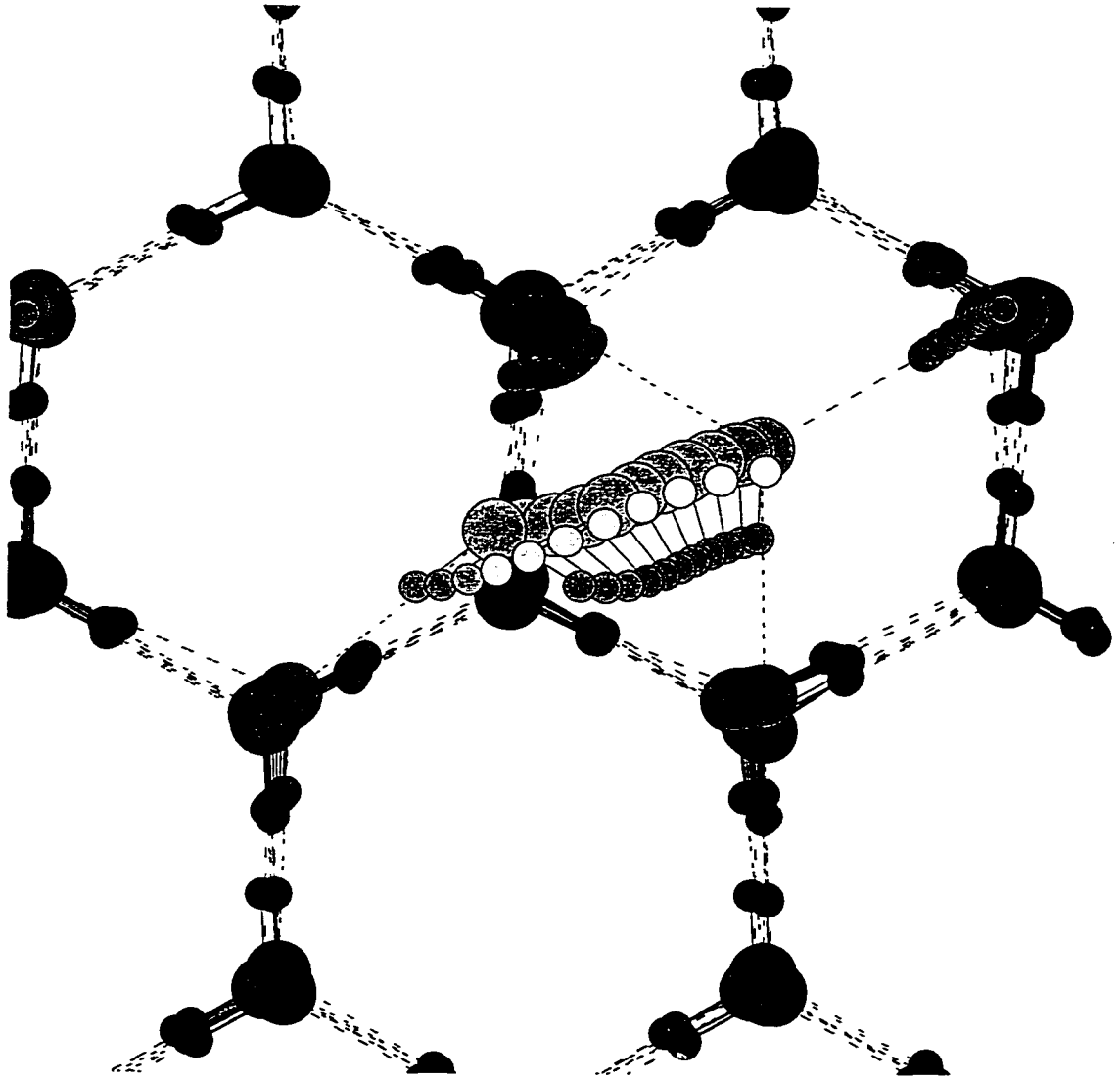

Figure 8.5: The minimum-energy diffusion path between an A-type site (on the left) to a B-type site (on the right). The path is discretized with 11 replicas and was found via the NEB method. One of the protons of the admolecule rotates from pointing down in the A-site to pointing up in the B-site. Notice the large relaxation of atoms in the surface layer. These surface relaxations can be as large as 0.5 Å.

relation function. The results indicate that the prefactors are on the order of 10^{12} sec^{-1}, which is typical for surface diffusion hops [109].

8.6 Simulation of Long-time Diffusion

A direct classical dynamics simulation of the diffusion is not practical. Such simulations necessarily include the vibrational motion of the molecules and are therefore limited to time steps that are about one order of magnitude smaller than the vibrational period ($\sim 10^{-14}$ sec). A hop over a barrier of 0.16 eV occurs, on the average, every 10^{-5} sec at 140 K. A direct classical dynamics simulation would require on the order of 10^9 iterations, which would take about 10^6 hours of CPU time (many years) on a workstation. By increasing the temperature, the rate of surface diffusion hops can be increased, but in order to see a hop every hour of CPU time, the temperature would need to be raised above 400 K, but this would lead to melting; a clear example of a crossover from one diffusion mechanism to another as temperature is changed.

After the stable binding-sites have been found and the activation-energy barriers for hops between the sites have been calculated, it is possible to simulate the long-time-scale diffusion of an admolecule using the kinetic Monte Carlo method [110, 111, 112, 113]. Using this method, a table of all possible events in the system is created and random numbers are used to select which process takes place next. The vibrational motion of the molecules is not included, and the time-step, Δt, in the iterative algorithm is essentially the average time interval between occurrences of the fastest process included in the table of possible events:

$$\Delta t = -\frac{\ln(x)}{\tau}. \tag{8.2}$$

Note that x is a random number between 0 and 1 and τ is the total expected escape rate for the system at the present stable location. The total expected

escape rate is the sum over the escape rates for all possible escape routes.

On a 13 Å by 15 Å sample, all the binding sites and activation barriers of diffusion were calculated (see Figure 8.6).

To simplify the calculation, the C- and D-sites where not included in the kinetic Monte Carlo simulation because they are rarely visited at low temperature.

The A- and B-sites form a sublattice on the ice surface, and the connected pathways between these sites form a random percolating network. For a larger sample of proton disordered ice, this surface sublattice is shown in Figure 8.7. The prefactor was assumed to be 10^{12} sec^{-1} for all diffusion hops.

The results of 50,000 repeated kinetic Monte Carlo simulations were used to obtain the mean-squared displacement of an admolecule as a function of time. For short time, when the molecules have traveled less than *ca.* 10 Å, the scaling is anomalous; the mean-squared displacement increases nearly as the square root of time. However, at longer times, the normal scaling is observed: $\langle r^2 \rangle \sim t$ and a diffusion coefficient, D, could be extracted from the proportionality constant:

$$D = \frac{1}{4}\frac{\delta r^2}{\delta t} \tag{8.3}$$

(see Appendix C for a deduction of this relation on a hexagonal lattice). We find a diffusivity of 7×10^{-10} cm^2/sec at 140 K that agrees with the upper bound for the surface diffusivity, set experimentally by Brown and George, to the value of 5×10^{-9} cm^2/sec at that same temperature [5].

We repeated the kinetic Monte Carlo simulations for a range of temperature (see Figure 8.8). The calculated diffusivity roughly follows an Arrhenius law with an effective activation barrier of 0.22 eV.

Another experimental information on surface diffusion is the measurement by Sitz and Isacson [114]. They measured the sticking coefficient of HCl mole-

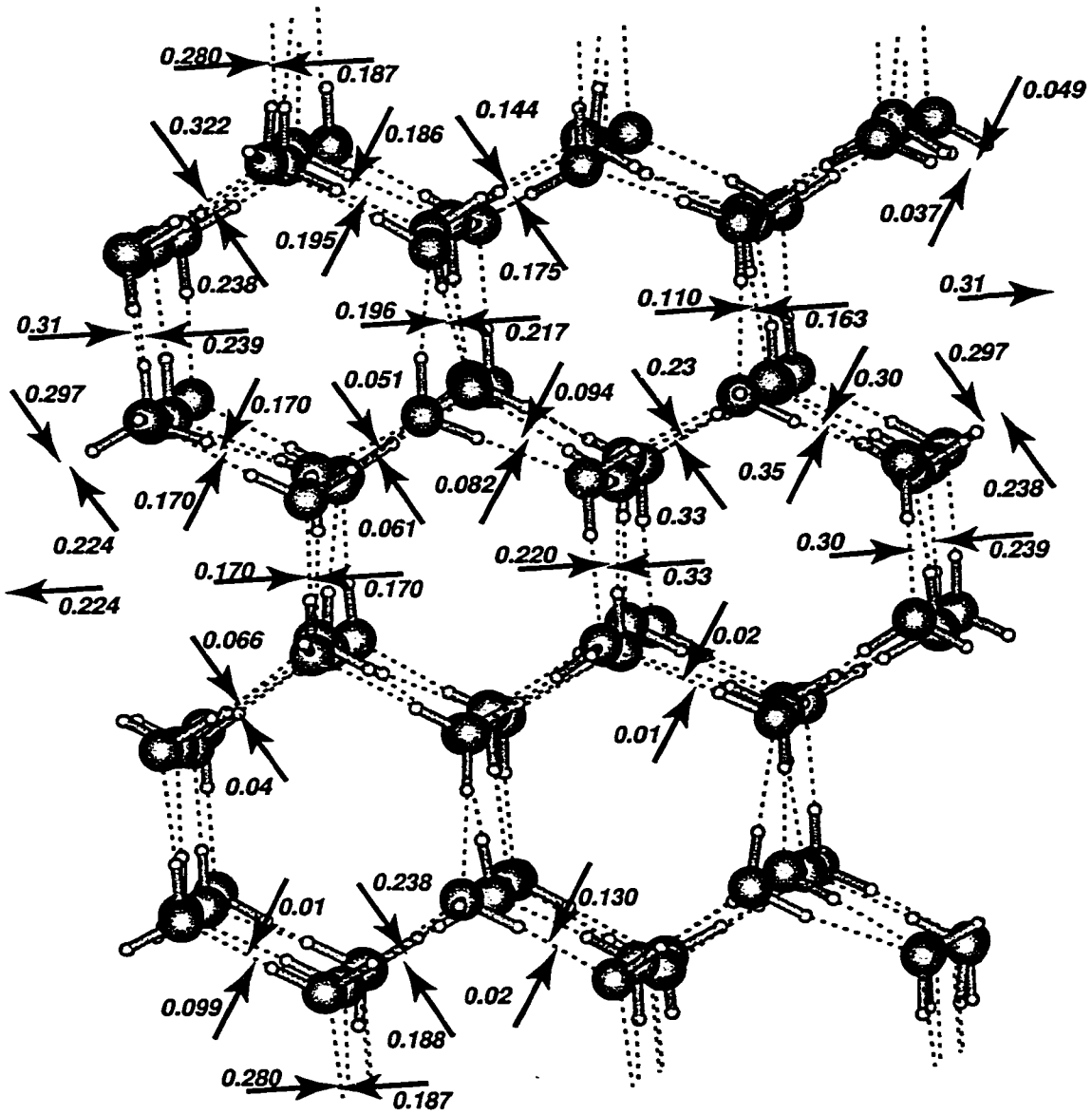

Figure 8.6: Activations barriers for diffusion. These energies were calculated by using the Nudged Elastic Band method on a basal surface of ice I_h

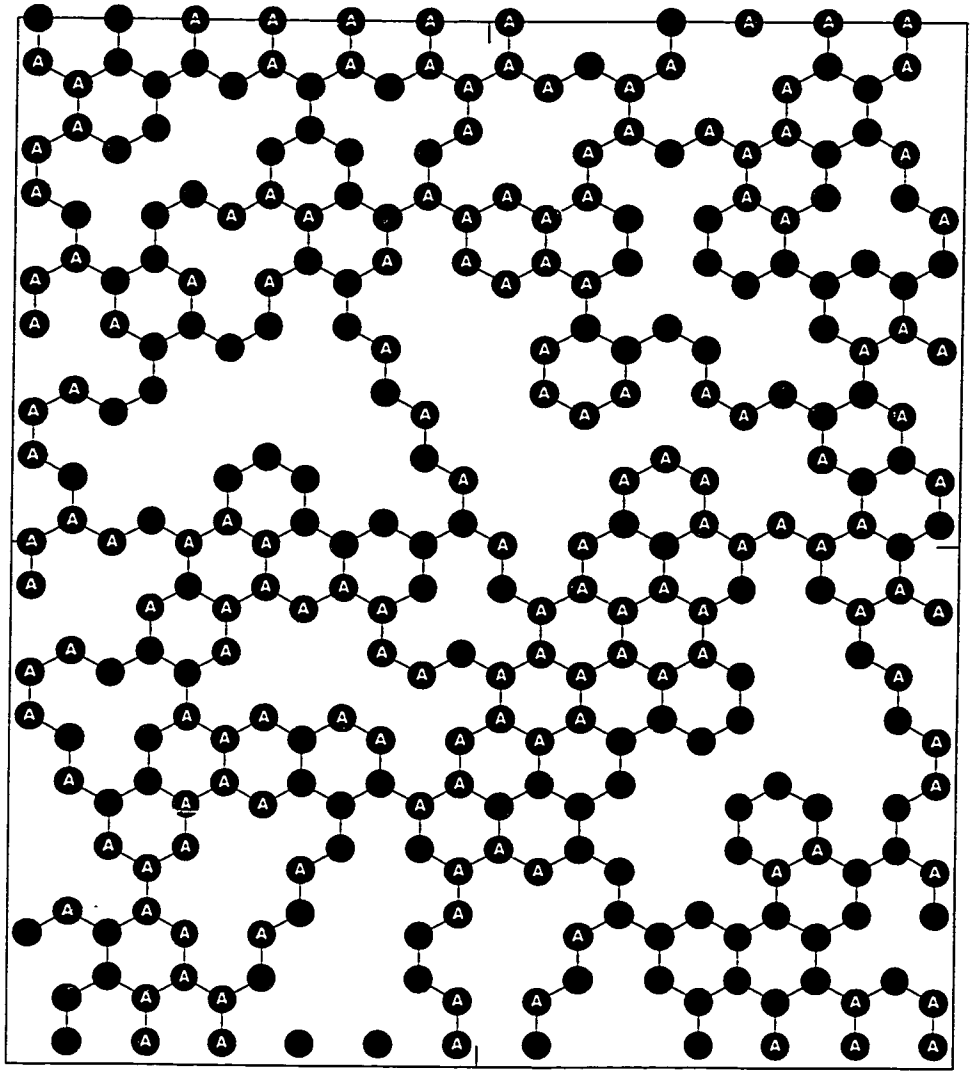

Figure 8.7: Active diffusion paths on a large sample of proton-disordered ice. Only the more stable sites, A and B, are shown since other sites are of too high energy to play an active role at low temperature. A line is drawn between sites where the barrier is low enough for the transition to be active at 140 K. The proton-disordered surface thus creates a random lattice of sites and pathways for the diffusing admolecule. A kinetic Monte Carlo simulation of the diffusivity on this lattice was carried out using the harmonic transition state theory estimate of the hopping rate, given the binding energy and barriers obtained from the structural relaxation and NEB minimum energy path calculations. The mean-squared displacement at short times is anomalous due to the disorder, but at long time it increases linearly with time and a diffusion coefficient can be obtained from the slope.

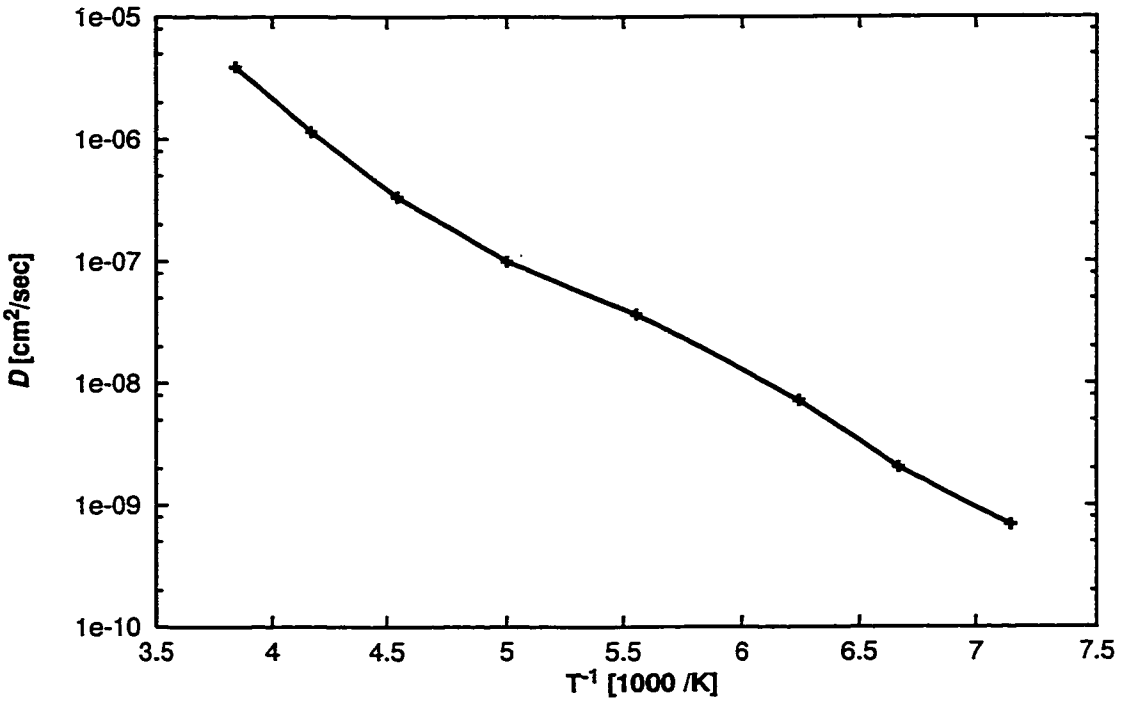

Figure 8.8: Arrhenius plot for the diffusivity of water molecules on the surface of ice as a function of the inverse of the temperature. The effective activation barrier, 0.22 eV, is the slope of this graph.

cules on thin film ice surfaces. It was found that to model the data they needed to include three processes: sticking, desorption and loss. The loss channel referred to a process that makes the HCl molecules unavailable for desorption. Sitz and Isakson found an activation energy for the loss channel of 0.22 eV and they interpreted this channel as the onset of water diffusion on the ice surface and subsequent ionization or hydration of the HCl molecule. Our calculated activation energy for single molecule diffusion on the ice surface predicts the same value as the activation energy of the loss channel in Sitz and Isakson's experiment giving stranght to their interpretation.

8.7 Island Formation

An important aspect of crystal growth is the formation of islands on the surface and nucleation of a new surface layer of the crystal. While the admolecule on the basal plane of the ice I_h surface sits in a non-crystallographic site, an island that serves as a nucleus for the growth of a new surface layer must be crystallographic. The question then arises as to what island size the crystallographic arrangements of the molecules become preferred.

In order to address this issue, we carried out simulated annealing studies of island shapes, ranging from the dimer to the hexamer. We started the simulation with a configuration obtained from the perfect crystal, heated the configuration up to 190 K for 3 psec, and then cooled it down over a couple of psec until a potential energy minimum was reached. The results are shown in Figure 8.9. The dimer and up to the pentamer are all non-crystallographic. Only when the island has grown to a hexamer is the crystallographic configuration optimal. This complexity will likely have implications for the nucleation of new surface layers during growth.

One interesting question is: What is the limiting step for growing an ice

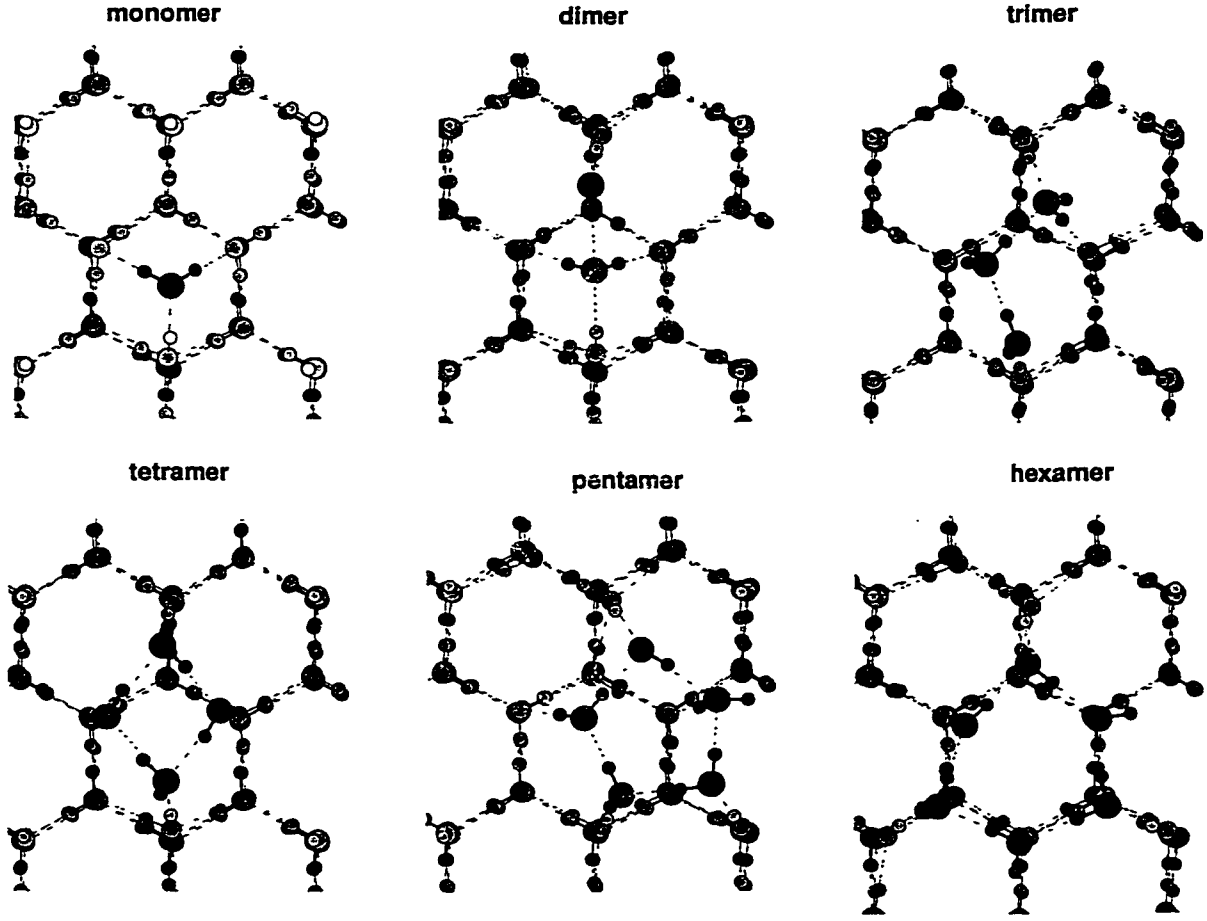

Figure 8.9: Stable configurations of small islands of admolecules on the ice I_h surface. Up to and including the pentamer the lowest energy configuration is non-crystallographic, *i.e.* it does not fit within the ice crystal structure. The configurations were obtained by starting with a hexamer island carved out of an ice lattice, annealing at 190 K for 3 psec and then cooling down slowly. After removing one of the molecules and annealing again, the non-crystallographic configuration of the pentamer was obtained. An analogous procedure was used for the smaller clusters. Note that all these clusters are unstable with respect to dissociation into isolated adatoms at A-type binding sites.

crystal rather than an amorphous solid? That is, what is the highest activation energy in the process of assembling a crystallographic hexamer from six admolecules? We have calculated the minimum energy paths for the formation of the dimer from two admolecules, the formation of the trimer from a dimer and an admolecule, *etc.* The minimum-energy path for forming a crystallographic hexamer from a pentamer and an admolecule is shown in Figure 8.10. This is a very complex transition involving the concerted displacement of many molecules and large relaxation of the underlying molecules. Nevertheless, the activation energy for this event is not very high, only 0.1 eV. The variation of the potential energy along the minimum-energy path is shown in Figure 8.11. A shallow metastable intermediate state is found from the path optimization. Even though this step is slightly downhill, this is an artifact of the proximity of the sixth molecule to the pentamer. If the extra molecule were at an A-type binding site a few lattice spacing away, the initial energy would be 0.07 eV lower than the configuration with the hexagonal island. All the islands are metastable with respect to admolecules in the very strongly binding A-sites.

8.8 Conclusions

The results presented here illustrate that dynamics at ice surfaces are quite complex with a significant range of binding energies for admolecules and activation barriers for diffusion. This energy range of binding sites and diffusion barriers on the surface is due to of the proton disorder.

The presence of binding-sites for admolecules with a binding energy that exceeds the cohesive energy is particularly intriguing.

The obvious question then arises as to how smooth the surface is during growth and during measurements. Experiments using He-atom scattering have certainly indicated that the ice I_h surface at 140 K is highly ordered [98].

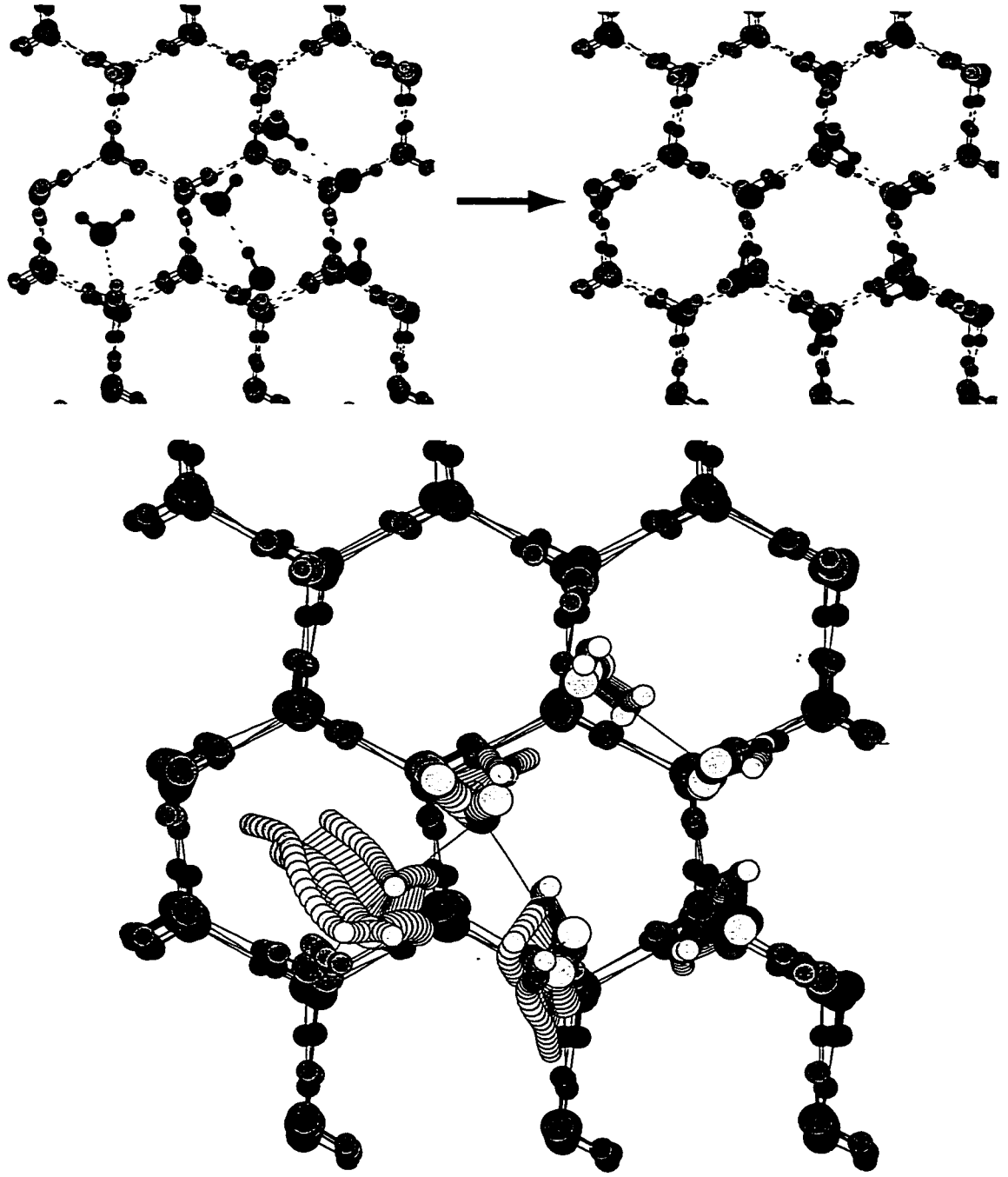

Figure 8.10: Minimum-energy path for the formation of a crystallographic hexamer island from a non-crystallographic pentamer and a nearby ad-molecule. The path was found using the NEB method. The initial state is shown in the top left part of the figure and the final state on the top right. The lower part of the figure shows the path discretized with 30 replicas of the system. Note the large relaxations in the substrate molecules.

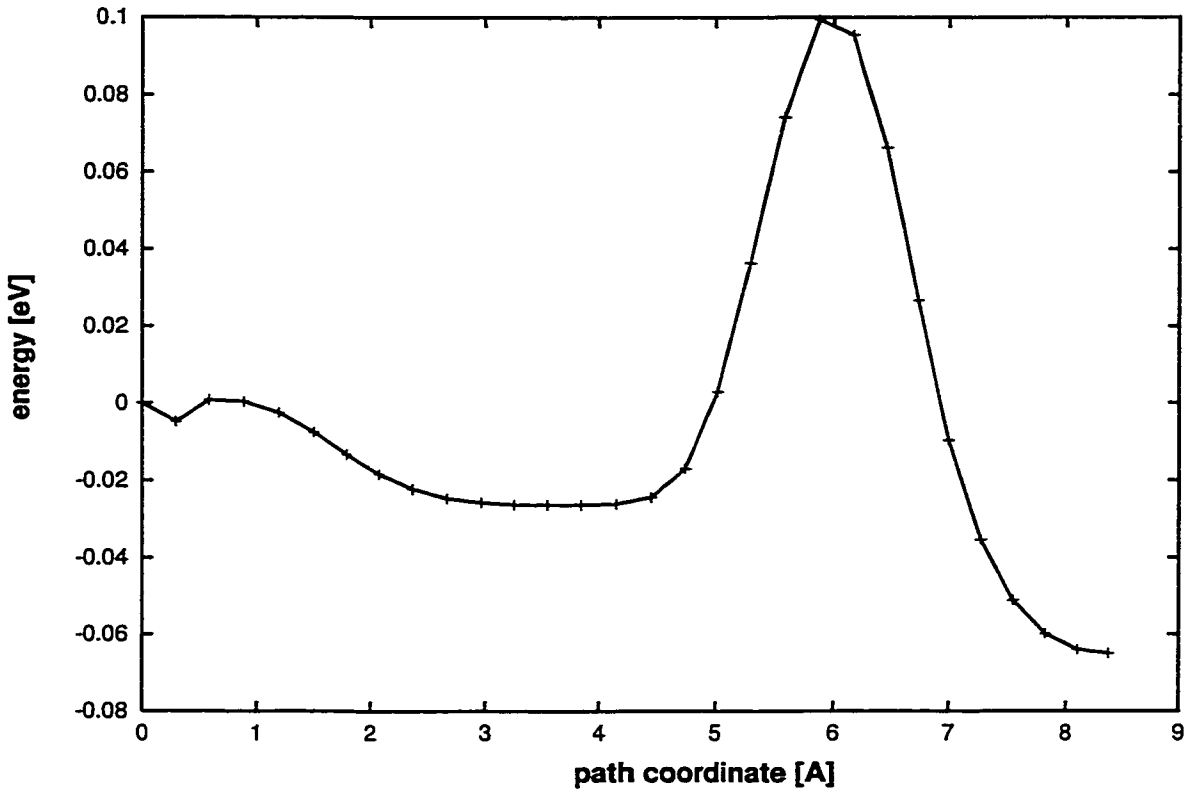

Figure 8.11: Change in the potential energy along the minimum energy path for the formation of the hexamer, shown in Figure 8.10. The path goes through a metastable intermediate configuration. While this is a complex transition involving concerted motion of many molecules, the activation energy is quite small, 0.1 eV, significantly smaller than the barrier for the diffusion hop of an admolecule on the flat surface.

The presence of this small percentage of stronger binding sites should not pose a contradiction to the well-ordered surfaces observed experimentally. If the surface is annealed in vacuum, some desorption will occur (the desorption rate is quite high at 150 K). The energy required to desorb a molecule from the flat surface is calculated to be 0.75 eV if a proton is pointing out of the surface, and 0.79 eV if both protons are pointed towards neighboring molecules. This is a substantially higher energy than the strongest binding energy, 0.62 eV. A desorbing surface is, therefore, most likely going to be flat, *i.e.* most of the time the surface is flat. However, under growth conditions, the strong binding-sites will be filled before kink-sites get filled, so the surface will not be flat.

The fact that clusters up to and including the pentamer are non-crystallographic can have interesting implications for nucleation of new islands on the surface during growth. The nucleation process is complex and the critical island size is likely to be large even at low temperatures. More work needs to be done to study this phenomena.

We point out, finally, that the simulations presented here can only be representative of the ice surface at low temperature. At temperatures above *ca.* 150 K the desorption rate becomes very high. In order to have a stable surface, the vapor pressure has to be appreciable and the deposition rate is high. The surface layer is very dynamic: it is a balance between rapid adsorption and desorption. It is an interesting, open question as to what the surface looks like under those conditions. At still higher temperatures, above *ca.* 240 K, the surface is likely liquid-like and the diffusion mechanism is very different from the one presented here. The simulations of Kroes, using the TIP4P potential, show surface melting at these high temperatures and very large diffusivity in the surface layer [14], but experimental measurements are difficult and so far inconclusive.

BIBLIOGRAPHY

[1] J. Verhoeven and A. Dymanus, J. Chem. Phys. **52**, 3222 (1970).

[2] R. Glaeser and C. Coulson, Trans. Faraday Soc. **61**, 389 (1965).

[3] E. R. Batista, S. S. Xantheas, and H. Jónsson, J. Chem. Phys. **109**, 4546 (1998).

[4] M. Hodges, A. Stone, and S. Xantheas, J. Phys. Chem. A **101**, 9163 (1997).

[5] D. Brown and S. George, J. Phys. Chem. **100**, 15460 (1996).

[6] K. Cuffey *et al.*, Science **270**, 455 (1995).

[7] H. Clausen *et al.*, in *Ice core studies of global biogeochemical cycles*, edited by R. Delmas (Springer-Verlag, Berlin Heidelberg, 1995).

[8] S. J. Johnsen, Quaternary Research **43**, 117 (1995).

[9] K. Cuffey and E. Steig, J. of Glaciology **44**, 273 (1998).

[10] B. Mason, Proc. R. Soc. Lond. A **441**, 3 (1993).

[11] M. Baker, Science **276**, 1072 (1997).

[12] M. Baker, in *Ice physics and the natural environment*, edited by J. Wettlaufer, J. Dash, and N. Untersteiner (Springer-Verlag, Berlin Heidelberg New York, 1999), Vol. 56, p. 121.

[13] J. Dash, Contemp. Phys. **30**, 89 (1989).

[14] G.-J. Kroes, Surf. Sci. **275**, 365 (1992).

[15] B. Mason and J. Dash, in *Ice physics and the natural environment*, edited by J. Wettlaufer, J. Dash, and N. Untersteiner (Springer-Verlag, Berlin Heidelberg New York, 1999), Vol. 56, p. 321.

[16] J. Dash, in *Ice physics and the natural environment*, edited by J. Wettlaufer, J. Dash, and N. Untersteiner (Springer-Verlag, Berlin Heidelberg New York, 1999), Vol. 56, p. 11.

[17] K. Itagaki, J. Glaciol. **121**, 12 (1973).

[18] O. Dengel and N. Riehl, Phys. Kondens. Mater **1**, 191 (1963).

[19] B. J. Mason, G. W. Bryant, and A. P. van den Heuvel, Phil. Mag. **8**, 505 (1963).

[20] J. Reimers, R. Watts, and M. Klein, Chemical Physics **64**, 95 (1982).

[21] W. L. Jorgensen *et al.*, J. Chem. Phys. **79**, 926 (1983).

[22] H. Berendsen, J. Grigera, and T. Straatsma, J. Phys. Chem. **91**, 6269 (1987).

[23] P. Cieplak, P. Kollman, and T. Lybrand, J. Chem. Phys. **92**, 6755 (1990).

[24] L. Dang, J. Chem. Phys. **97**, 2659 (1992).

[25] O. Matsuoka, E. Clementi, and M. Yoshimine, J. Chem. Phys. **64**, 1351 (1976).

[26] F. Stillinger and A. Rahman, J. Chem. Phys. **68**, 666 (1978).

[27] P. Barnes, J. L. Finney, J. D. Nicholas, and J. E. Quinn, Nature **12**, 107 (1979).

[28] C. Coulson and D. Eisenberg, Proc. R. Soc. Lond. A **291**, 445 (1966).

[29] T. Dyke and J. Muenter, J. Chem. Phys. **59**, 3125 (1973).

[30] E. Whalley, Chem. Phys. Lett. **53**, 449 (1978).

[31] D. Adams, Nature **293**, 447 (1981).

[32] S. Carnie and G. Patey, Mol. Phys. **47**, 1129 (1982).

[33] D. Eisenberg and W. Kauzmann, *The Structure and Properties of Water* (Oxford University Press, New York and Oxford, 1969).

[34] J. Bernal and R. Fowler, J. Phys. Chem. **1**, 515 (1933).

[35] P. V. Hobbs, *Ice Physics* (Clarendon Press, Oxford, 1974).

[36] J. Hayward and J. Reimers, J. Chem. Phys. **106**, 1518 (1997).

[37] A. J. Stone, *The Theory of Intermolecular Forces* (Clarendon Press, Oxford, 1996).

[38] R. M. Weeny and K. Ohno, Proc. R. Soc. Lond. A **255**, 367 (1960).

[39] W. Murphy, J. Chem. Phys. **67**, 5877 (1977).

[40] C. Millot *et al.*, J. Phys. Chem. A **102**, 754 (1998).

[41] C. Dykstra, S. Liu, and D. Malik, Adv. Chem. Phys. **75**, 37 (1989).

[42] A. D. Buckingham, Adv. Chem. Phys. **12**, 107 (1967).

[43] C. E. Dykstra, Acc. Chem. Res. **21**, 355 (1988).

[44] S. S. Xantheas, J. Chem. Phys. **102**, 4505 (1995).

[45] S. S. Xantheas, Phil. Mag. B **73**, 107 (1996).

[46] S. S. Xantheas and J. T. H. Dunning, J. Chem. Phys. **99**, 8774 (1993).

[47] J. K. Gregory *et al.*, Science **275**, 814 (1997).

[48] K. Liu, M. G. Brown, and R. J. Saykally, J. Phys. Chem. A **101**, 8995 (1997).

[49] J. Caldwell, L. X. Dang, and P. A. Kollman, J. A. Chem. Soc. **112**, 9145 (1990).

[50] L. X. Dang and T.-M. Chang, J. Chem. Phys. **106**, 8149 (1997).

[51] M. Sprik, J. Chem. Phys. **95**, 6762 (1991).

[52] K. Laasonen, M. Sprik, M. Parrinello, and R. Car, J. Chem. Phys. **99**, 9080 (1993).

[53] D. Wei and D. R. Salahub, Chem. Phys. Lett. **224**, 291 (1994).

[54] E. S. Fois, M. Sprik, and M. Parrinello, Chem. Phys. Lett. **223**, 411 (1994).

[55] C. Gatti, B. Silvi, and F. Colonna, Chem. Phys. Lett **247**, 135 (1995).

[56] M. I. Heggie, C. D. Latham, S. C. P. Maynard, and R. Jones, Chem. Phys. Lett. **249**, 485 (1996).

[57] A. J. Stone, Chem. Phys. Lett. **83**, 233 (1981).

[58] A. J. Stone and M. Alderton, Mol. Phys. **56**, 1047 (1985).

[59] R. S. Mulliken, J. Chem. Phys. **23**, 1833 (1955).

[60] C. Edmiston and K. Ruedenberg, Rev. Mod. Phys. **35**, 457 (1963).

[61] J. E. Carpenter and F. Weinhold, J. Mol. Struct. (THEOCHEM) **169**, 41 (1988).

[62] J. Pipek and P. G. Mezey, J. Chem. Phys. **90**, 4916 (1989).

[63] R. Bader, *Atoms in Molecules. A Quantum Theory* (Oxford University Press, Oxford, 1990).

[64] B. Møller and M. S. Plesset, Phys. Rev. **46**, 618 (1934).

[65] S. S. Xantheas and J. T. H. Dunning, J. Chem. Phys. **98**, 8037 (1993).

[66] S. S. Xantheas and J. T. H. Dunning, in *Advances in Molecular Vibrations and Collision Dynamics*, edited by Z. Bacic and J. M. Bowman (JAI press, Stanford, 1998), Vol. 3, p. 281.

[67] R. A. Kendall and R. J. H. T. H. Dunning, Jr., J. Chem. Phys. **96**, 6796 (1992).

[68] K. Liu *et al.*, Nature **381**, 501 (1996).

[69] N. Troullier and J. Martins, Phys. Rev. B **43**, 1993 (1991).

[70] C. Lee *et al.*, Phys. Rev. B **47**, 4863 (1993).

[71] A. Becke, Phys. Rev. A **38**, 3098 (1988).

[72] J. Perdew, Phys. Rev. B **33**, 8822 (1986).

[73] J. Perdew, in *Electronic Structure of Solids '91*, edited by P. Ziesche and H. Eschrig (Akademie Verlag, Berlin, 1991), p. 11.

[74] J. P. Perdew and Y. Wang, Phys. Rev. B **45**, 13244 (1992).

[75] J. Bernal and R. Fowler, J. Chem. Phys. **1**, 515 (1933).

[76] B. P. Uberuaga, E. R. Batista, and H. Jónsson, *Submitted to J. Chem. Phys.*, 1998, elastic sheet method for identifying atoms in molecules.

[77] *Gaussian 94, Revision* **E.2**, Gaussian, Inc., Pittsburgh, PA, 1995, m. J. Frisch, G. W. Trucks, H. B. Schlegel, P. M. W. Gill, B. G. Johnson, M. A. Robb, J. R. Cheeseman, T. Keith, G. A. Petersson, J. A. Montgomery, K. Raghavachari, M. A. Al-Laham, V. G. Zakrzewski, J. V. Ortiz, J. B. Foresman, J. Cioslowski, B. B. Stefanov, A. Nanayakkara, M. Challacombe, C. Y. Peng, P. Y. Ayala, W. Chen, M. W. Wong, J. L.,res, E. S. Replogle, R. Gomperts, R. L. Martin, D. J. Fox, J. S. Binkley, D. J. Defrees, J. Baker, J. P. Stewart, M. Head-Gordon, C. Gonzalez and J. A. Pople.

[78] B. Stefanov and J. Cioslowski, J. Comp. Chem **16**, 1394 (1995).

[79] N. Ashcroft and N. Mermin, *Solid State Physics* (Saunders College, Fort Worth, 1976).

[80] C. Millot and A. J. Stone, Mol. Phys. **77**, 439 (1992).

[81] T. P. Lybrand and P. A. Kollman, J. Chem. Phys. **83**, 2923 (1985).

[82] C. E. Dykstra, J. Phys. Chem. **91**, 6216 (1987).

[83] J. Perez and M. Dupuis, J. Phys. Chem. **95**, 6526 (1991).

[84] S.-Y. Liu and C. E. Dykstra, J. Phys. Chem. **90**, 3097 (1986).

[85] D. J. Malik and C. E. Dykstra, J. Chem. Phys. **83**, 6307 (1985).

[86] J. D. Augsburger and C. E. Dykstra, J. Chem. Phys. **88**, 3817 (1988).

[87] P. Hohenberg and W. Kohn, Phys. Rev. B **136**, 864 (1964).

[88] W. Kohn and L. J. Sham, Phys. Rev. A **140**, 1133 (1965).

[89] J. Bernal and R. Fowler, J. Chem. Phys. **1**, 515 (1933).

[90] D. Margofiash, T. Proctor, T. Zeiss, and W. Meath, J. Mol. Phys. **35**, 747 (1978).

[91] K. Tang and J. Toennies, J. Chem. Phys. **80**, 3726 (1984).

[92] A. Goldstein and H. Jónsson, Philosophical Magazine B **71**, 1041 (1995).

[93] D. Coker and R. Watts, J. Phys. Chem. **91**, 2513 (1987).

[94] S. Xantheas, J. Chem. Phys. **100**, 7523 (1994).

[95] Y.-P. Liu *et al.*, J. Chem. Phys. **108**, 4739 (1998).

[96] D. Hamann, Phys. Rev. B **55**, R10157 (1997).

[97] E. Isaacs *et al.*, Phys. Rev. Lett. **82**, 600 (1999).

[98] J. Braun *et al.*, Phys. Rev. Lett. **80**, 2638 (1998).

[99] H. Jónsson, J. Weare, and A. Levi, Surf. Sci. **1948**, 126 (1984).

[100] G. Elliott, H. Jónsson, D. Miller, and J. Weare, J. of Vac. Sci. and Technol. **3**, 1665 (1985).

[101] N. Materer *et al.*, J. Phys. Chem. **99**, 6267 (1995).

[102] N. Materer *et al.*, Surf. Sci. **381**, 190 (1997).

[103] E. R. Batista, B. D. Kay, and H. Jónsson, *In preparation*, 1999.

[104] J. Kiefer and B. Hale, J. Chem. Phys. **67**, 3206 (1977).

[105] B. Hale, J. Kiefer, and C. Ward, J. Chem. Phys. **75**, 1991 (1981).

[106] G. Mills, H. Jónsson, and G. Schenter, Surf. Sci. **324**, 305 (1995).

[107] H. Jónsson, G. Mills, and K. W. Jacobsen, in *Classical and Quantum Dynamics in Condensed Phase Simulations*, edited by B. J. Berne, G. Ciccotti, and D. F. Coker (World Scientific, NJ, 1998), p. 385.

[108] W. Swope, H. Andersen, P. Berens, and K. Wilson, J. Chem. Phys. **76**, 637 (1982).

[109] G. Kellogg, Surf. Sci. Reports **21**, 1 (1994).

[110] D. Gillespie, J. Comp. Phys. **22**, 403 (1976).

[111] D. Gillespie, J. Phys. **81**, 2340 (1977).

[112] D. Gillespie, J. Comp. Phys. **28**, 395 (1978).

[113] A. Voter, Phys. Rev. B **34**, 6819 (1986).

[114] G. Sitz and M. Isakson, J. Phys. Chem. (1998). *In press* .

Appendix A

EXPLICIT EXPRESSIONS FOR THE FIRST AND SECOND DERIVATIVES OF THE ELECTROSTATIC POTENTIAL

In this appendix we give the explicit expressions of the electrostatic potential, and its first two derivatives, to facilitate the implementation and use of the potential energy surface presented in Chapter 5.

A.1 First Derivative

The electrostatic potential for a charge distribution with multipole moments up to hexadecapole moment is given by

$$U = \frac{\mathcal{P}_i\, r_i}{r^3} + \frac{\mathcal{Q}_{ij}\, r_i\, r_j}{r^5} + \frac{\mathcal{O}_{ijk}\, r_i\, r_j\, r_k}{r^7} + \frac{\mathcal{H}_{ijkl}\, r_i\, r_j\, r_k\, r_l}{r^9} \tag{A.1}$$

where $\mathbf{r} = \mathbf{r}_i - \mathbf{r}_j$ and $\mathcal{P}$, $\mathcal{Q}$, $\mathcal{O}$, $\mathcal{H}$ are the dipole, quadrupole, octopole and hexadecapole moments, respectively.

The first derivative of the potential is the negative of the electric field

$$U_{;i} = U_{;i}^{(\mathrm{d})} + U_{;i}^{(\mathrm{q})} + U_{;i}^{(\mathrm{o})} + U_{;i}^{(\mathrm{h})} \tag{A.2}$$

$$= -\mathbf{E}_i^{(\mathrm{d})}(\mathbf{r}) - \mathbf{E}_i^{(\mathrm{q})}(\mathbf{r}) - \mathbf{E}_i^{(\mathrm{o})}(\mathbf{r}) - \mathbf{E}_i^{(\mathrm{h})}(\mathbf{r}) \tag{A.3}$$

where the dipole field is

$$\mathbf{E}_i^{(\mathrm{d})}(\mathbf{r}) = 3\,\frac{\mathcal{P}_s\, r_s}{r^5}\, r_i - \frac{\mathcal{P}_i}{r^3}, \tag{A.4}$$

the quadrupole field is

$$\mathbf{E}_i^{(\mathrm{q})}(\mathbf{r}) = 5\,\frac{\mathcal{Q}_{st}\, r_s\, r_t}{r^7}\, r_i - 2\,\frac{\mathcal{Q}_{si}\, r_s}{r^5}, \tag{A.5}$$

the octopole field is

$$\mathbf{E}_i^{(o)}(\mathbf{r}) = 7\,\frac{\mathcal{O}_{stu}\,r_s\,r_t\,r_u}{r^9}\,r_i - 3\,\frac{\mathcal{O}_{ist}\,r_s\,r_t}{r^7} \tag{A.6}$$

and the hexadecapole field is

$$\mathbf{E}_i^{(h)}(\mathbf{r}) = 9\,\frac{\mathcal{H}_{stuv}\,r_s\,r_t\,r_u\,r_v}{r^{11}}\,r_i - 4\,\frac{\mathcal{H}_{istu}\,r_s\,r_t\,r_u}{r^9}. \tag{A.7}$$

A.2 Second Derivative

Using then notation introduced in Chapter 5, the second derivatives of the potential $U_{;ij}$ are

$$\begin{aligned} U_{;ij} &= U_{;ij}^{(d)} + U_{;ij}^{(q)} + U_{;ij}^{(o)} + U_{;ij}^{(h)} && \text{(A.8)} \\ &= -\mathbf{E}_{i;j}^{(d)} - \mathbf{E}_{i;j}^{(q)} - \mathbf{E}_{i;j}^{(o)} - \mathbf{E}_{i;j}^{(h)} && \text{(A.9)} \end{aligned}$$

where the dipole field component is

$$\mathbf{E}_{i;j}^{(d)} = -\frac{15}{r^7}(\mathcal{P}_s\,r_s)\,r_i\,r_j + \frac{3}{r^5}[\mathcal{P}_i\,r_j + \mathcal{P}_j\,r_i + (\mathcal{P}_s\,r_s)\delta_{ij}], \tag{A.10}$$

the quadrupole field is

$$\begin{aligned} \mathbf{E}_{i;j}^{(q)} &= -\frac{35}{r^9}(\mathcal{Q}_{st}\,r_s\,r_t)r_i\,r_j + \frac{5}{r^7}[(\mathcal{Q}_{st}\,r_s\,r_t)\,\delta_{ij} \\ &\quad +2(\mathcal{Q}_{si}\,r_s\,r_j + \mathcal{Q}_{sj}\,r_s\,r_i)] - \frac{2}{r^5}\,\mathcal{Q}_{ij}, \end{aligned} \tag{A.11}$$

the octopole field

$$\begin{aligned} \mathbf{E}_{i;j}^{(o)} &= -\frac{63}{r^{11}}(\mathcal{O}_{stu}\,r_s\,r_t\,r_u)\,r_i\,r_j \\ &\quad +\frac{7}{r^9}[(\mathcal{O}_{stu}\,r_s\,r_t\,r_u)\,\delta_{ij} + 3\,(\mathcal{O}_{ist}\,r_s\,r_t\,r_j + \mathcal{O}_{jst}\,r_s\,r_t\,r_i)] \\ &\quad -\frac{6}{r^7}\,\mathcal{O}_{ijs}\,r_s, \end{aligned} \tag{A.12}$$

and the hexadecapole field is

$$
\begin{aligned}
\mathbf{E}^{(\mathrm{h})}_{i;j} \;=\; & -\frac{99}{r^{13}}(\mathcal{H}_{stuv}\, r_s\, r_t\, r_u\, r_v)\, r_i\, r_j \\
& +\frac{9}{r^{11}}\{(\mathcal{H}_{stuv}\, r_s\, r_t\, r_u\, r_v)\, \delta_{ij} \\
& +4\,[(\mathcal{H}_{istu}\, r_s\, r_t\, r_u)\, r_j + (\mathcal{H}_{jstu}\, r_s\, r_t\, r_u)\, r_i]\} \\
& -\frac{12}{r^9}\mathcal{H}_{ijst}\, r_s\, r_t. \qquad \textbf{(A.13)}
\end{aligned}
$$

Appendix B

DEFINITIONS OF MULTIPOLE MOMENTS

Several different definitions of the multipole moments of a charge density are in use in the literature. The differences among them are signs, constants of proportionality and some being linear combinations of the others. In this appendix, we give the definitions of the multipoles used in Table 1 in Cartesian coordinates.

The total charge density of the molecule $\rho(\mathbf{r})$ is

$$\rho(\mathbf{r}) = \rho_e(\mathbf{r}) + \sum_i q_i \, \delta(\mathbf{r} - \mathbf{r}^{(i)}) \tag{B.1}$$

in which ρ_e is the electronic charge density, q_i and $\mathbf{r}^{(i)}$ are the ionic charges (one proton charge for each of the hydrogen atoms and 8 for the oxygen) and the position of the i-th ion, respectively, and $\delta(\mathbf{r})$ is the Dirac delta function. Note that the sum is over all the nuclear charges. The molecular multipole moments are obtained by integrating over the charge density of the molecule. The electric dipole moment is defined as

$$\mathcal{P}_i = \int d^3r \; \rho(\mathbf{r}) \; r_i. \tag{B.2}$$

The quadrupole moment is defined as

$$\mathcal{Q}_{ij} = \frac{1}{2} \int d^3r \; \rho(\mathbf{r}) \; (3 \; r_i \; r_j - r^2 \; \delta_{ij}) \tag{B.3}$$

where δ_{ij} is the Kroeneker delta. We chose to measure $\mathbf{r}$ from the center of mass of the molecule. The octopole moments are defined as

$$\mathcal{O}_{ijk} = \frac{1}{3!} \int d^3r \; \rho(\mathbf{r}) \; [15 \; r_i \; r_j \; r_k - 3 \; r^2 \; (r_i \; \delta_{jk} + r_j \; \delta_{ki} + r_k \; \delta_{ij})] \tag{B.4}$$

and the components of the hexadecapole are defined as

$$\mathcal{H}_{ijkl} = \frac{1}{4!}\int d^3r\ \rho(\mathbf{r})\ [105\ r_i\ r_j\ r_k\ r_l \ - \ 15\ r^2\ (r_i\ r_j\ \delta_{kl} + r_i\ r_k\ \delta_{jl} + r_i\ r_l\ \delta_{jk} + r_j\ r_k\ \delta_{il} + r_j\ r_l\ \delta_{ik} + r_k\ r_l\ \delta_{ij}) + 3\ r^4\ (\delta_{ij}\ \delta_{kl} + \delta_{ik}\ \delta_{jl} + \delta_{il}\ \delta_{jk})]. \qquad \text{(B.5)}$$

Appendix C

DIFFUSION EQUATION FOR PARTICLES ON A TWO DIMENSIONAL HEXAGONAL LATTICE

C.1 Diffusion Equation

The probability, $P(\mathbf{r}, t+\delta t)$ that the particle is at $\mathbf{r}$ at time $t+\delta t$ is the same as the probability that it had been in a neighboring cell at time t and then hopped into the cell in consideration:

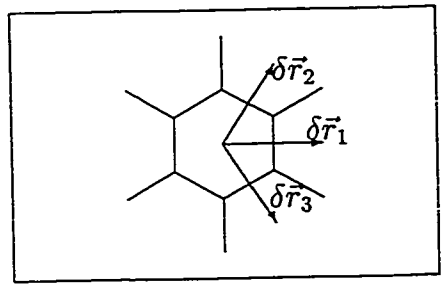

$$
\begin{aligned}
&P(\mathbf{r}, t+\delta t) = \\
&\quad \frac{1}{6}\left[P(\hat{\mathbf{r}}+\delta\hat{\mathbf{r}}_1, t) + P(\hat{\mathbf{r}}-\delta\hat{\mathbf{r}}_1, t) + P(\hat{\mathbf{r}}+\delta\hat{\mathbf{r}}_2, t)\right. \\
&\quad \left. + P(\hat{\mathbf{r}}-\delta\hat{\mathbf{r}}_2, t) + P(\hat{\mathbf{r}}+\delta\hat{\mathbf{r}}_3, t) + P(\hat{\mathbf{r}}-\delta\hat{\mathbf{r}}_3, t)\right].
\end{aligned} \tag{C.1}
$$

Subtracting on both sides $P(\mathbf{r}, t)$ and dividing by δt,

$$
\begin{aligned}
&\frac{P(\mathbf{r}, t+\delta t) - P(\mathbf{r}, t)}{\delta t} = \\
&\quad \frac{\delta r^2}{6\,\delta t}\left[\frac{P(\hat{\mathbf{r}}+\delta\hat{\mathbf{r}}_1, t) - 2\,P(\hat{\mathbf{r}}, t) + P(\hat{\mathbf{r}}-\delta\hat{\mathbf{r}}_1, t)}{\delta r^2}\right. \\
&\quad + \frac{P(\hat{\mathbf{r}}+\delta\hat{\mathbf{r}}_2, t) - 2\,P(\hat{\mathbf{r}}, t) + P(\hat{\mathbf{r}}-\delta\hat{\mathbf{r}}_2, t)}{\delta r^2} \\
&\quad \left. + \frac{P(\hat{\mathbf{r}}+\delta\hat{\mathbf{r}}_3, t) - 2\,P(\hat{\mathbf{r}}, t) + P(\hat{\mathbf{r}}-\delta\hat{\mathbf{r}}_3, t)}{\delta r^2}\right]
\end{aligned} \tag{C.2}
$$

in which $\delta r = |\delta\vec{r}_1| = |\delta\vec{r}_2| = |\delta\vec{r}_3|$. Taking the limit as $\delta t \to 0$ and $\delta r \to 0$ and keeping the fraction $\delta r^2/\delta t$ finite, we have the following:

$$\frac{\partial P}{\partial t} = \frac{\delta r^2}{6\delta t}\left[\frac{\partial^2 P}{\partial \hat{r}_1^2} + \frac{\partial^2 P}{\partial \hat{r}_2^2} + \frac{\partial^2 P}{\partial \hat{r}_3^2}\right]. \tag{C.3}$$

Since $\hat{r}_1$ is along the x-direction

$$\frac{\partial^2 P}{\partial \hat{r}_1^2} = \frac{\partial^2 P}{\partial x^2} \tag{C.4}$$

while the other two directional derivatives have to be calculated considering the particular directions as follows:

$$\frac{\partial^2 P}{\partial \hat{r}^2} = \frac{\partial}{\partial \hat{r}}\left[\frac{\partial P}{\partial \hat{r}}\right] = \frac{\partial}{\partial \hat{r}}\left[\vec{\nabla} P \cdot \hat{r}\right] = \vec{\nabla}\left[\vec{\nabla} P \cdot \hat{r}\right] \cdot \hat{r}. \tag{C.5}$$

Given that $\hat{r}_2 = (\alpha, \beta)$ and $\hat{r}_3 = (\alpha, -\beta)$,

$$\frac{\partial^2 P}{\partial \hat{r}_2^2} = \vec{\nabla}\left[\alpha\frac{\partial P}{\partial x} + \beta\frac{\partial P}{\partial y}\right] \cdot \hat{r}_2 \tag{C.6}$$

$$\frac{\partial^2 P}{\partial \hat{r}_2^2} = \alpha^2\frac{\partial^2 P}{\partial x^2} + 2\,\alpha\,\beta\,\frac{\partial^2 P}{\partial x \partial y} + \beta^2\frac{\partial^2 P}{\partial y^2} \tag{C.7}$$

$$\frac{\partial^2 P}{\partial \hat{r}_3^2} = \alpha^2\frac{\partial^2 P}{\partial x^2} - 2\,\alpha\,\beta\,\frac{\partial^2 P}{\partial x \partial y} + \beta^2\frac{\partial^2 P}{\partial y^2}. \tag{C.8}$$

Replacing equations (C.4), (C.7) and (C.8) in (C.3)

$$\frac{\partial P}{\partial t} = \frac{\delta r^2}{6\delta t}\left[(1 + 2\,\alpha^2)\frac{\partial^2 P}{\partial x^2} + 2\,\beta^2\,\frac{\partial^2 P}{\partial y^2}\right]. \tag{C.9}$$

Since $\hat{r}$ are unit vectors, $\alpha^2 + \beta^2 = 1 \Rightarrow 2\,\beta^2 = 2 - 2\,\alpha^2$, and thus,

$$\frac{\partial P}{\partial t} = \frac{\delta r^2}{6\delta t}\left[\frac{\partial^2 P}{\partial x^2} + 2\,\alpha^2\frac{\partial^2 P}{\partial x^2} + 2\frac{\partial^2 P}{\partial y^2} - 2\,\alpha^2\frac{\partial^2 P}{\partial y^2}\right]. \tag{C.10}$$

For a hexagonal lattice, $\alpha = 1/2$ and $\beta = \sqrt{3}/2$:

$$\frac{\partial P}{\partial t} = \frac{\delta r^2}{6\delta t}\left[\frac{\partial^2 P}{\partial x^2} + \frac{1}{2}\frac{\partial^2 P}{\partial x^2} + 2\frac{\partial^2 P}{\partial y^2} - \frac{1}{2}\frac{\partial^2 P}{\partial y^2}\right] \tag{C.11}$$

or, equivalently,

$$\frac{\partial P}{\partial t} = \frac{\delta r^2}{6\delta t}\,\frac{3}{2}\nabla^2 P. \tag{C.12}$$

Defining the diffusion coefficient to be

$$\mathcal{D} = \frac{\delta r^2}{4\delta t}, \tag{C.13}$$

we finally get the diffusion equation in 2 dimensions:

$$\frac{\partial P}{\partial t} = \mathcal{D}\,\nabla^2 P \tag{C.14}$$

C.2 Solution

To solve the diffusion equation

$$\mathcal{D}\,\nabla^2 P = \frac{\partial P}{\partial t}, \tag{C.15}$$

let us use separation of variables. Defining $P(\vec{\mathbf{r}}, t) = v(\vec{\mathbf{r}})\; u(t)$, and dividing eq (C.15) by P we obtain that

$$\mathcal{D}\,\frac{\nabla^2 P(\vec{\mathbf{r}}, t)}{P(\vec{\mathbf{r}}, t)} = \mathcal{D}\,\frac{\nabla^2 v(\vec{\mathbf{r}})}{v(\vec{\mathbf{r}})}, \tag{C.16}$$

$$\frac{1}{P}\,\frac{\partial P}{\partial t} = \frac{1}{u(t)}\,\frac{\partial u(t)}{\partial t}, \tag{C.17}$$

and, therefore,

$$\mathcal{D}\,\frac{\nabla^2 v(\vec{\mathbf{r}})}{v(\vec{\mathbf{r}})} = \frac{1}{u(t)}\,\frac{\partial u(t)}{\partial t}. \tag{C.18}$$

Since the right-hand-side has only spatial dependence, while the left hand side has only time dependence, they must be equal to a constant,

$$\mathcal{D}\,\frac{\nabla^2 v(\vec{\mathbf{r}})}{v(\vec{\mathbf{r}})} = \frac{1}{u(t)}\,\frac{\partial u(t)}{\partial t} = \lambda. \tag{C.19}$$

The differential equation for $u(t)$ can readily be integrated, yielding

$$u(t) = e^{\lambda t}, \tag{C.20}$$

and, for $u(t)$ not to diverge at large times, we require that $\lambda < 0$, or $\lambda = -\omega^2$

$$u(t) = e^{-\omega^2 t}. \tag{C.21}$$

Substituting (C.21) into (C.19), we obtain the equation for the spatial part, $v(\vec{r})$:

$$\mathcal{D}\,\frac{\nabla^2 v(\vec{r})}{v(\vec{r})} = -\omega^2 \tag{C.22}$$

$$\frac{\nabla^2 v(\vec{r})}{v(\vec{r})} = -k^2 \tag{C.23}$$

where $k^2 = \omega^2/\mathcal{D}$

We can solve this equation by separation of variables, $v(\vec{r}) = v_x(x)\, v_y(y)$:

$$\frac{\nabla^2 v(\vec{r})}{v(\vec{r})} = \frac{1}{v_x}\frac{\partial v_x(x)}{\partial x} + \frac{1}{v_y}\frac{\partial v_y(y)}{\partial y} = -k^2 = -(k_x^2 + k_y^2) \tag{C.24}$$

$$\frac{1}{v_x}\frac{\partial v_x(x)}{\partial x} = -k_x^2 \tag{C.25}$$

$$\frac{1}{v_y}\frac{\partial v_y(y)}{\partial y} = -k_y^2 \tag{C.26}$$

which yields

$$v(\vec{r}) = e^{ik_x x} e^{ik_y y} = e^{i(k_x x + k_y y)} = e^{i\vec{k}\cdot\vec{r}}. \tag{C.27}$$

The general solution will be a superposition of solutions of different k^2 values, each component with its own amplitude:

$$P(\vec{r}, t) = \int \frac{d^2k}{2\pi}\, f(\vec{k})\, e^{i\vec{k}\cdot\vec{r}}\, e^{-\mathcal{D}\, k^2\, t} \tag{C.28}$$

and $f(\vec{k})$ is given by the initial condition as

$$f(\vec{k}) = \int \frac{d^2r'}{2\pi} e^{-\imath\vec{k}\cdot\vec{r}'} \; P(\vec{r}', 0). \tag{C.29}$$

Substituting equation (C.29) into (C.28),

$$P(\vec{r}, t) = \int \frac{d^2k}{2\pi} \int \frac{d^2r'}{2\pi} e^{-\imath\vec{k}\cdot\vec{r}'} \; P(\vec{r}', 0) e^{\imath\vec{k}\cdot\vec{r}} \; e^{-\mathcal{D}\, k^2\, t} \tag{C.30}$$

Changing the order of integration and reordering the terms yields

$$P(\vec{r}, t) = \int \frac{d^2r'}{2\pi} \left[\int \frac{d^2k}{2\pi} \, e^{-\imath\vec{k}\cdot\vec{r}'} \; e^{\imath\vec{k}\cdot\vec{r}} \; e^{-\mathcal{D}\, k^2\, t} \right] P(\vec{r}', 0) \tag{C.31}$$

$$P(\vec{r}, t) = \int \frac{d^2r'}{2\pi} G(r, r', t) P(\vec{r}', 0) \tag{C.32}$$

where we have introduced the Green function $G(r, r', t)$

$$G(r, r', t) = \int \frac{d^2k}{2\pi} \, e^{\imath\vec{k}\cdot(\vec{r}-\vec{r}')} \; e^{-\mathcal{D}\, k^2\, t} \tag{C.33}$$

that can be evaluated as

$$G(r, r', t) = \frac{1}{2\mathcal{D}t} \, e^{-|\vec{r}-\vec{r}'|^2/(4\mathcal{D}t)}. \tag{C.34}$$

C.3 Example: Initial Gaussian Distribution

For an initial gaussian distribution

$$P(\vec{r}, 0) = \frac{1}{\pi\, \sigma_0^2} \, e^{-r^2/\sigma_0^2} \tag{C.35}$$

and, thus, the density in k-space is

$$f(\vec{k}) = \int \frac{d^2r}{2\pi} e^{-\imath\vec{k}\cdot\vec{r}} \, \frac{1}{\pi\, \sigma_0^2} \, e^{-r^2/(4\sigma_0^2)} \tag{C.36}$$

$$= \frac{1}{\pi\, \sigma_0^2} \int_{-\infty}^{\infty} \frac{dx}{\sqrt{2\pi}} e^{-\imath k_x\, x} \; e^{-x^2/(4\sigma_0^2)} \int_{-\infty}^{\infty} \frac{dy}{\sqrt{2\pi}} e^{-\imath k_y\, y} \; e^{-y^2/(4\sigma_0^2)}. \tag{C.37}$$

We can now evaluate each of these gaussian integrals

$$\int_{-\infty}^{\infty} \frac{dx}{\sqrt{2\pi}} e^{-ik_x x} e^{-x^2/(4\sigma_0^2)} = \frac{e^{-\sigma_0^2 k_x^2}}{\sqrt{2\pi}} \int_{-\infty}^{\infty} dx e^{-(x+i2\sigma_0^2 k_x)^2/(4\sigma_0^2)} \quad \text{(C.38)}$$

$$= \frac{e^{-\sigma_0^2 k_x^2}}{\sqrt{2\pi}} \sqrt{\pi 4\sigma_0^2} \quad \text{(C.39)}$$

$$= \sqrt{2}\sigma_0 e^{-\sigma_0^2 k_x^2} \quad \text{(C.40)}$$

leading us to the following distribution in k-space:

$$f(\vec{k}) = \frac{1}{\pi \sigma_0^2} 2\sigma_0^2 e^{-\sigma_0^2(k_x^2+k_y^2)} = \frac{2}{\pi} e^{-\sigma_0^2 k^2} \quad \text{(C.41)}$$

Substituting equation (C.41) into (C.28), we find the time evolution of the probability distribution:

$$P(\vec{r}, t) = \int \frac{d^2k}{2\pi} \frac{2}{\pi} e^{-\sigma_0^2 k^2} e^{i\vec{k}\cdot\vec{r}} e^{-\mathcal{D} k^2 t} \quad \text{(C.42)}$$

$$P(\vec{r}, t) = \frac{1}{\pi^2} \int d^2k e^{i\vec{k}\cdot\vec{r}} e^{-(\sigma_0^2+\mathcal{D}t) k^2}. \quad \text{(C.43)}$$

This integral can be evaluated through the same procedure as the previous one, yielding

$$P(\vec{r}, t) = \frac{1}{\pi (\mathcal{D} t + \sigma_0^2)} e^{-r^2/(\sigma_0^2+\mathcal{D} t)} \quad \text{(C.44)}$$

which shows that the spreading of the probability density increases linearly with time:

$$\langle r^2 \rangle(t) = \sigma^2(t) = \sigma_0^2 + \mathcal{D} t. \quad \text{(C.45)}$$

VITA

Enrique R. Batista received the following advanced degrees:

- Licenciado in Physics. University of Buenos Aires, Argentina. July 1992
- MS in Physics. University of Washington. December 1993
- PhD in Physics. University of Washington. June 1999

IMAGE EVALUATION TEST TARGET (QA-3)

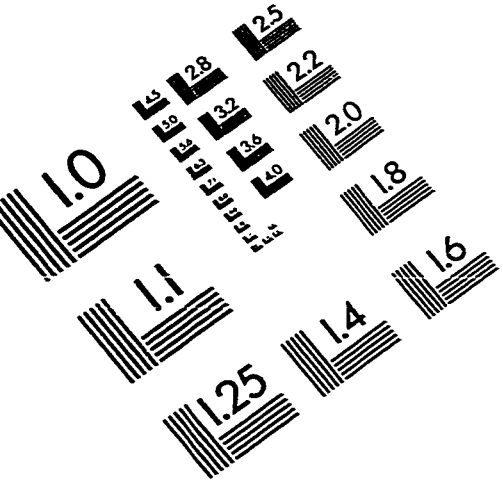

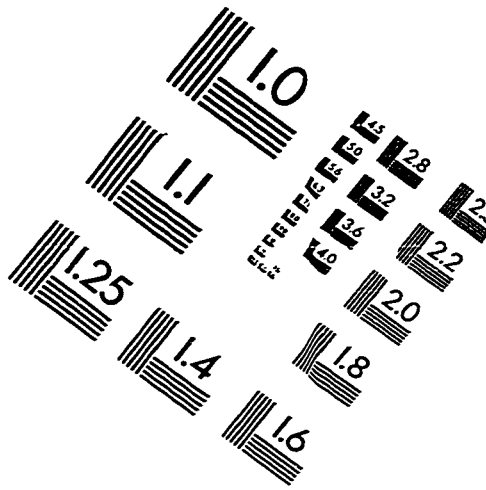

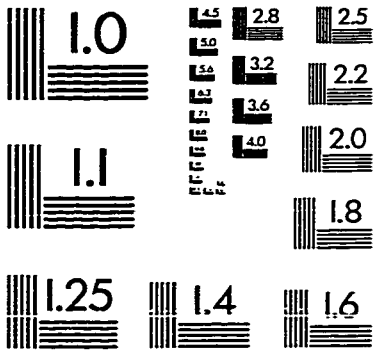

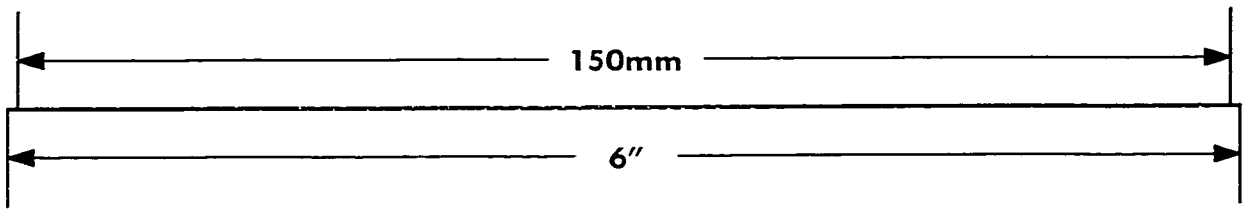

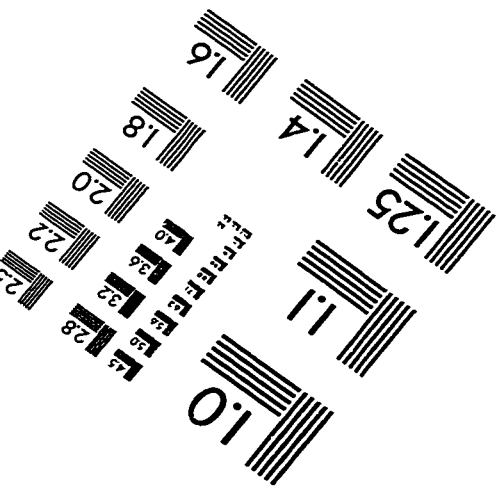

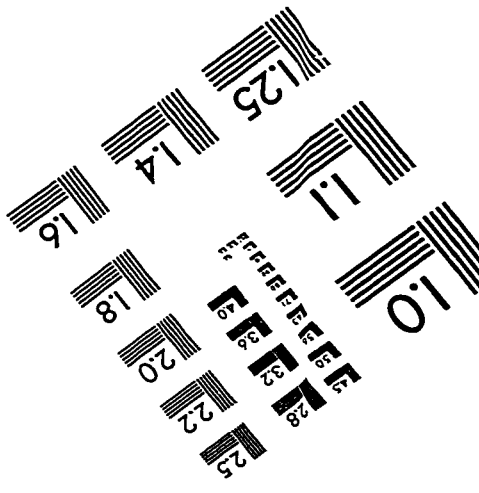

APPLIED IMAGE, Inc
1653 East Main Street
Rochester, NY 14609 USA
Phone: 716/482-0300
Fax: 716/288-5989